Characterization of neuronal network dynamics on microelectrode arrays: assessing the effect of temperature and the activity profile of long-term recordings

João Tiago dos Santos Palma

Masters Dissertation
Integrated Master in Bioengineering
Branch of Molecular Biotechnology

Supervisor:
Miguel Aroso (PhD)

Co-supervisor:
Paulo Aguiar (PhD)

Porto, September 2021

Agradecimentos

Quero especialmente agradecer ao Miguel Aroso pelo apoio fundamental que me deu durante este projeto, como orientador e como amigo. Só consigo imaginar a paciência que foi necessária e as dores de cabeça que provoquei e, por isso, estou eternamente grato! Pelo enorme sentido critico e rigor científico que servirá sempre como modelo no meu futuro. Que continues a encontrar os locais mais recônditos para almoçar e que um dia consigas exterminar a população de vespas do i3S.

Não posso deixar de agradecer ao Paulo Aguiar pela incrível oportunidade de fazer parte do NCN, uma nova família. Um grupo extraordinariamente inclusivo, jovem e estimulante que só podia ter sido reunido sobre as condições de um grande líder. Porque sei que nunca vou encontrar outro chefe que organize os encontros mais radicais de Ultimate Frisbee! Muito Obrigado! Por tudo o que aprendi e pela experiência que levo para a vida, já com muitas saudades.

Ao grande Domingos e a esta grande amizade! Gostava de ter tido mais tempo para te ensinar a programar. E a tocar guitarra. E para fazer a tua tese por ti. À Andreia, por todo o apoio, sensibilidade e alegria. E à Catarina, a minha parceira de tese. Por toda a ajuda e empatia no sofrimento! Ao resto da malta do NCN, os que ficam e os que passaram. Obrigado pela disposição e por tornarem tudo mais fácil!

À Márcia, sua incrível criatura, por me estares a formatar a tese neste momento. Grande companhia de trabalho e das distrações. És a maior!

A todos os meus amigos, companheiros da vida, pelo apoio incondicional. Sem vocês, isto seria impossível. Obrigado aos meus pais, ao Duarte e a toda a minha família. Por nunca deixarem de acreditar em mim!

Resumo

O Sistema nervoso é, indiscutivelmente, o mais complexo na fisiologia mamífera, apelando muitos a aventurarem-se na sua compreensão. Uma das suas características fundamentais consiste na sinalização rápida e eficiente com a qual os diferentes neurónios comunicam entre si. Como tal, a análise eletrofisiológica da atividade neuronal possui um papel fundamental na área das neurociências. De entre as técnicas usadas para o seu estudo, a aplicação de MicroElectrode Arrays (MEAs) oferece um método robusto para monitorizar, não invasivamente, a atividade eletrofisiológica de populações neuronais *in vitro* com alta resolução espaciotemporal. Consequentemente, é considerada uma técnica excelente para analisar as dinâmicas de atividade neuronal ao longo de extensos períodos de tempo, e estudar o efeito na atividade neuronal de perturbações às condições fisiológicas, sejam estas causadas por alterações no ambiente ou pela adição de agentes exógenos. É amplamente reconhecido que a atividade neuronal *in vitro* é afetada por perturbações na temperatura durante a gravação, e que, as populações neuronais apresentam ciclos de atividade com períodos que duram de entre segundos a horas. No entanto, estas particularidades estão ainda vagamente caracterizadas. Com isto em mente, desenvolvemos duas abordagens complementares para caracterizar melhor a atividade eletrofisiológica de populações neuronais *in vitro*. Por um lado, avaliamos o efeito da temperatura na atividade neuronal com foco em: a) caracterizar e otimizar o controlo de temperatura no sistema MEA, e b) gravar e analisar a atividade elétrica de culturas neuronais primárias do hipocampo a condições fisiológicas (37°C) e de hipertermia (39°C). Por outro lado, exploramos a presença de padrões temporais de atividade elétrica em culturas neuronais pela execução de gravações de longa duração (24 horas) a diferentes fases de maturação da rede neuronal (Dias em vitro (DIV) 7 e 14).

Durante este trabalho demonstramos que a temperatura medida no meio celular dentro de um MEA é inferior à temperatura imposta ao sistema de gravação MEA2100. Posteriormente, demonstramos de forma clara que um aumento de 2°C acima da temperatura fisiológica leva a uma diminuição significativa da atividade neuronal, no entanto, os mecanismos responsáveis por esta diminuição necessitam de ser melhor investigados. Além disso, observamos que a atividade neuronal gravada ao longo de 24 horas

a DIV 7 e 14 varia imensamente ao longo do tempo, revelando a ausência de padrões de atividade neuronal nesses DIVs. Estas observações dificultam a caracterização de um tempo de gravação ótimo para descrever a atividade neuronal ao longo do tempo, realçando a necessidade de um cuidado rigoroso na delineação de experiências de eletrofisiologia. Como tal, especial atenção deve ser prestada à duração de gravação e ao intervalo entre gravações consecutivas, de acordo com o objetivo da experiência e do DIV da cultura.

Abstract

The nervous system is, undoubtedly, the most complex in mammalian physiology, appealing many to endeavour in its understanding. One of its fundamental characteristics relies on the fast and efficient electrical signalling through which neurons communicate. Thus, the electrophysiological analysis of neuronal activity has a fundamental role in the field of neurosciences. Among the techniques developed for its study, the application of MicroElectrode Arrays (MEAs) offers a robust method to monitor, non-invasively, the electrophysiological activity of *in vitro* neuronal populations with a high spatiotemporal resolution. Therefore, it is an excellent technique to analyse the dynamics of neuronal activity over long periods of time and study the effect on neuronal activity of perturbations to the physiological conditions, either due to alterations in the environment or by addition of exogenous agents. It is generally acknowledged that neuronal activity *in vitro* is affected by perturbations on the recording temperature and that neuronal populations present cycles of activity with periods that span from seconds to hours. However, these features are not yet well characterized. With this in mind, we developed two complementary approaches to further characterize the electrophysiological activity of *in vitro* neuronal populations. On one hand we evaluated the effect of temperature on the neuronal cultures, with focus on: a) the characterization and optimization of the temperature control of the MEA system, and b) recording and analysis of the electrical activity of primary hippocampal neuronal cultures at physiological conditions (37°C) and hyperthermic conditions (39°C). On the other hand, we explored the presence of temporal patterns of electrical activity in neuronal cultures by conducting long-term recordings (24 hours) at different network maturation stages (Day in vitro (DIV) 7 and 14).

During the course of this work, we revealed that the temperature measured in the medium of the MEA chip is lower than the temperature set in the MEA2100 recording System. Then, we have clearly shown that an increase of 2°C above the physiological temperature leads to a significant decrease of neuronal activity, however, the mechanisms behind this reduction need to be further investigated. Besides, we observed that the neuronal activity recorded over 24h at DIV 7 and DIV 14 changes vastly over time, unveiling the absence of patterns of neuronal activity at such DIVs. This hinders the characterization

of an optimum recording time to describe neuronal activity across time, stressing the need to carefully design electrophysiological experiments. In such way, particular attention should be given to the recording duration and the interval between recordings, while bearing in mind the objective of the experiment and the DIV of the cultures.

Contents

List of Figures

Abbreviations, Acronyms e Symbols

$[X]_{in}$ - Concentrations in the intracellular fluid

$[X]_{out}$ - Concentrations in the extracellular fluid

4α-PDD – 4α-Phorbol 12-13-didecanoate

ADC – Analog-to-digital conversion

AP – Action Potential

ARD - Ankyrin repeat domain

Au – Gold

Ca^{2+} – Calcium ion

Cl^- - Chloride ion

C_m – Capacitor

CNS - Central Nervous System

CO_2 – Carbon dioxide

d – Diameter of axon

D - Distance from the source to the recording point

DIV – Days in vitro

DMSO - Dimethyl sulfoxide

DSP – Digital signal processor

EAP – Extracellular action potential

EEG – Electroencephalography

E_m - Resting potential

E_x – Equilibrium potential

F – Faraday´s constant

$\bar{g}$ - Membrane maximum conductance

GHK - Goldman-Hodgkin-Katz

g_x - Conductance per unit area

h – Inactivation state variable

h – Longitudinal distance from the end of the axon

HBSS - Hank's Balanced Salt Solution

HEK293 - Human embryonic kidney 293 cells

HH – Hodgkin and Huxley

hiFBS - Heat-inactivated fetal bovine serum

Hz – Hertz

I - Membrane current

IBI – Interburst Interval

I_c – Capacitive current

IC_{50} - Half maximal inhibitory concentration

I_{GABA} - GABA-activated current

I_i – Ionic current

I_K – Potassium current

I_L – Leak current

I_{LC} – Axial current

I_{Na} – Sodium current

ISI – Interspike interval

ITO – Indium tin oxide

K^+ - Potassium ion

KO – Knockout

LFP – Local field potential

LSA – Line source approximation

m – Gating variable

MCS – Multi Channel Systems

MEA - MicroElectrodes Array

MFR – MFR

Mg^{2+} – Magnesium ion

min – Minutes

mV - Milivolts

n – Gating variable

Na^+ - Sodium ion

n^x – Probability of gate to be in open state

PDL - Poly-D-Lysine

PIP_2 - Phosphatidylinositol-4,5-biphosphate

PKA - Cyclic-AMP dependent protein kinase A

PKC – Protein kinase C

PNS - Peripheral Nervous System

Pt – Platinum

P_x - Permeability of the membrane

Q_{10} - Temperature coefficient

R – Axial resistivity

r – Radial distance from the axon

R – Universal gas constant

RMS – Root mean square

s - Seconds

SD – Standard Deviation

SGK-1 - Serum glucocorticoid protein kinase-1

SiN – Silicon nitride

SNR – Signal-to-noise ratio

SRC - SRC family kinases

SX – Transmembrane domain X

T – Temperature in Celsius

t – Temperature in Kelvins

TC02 – External temperature controller from Multi Channel Systems

TC-K – Type K thermocouple sensor

TiN – Titanium nitride

TRP – Transient Receptor Potential

TRPA - Transient Receptor Potential Ankyrin

TRPC - Transient Receptor Potential Canonical

TRPM - Transient Receptor Potential Melastatin

TRPML - Transient Receptor Potential Mucolipin

TRPP - Transient Receptor Potential Poly-cystin

TRPV - Transient Receptor Potential Vanilloid

TRPV4 - Transient Receptor Potential Vanilloid 4

V - Membrane potential

V_{out} - Extracellular potential

wMBR – Weighted mean burst rate

wMNBR – Weighted mean network burst rate

X – Synchrony quantification

z_x – Valence of the ion

α_X – Rate coefficient

β_X - Rate coefficient

Δs – length of the axon

σ^2 – Variance

Chapter 1

Introduction

The human nervous system is a highly complex structure responsible for countless body functions. It consists of organized signaling pathways that are responsible for the rapid exchange of information inside the Central Nervous System (CNS), which comprises the brain and spinal cord, but also for its communication with the Peripheral Nervous System (PNS).

The PNS essentially works as an interface for the CNS with the rest of body, allowing for the sensorial acquisition of environmental information, either internal or external, and the motorial execution of voluntary and autonomic tasks. Such mechanisms allow homeostatic and endocrine maintenance, as well as reflex movements and deliberate physical actions. Accordingly, the remarkable range of human behavior depends on the sophisticated brain that constructs our perception of reality, selecting and memorizing cues from the environment, constantly learning, and both consciously and unconsciously molding our behavior. The human brain is a network of approximately 86 billion of interconnected neurons, the basic unit of the brain, and roughly the same number of glial cells, which offer metabolic and structural support, as well as a regulatory role in neuronal activity. Therefore, trying to comprehend how the combined activity of all different cell types results in such a wide range of functions is an endearing, yet extremely challenging, endeavor that continuously captivates scientists[1–3].

The fundamental activity of neurons relies on the generation and propagation of electrical signals through which these encode information and communicate with each other and different organs in the body. These electrical signals, or action potentials (APs), are the result of a choreographed activity of ion channels, a class of integral membrane proteins. It is remarkable how the different patterns of ion channels expression mediate membrane excitability and response to stimuli, as distinct combinations in morphologically similar cells may lead to single APs or sequences of APs with both constant or varying firing

rates, and thus conveying distinct information. Additionally, channels vary in the factors that control their gating, granting another degree of complexity to the system. Some will react to the binding of chemical ligands, while others are voltage or mechanosensitive. For example, some ion channels, such as Transient Receptor Potential Vanilloid 4 (TRPV4), are temperature sensitive, changing their voltage gating membrane potentials according to temperature shifts[1,2].

Electrophysiology allows for the application and development of functional analysis methodologies that enable the study of a wide range of neuronal activity. However, practical and ethical limitations in the analysis of the *in vivo* brain often hamper informative manipulations. Therefore, the use of *in vitro* cultures, although presenting the typical translational limitations, offers less complex and more accessible models that have granted valuable insights into the understanding of neuronal activity[4,5]. Thus, such models can be coupled to electrically sensitive devices such as microelectrode arrays for the investigation of the mechanisms underlying neuronal communication, pathophysiological conditions, and the neurotoxicity of drugs. Indeed, MEA technology allows for the non-invasive acquisition of spatiotemporal information of the neuronal networks, granting researchers with the tools for the development of new methodologies and experiments for further comprehension of the nervous system in normal and pathophysiological states[6,7].

1.1 - Motivation

Even though the cellular environment and stimuli are significantly different from the brain physiology, *in vitro* cultures of neurons retain the fundamental electrophysiological properties of the tissue of origin, representing a reductionist model for the study of neuronal networks when coupled with MEAs[8]. These are well established for the study of pathologies with underlying network disorders, such as epilepsy, a condition characterized by seizures that result from an increased synchronization of excitatory neurons[5]. Moreover, the evaluation of the neurotoxic effect of different chemicals is also a recurrent application and there are reports of interlaboratory reproducibility supporting this methodology[9,10].

Temperature is a variable known to interfere with the dynamics of neuronal activity. Impairments in memory, attention and information processing have been associated with acute episodes of hyperthermia, and worse outcomes correlate with prolonged exposures and extreme temperature increases[11]. *In vitro*, both hypothermic and hyperthermic conditions have shown to result in neuronal activity depression[12,13]. However, there is limited information defining such alterations and temperature control during experimental designs is often unspecified. Therefore, an exploration of the effect of a pathophysiological temperature on neuronal activity would be a valuable reference for a proper experimental analysis.

Concerning the analysis of neuronal activity, it usually relies on the quantification of the frequency of action potentials, or spikes, and the occurrence of synchronized spiking events, or bursts. Additionally, there is a wide range of metrics based on these events which allow for a detailed assessment and comparison of activity dynamics within neuronal cultures. However, the activity patterns of the neuronal network change substantially with time during *in vitro* maturation. The initial period, until around 7 days *in vitro*, is characterized by the modulation and shaping of synaptic connectivity and therefore presents less overall activity. After a period of maturation, at between 2 and 3 weeks the cultures typically display more stable firing patterns[14–16]. On top of that, there is evidence that neuronal populations display cycles and fluctuations of activity levels with periods that span from seconds to hours. The description of these putative patterns of activity will be very relevant to better understand neuronal network dynamics, with additional implications in the design and analysis of MEA-based experiments.

1.2 - Objectives

Although in the last couple of decades the use of MEAs chips in the study of neuronal activity *in vitro* has grown substantially, there are still important aspects of culture dynamics that were not properly addressed. Having this in mind, the main goal of this dissertation is to better characterize the activity of *in vitro* neuronal cultures by assessing the effect of temperature on such activity and exploring the activity dynamics over 24h periods.

For this purpose, the first part of the work will be focused on the optimization of the temperature control of the experimental setting and the characterization of the impact that pathological temperatures, such as observed in hyperthermia, have on the neuronal activity. The second part of the work will explore the intrinsic dynamics of neuronal activity in neuronal cultures during the course of 24h at DIV7 and DIV14, aiming at detecting potential patterns of activity and identify the minimal recording time that better represents such dynamics.

In order to achieve this, we will record the activity of primary embryonic hippocampal neuronal networks on 6-well MEAs via the *in vitro* recording system MEA2100 (Multi channel Systems).

Chapter 2

"Electrophysiology"

2.1 The basis of neuronal electrical activity

The neuron is the fundamental building block of the nervous system. It provides the organism with complex, fast signaling networks capable of conducting electric signals, that can travel at rates of 100 m/s, over long distances. Although there are about 100 different types of neurons, most follow the same morphological display: a cell body, or soma, that processes and integrates information and gives rise to two distinct types of processes, or neurites: dendrites and axons. Dendrites span out in a tree-like manner and are typically the site of stimulation incoming from other neurons. The axon is a tubular structure that can extend over 2 meters and functions as the transmitting element of the neuron. Branches of the axon may connect with up to 1000 neurons through cell-cell junctions, called synapses. An electrical signal is typically integrated in the dendrites and propagated along the axon, without attenuation, until it is transmitted to another neuron, or other type of cell.[1,2]

The ability of the neuron to conduct electric signals stems from the flow of ions across the cell membrane. The separation of extracellular and intracellular space creates a membrane potential due to the different ion concentrations and their charge. This unequal distribution of ions such as Sodium (Na^+) and potassium (K^+), under normal circumstances, creates a membrane resting potential of about -65 mV, indicating that the intracellular medium is more negative than the extracellular. Therefore, when stimuli destabilize this equilibrium above a certain threshold, the cell generates an AP, an all-or-none impulse.[1,2,17] Despite the broad range of sensorial inputs and functions of the nervous system, the AP is a highly stereotyped event, meaning that the signals generated from different stimuli are identical. This highlights a key feature of brain function, that the

information transmitted is not determined by the shape of the signal but from the signaling pathway it assumes.[1]

This section seeks to provide sufficient knowledge about how neurons generate and propagate APs, the fundamental unit of communication of the nervous system, and how the molecular composition of neurons impacts their functioning. Hopefully, this will help in the posterior understanding of how electrophysiological recordings present a relevant tool for a better comprehension of the dynamics of neuronal networks.

2.1.1 Neuronal Membrane

To understand the function of neurons, it is necessary to understand the structure and function of the membrane and its associated proteins. The neuronal membrane consists of an impermeable 5 nm thick lipid bilayer with transmembrane proteins embedded in it. These proteins can be either ionic channels or ionic pumps and allow for the ion flow across the membrane and maintenance of the resting membrane potential. Ion channels are pores that confer semi-permeability to the membrane by allowing the passage of specific ions at rates of up to 100 million ions per second, in just a single channel. These can be passive channels, which means that the permeability does not change, or active channels. Active channels dwell both in open and closed states, and this change may represent the effect of the membrane potential, ionic concentrations, or the presence of ligands. Ionic pumps form channels that transport certain ions across the membrane by consuming ATP. This process, contrarily to ion channels where ions flow unimpeded through a continuous gap, involves conformational changes that result in considerably slower rates of passage.[1]

Regarding the concept of resting membrane potential, it is necessary to comprehend the forces that play upon the ions. The intracellular and extracellular space are filled with several ions, both negative anions, such as chloride (Cl^-), and positive cations including K^+, Na^+, calcium (Ca^{2+}) and magnesium (Mg^{2+}), at different concentrations. Since there are both non-uniform concentrations and electric charges, that produce an electrical field, the flow of ions is governed by a combination of diffusion and electrical drift. Diffusion consists of the flow of particles according to the concentration gradient and, therefore, an ion would flow down from the higher concentration to the lower concentration. However, considering the electrical charge of the different ions gives rise to another phenomenon, the electrical drift, that consists in the movement of charged particles in an electric field, according to the potential gradient.[2,17]

To a better gasp of this situation, it is better to imagine a hypothetical cell separated from the outside with an impermeable membrane. Inside the cell, there is a concentrated potassium solution that consist of equal numbers of K^+ and anions A^-, while in the outside the same solution is present but diluted. Despite the existence of a concentration gradient across the membrane, there is no movement due to its

impermeability. However, there is no potential difference across the membrane as both solutions are electrically neutral due to the ratio of K^+ to A^- being 1. Now, one should consider that at one point the membrane is inserted with protein channels only permeable to K^+, meaning this cation is free to move through the membrane but not A^-. Initially, diffusion plays a role and K^+ ions pass through the channels down the concentration gradient. Since A^- does not move, the inside of the cell starts to acquire a net negative charge and, as the opposite occurs in the outside, a potential difference is established across the membrane. As this potential grows, the electric force starts to pull K^+ back into the cell with more strength. Thus, at one point, the electrical force pulling K^+ inside exactly counteracts the force of diffusion, meaning that an equilibrium potential is established.[17] To calculate the equilibrium potential for any sole ion, one can use the Nernst equation:

$$E_X = \frac{Rt}{z_X F} \ln \frac{[X]_{out}}{[X]_{in}} \tag{1}$$

where, E_x is the equilibrium potential, or Nernst potential, for the membrane-permeable ion X. R stands for the universal gas constant, t is the temperature in Kelvins, z_x is the charge of the ion, F is the Faraday's constant and $[X]_{in}$ and $[X]_{out}$ reflect the ion concentration inside and outside of the cell, respectively.

However, in the complex physiology of the neuron, there is a need to understand the interactions in a membrane that is permeable to more than one ion. Therefore, we can resort to the scheme in Figure 1 for an easier understanding of this scenario.
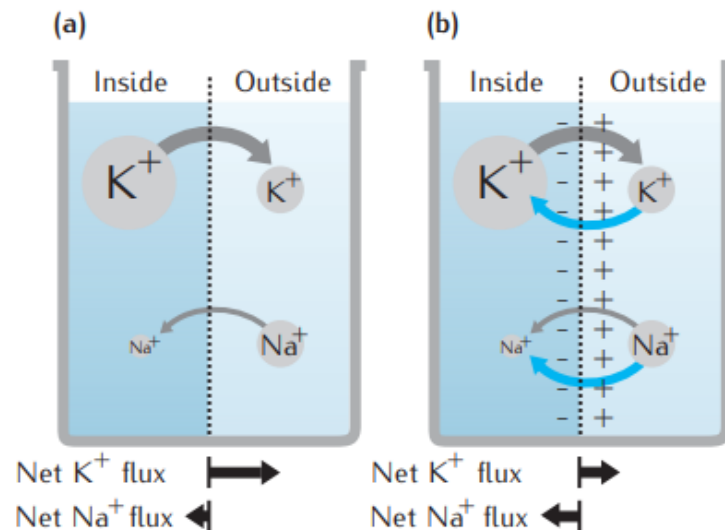
Figure 1 – Representation of diffusion and electrical drift in two membrane-permeable cations (the anions are ommited for symplification).
The grey arrow represents the net flow due to diffusion and the blue arrow the flow due to the electric field. (a) Ion flow according to concentration gradient. (b) The generation of an electrical potential across the membrane. The net flux of one ion is oppositely equal to the net flux of the other. Adapted from Sterrat et al., 2011[17].

Considering that both sides of the membrane contain a solution of two different membrane-permeable cations, K+ and Na+, with the depicted ratios (as in a typical neuron), but also membrane-impermeable anions, that although omitted in order to simplify, confer an initial electrically neutral state to each of the sides of the membrane. Since the concentration difference is bigger for K+ than Na+, according to Fick's law, which states that larger concentration gradients lead to larger fluxes, the flux of K+ down its gradient potential is bigger than the flux of Na+ (Figure 1a). Accordingly, there is an increase in positive charge in the right side of the membrane, creating an electric field that causes electrical drift of both cations to the left. Thus, resulting in a decrease of the net flux of K+ and an increase of the net flux of Na+, eventually attaining equal, but opposite magnitudes (Figure 1b). In this state there is no net flux of charge, the charge on each side of the membrane is constant and so is the membrane potential. However, there is still a diminishing flow of the ions across the concentration gradient until both sides are equal and the membrane potential eventually reaches zero. In a neuron, the presence of ionic pumps prevents this effect.[17] Finally, it can be deduced that, in this case, the resting membrane potential lies somewhere between the potassium and sodium equilibrium potentials.

To quantitatively predict the resting potential of the membrane, we can first use the Goldman-Hodgkin-Katz (GHK) current equation to predict the current (I) of a specific ion (X) across the cell membrane for a specific value of membrane potential (V), per unit area of membrane (in cm^{-2}):

$$I_X = P_X z_X F \frac{z_X F V}{RT} \left(\frac{[X]_{in} - [X]_{out} e^{-z_X FV/RT}}{1 - e^{-z_X FV/RT}} \right) \tag{2}$$

where P_x stands for the permeability of the membrane to the chosen ion.[17] Also, it should be noted that this equation was developed considering that the ions cross the membrane independently and that the electric field within the membrane is constant. By defining I, the membrane current, as 0 and solving (2) for voltage, the GHK voltage equation for the reversal potential, the membrane potential at which the current reverses direction, is obtained (in this case, for a membrane permeable to K+, Na+ and Cl-):

$$E_m = \frac{RT}{F} \ln \frac{P_{Na}[Na^+]_{out} + P_K[K^+]_{out} + P_{Cl}[Cl^-]_{in}}{P_{Na}[Na^+]_{in} + P_K[K^+]_{in} + P_{Cl}[Cl^-]_{out}}. \tag{3}$$

2.1.2 Hodgkin-Huxley model

The first quantitative description of the active mechanisms governing an AP originates from a series of five papers lead by Hodgkin and Huxley (HH), published in 1952 [18–22]. At the time, the concept of ion channels was yet to be established. Little was known about the properties of the membrane, and the varying concentration of ions on both sides

had only been recently associated with nervous impulses. Thus, the authors aim was to uncover the laws governing the movement of ions across the membrane during electrical activity. For such purpose, the newly developed voltage clamp method was employed in the giant axon of a squid, as it is large enough (up to 1 mm in diameter) to be inserted with the two necessary electrodes. One was used to record the membrane potential and the other to electronically compare this value with a desired "control voltage" and, subsequently, inject the necessary current to reach this control voltage. In this way, they were able to access the dynamics of membrane current at different values of membrane potential.

To facilitate the interpretation of the Hodgkin-Huxley model, the equivalent electrical circuit for a compartment of the cell membrane proposed by the authors is shown in Figure 2[17].
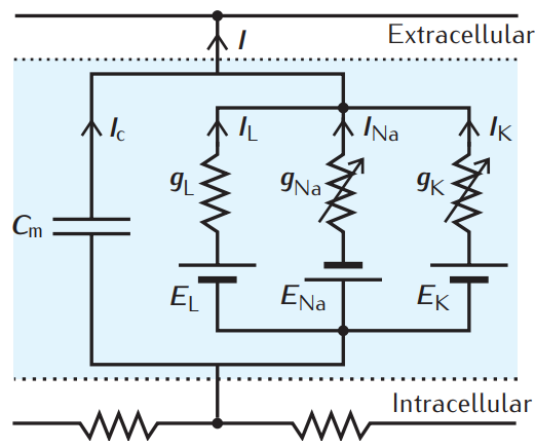
Figure 2 – The Hodgkin-Huxley equivalent circuit model for a compartment of cell membrane.
Adapted from Sterratt et al., 2011[17].

In this model, the cell membrane is represented by a capacitor (C_m) since it accumulates charge. The membrane current, I, can be carried either by charging the membrane capacity, as capacitive current (I_c), or by the flow of ions, which is presented as a resistance and battery in series. The latter comprises three different ionic currents, the sodium current, I_{Na}, the potassium current, I_K, and the leak current, I_L, resulting from the flow of chloride and other ions. These ionic currents for a certain ion X can be calculated in a simplified equation of (2):

$$I_X = g_X(V - E_X) \tag{4}$$

where g_x is the conductance per area unit (mS.cm^{-2}) for a certain ion, and the difference between membrane potential and equilibrium potential of the respective ion, (V-E_X), corresponds to the electrochemical driving force acting on the ion. It is relevant to note the arrow above the sodium and potassium resistors, meaning that these are altered with

voltage, which we now know to translate as voltage-gated ion channels. The elementary equation that corresponds to the equivalent electric circuit is:

$$I = I_c + I_i \tag{5}$$

where I_i corresponds to the sum of ionic currents and I_c is given by the product between the membrane capacitance and the rate of change of voltage, as shown in the following equation:

$$I_c = C_m \frac{dV}{dt}. \tag{6}$$

Once the authors discovered the voltage-induced variability in conductance for sodium and potassium, it was necessary to establish adequate equations to fit this behavior over time [17,22,23]. Thus, they conducted experiments with different values of clamp voltage. To isolate the current corresponding to each ion, the ion substitution method was used [17,18]. Initially, the extracellular concentration of sodium is lowered by partial replacement with impermeant choline ions. Then, the current is recorded under clamp voltage conditions in choline water and in sea water. Assuming that ions cross the membrane independently, the current carried by Na$^+$ differs, but stays the same for the other ions. Thus, the current measured in both media can be used to determine the sodium current and, consequently, the potassium current by subtracting the sodium current and the leak current, obtained with (4).

For potassium, the conductance behavior best suited an exponential to the fourth power as depicted below:

$$g_K = \bar{g}_K n^4 \tag{7}$$

where $\bar{g}$ is the maximal conductance and n is a dimensionless variable which can vary between 0 and 1. The authors suggest a physical basis for the model that gives n a palpable definition[22]. They introduce the idea of the existence of gates in the membrane, which can be in an open or closed state, and that this change is controlled by a number of gating particles, that also vary between an open or closed state, depending on the membrane potential. For a potassium ion to flow, all the gating particles in the gate need to be in their open state. Thus, the gating variable n can be defined as the probability of a sole gating particle to be in its open state and n^x as the probability of the gate to be open, where x is the needed number of gating particles for each gate, which in the case of potassium is 4.

Regarding sodium conductance, the fit was somewhat different since, at a fixed voltage, the conductance initially rose but then suffered an exponential decay, an inactivation, as named by the authors[22]. To represent this change in the model, an inactivation state variable, h, was introduced. Thus, the equation that more adequately shows the sodium membrane conductance is:

$$g_{Na} = \bar{g}_{Na}m^3h \tag{8}$$

where, m is the homologous for n in (7) and both m and h are voltage dependent.

Finally, and considering all the equations mentioned in this subsection, the Hodgkin-Huxley equation for the variation in time of membrane potential in a small part of the squid giant axon is:

$$C_m\frac{dV}{dt} = -\bar{g}_L(V - E_L) - \bar{g}_{Na}m^3h(V - E_{Na}) - \bar{g}_Kn^4(V - E_K) + I_{LC}. \tag{9}$$

Since this equation represents only a portion of the axon, I_{LC} states the contribution of the axial current from regions bordering this part of the axon. If a continuous model of the axon is to be considered, this current can be replaced by the second derivative of the membrane potential with respect to space, $\frac{d}{4R_a}\frac{\partial^2 V}{\partial x^2}$, where d is the diameter of the axon, R is the axial resistivity and x the position along the axon [17,22].

In summary, the observed pattern for the AP corresponds to Figure 3 and can be described over several phases [1,24].
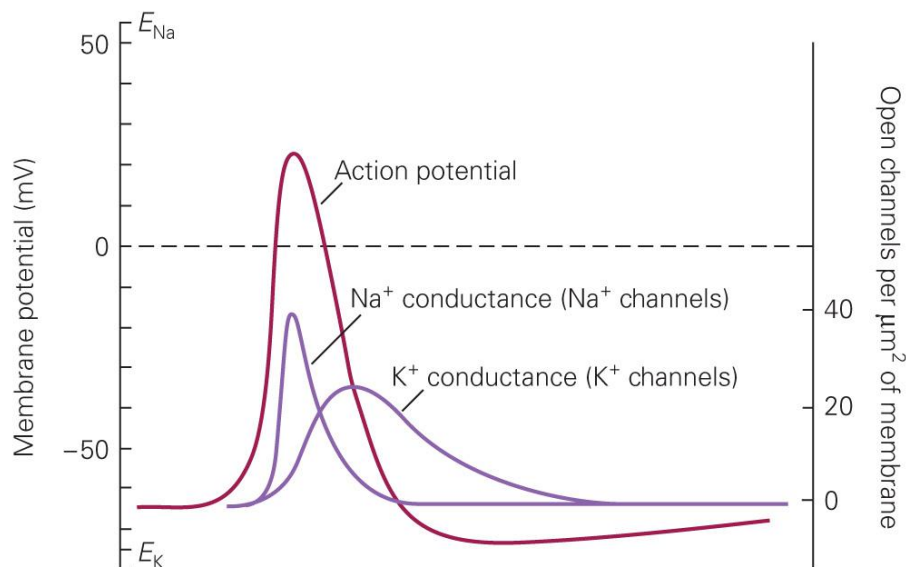
Figure 3 – The action potential and separate behavior of Na+ and K+ channels.
Adapted from Kandel et al, 2013[1].

The initial point recalls for the concept of resting membrane potential which, as explained before, is about -70mV in a typical neuron. The presence of a stimulus can result in hyperpolarization (increased intracellular negativity) or depolarization (decreased

intracellular negativity). The general response to these inputs is graded, however, when a depolarizing stimuli reaches a certain threshold (tipically around -50mV), an AP is triggered. This corresponds to a rapid further depolarization to a positive value peak and is entirely driven by the activation of voltage-gated sodium channels and a subsequent influx of Na^+, caused by the strong driving force. The next phase represents a repolarization to the resting potential and is governed by two factors. The inactivation of all sodium channels at the peak of the AP and the opening of voltage-gated potassium channels. The opening of these also happens when the threshold is surpassed, but is considerably slower than that of sodium channels. The outflux driving force for K^+ is initially driven by the concentration gradient and then, as the cell becomes more positive, also by an electrical gradient. Finally, a small phase of hyperpolarizing afterpotential, right before returning to baseline, happens due to the delay in closing of potassium channels and is counterbalanced by the work of sodium-potassium pumps (Figure 3). Another important concept is the refractory period, which is characterized by the amount of time necessary for the membrane to be ready to fully respond to a second stimulus. It comprises an absolute refractory period, corresponding to depolarization and repolarization, where it is impossible to generate a new AP. And a relative refractory period, occuring during the hyperpolarizing afterpotential, where the threshold is higher and the peak of the AP reaches a lower value.

Since these papers were published, several more ion channels, with different controlling properties, have been discovered and studied in a variety of neurons. However limited, the Hodgkin-Huxley equations still provides a foundation for the development of computational neuroscience models and the understanding of the function of the nervous system [24].

2.1.3 Temperature effect on neuronal activity

In their experiments, Hodgkin et al. reported on how temperature affects neuronal activity during voltage clamp recordings[18]. In sum, variations in temperature affect the ion channel gating kinetics, as well as the maximum ion channel conductance, hence resulting in alterations in the generation, propagation, and shape of action potentials[25].

Such temperature dependence can be quantified by making use of the Q_{10} temperature coefficient:

$$Q_{10} = \frac{\text{rate at } T + 10°C}{\text{rate at } T}, \tag{10}$$

providing the change in rate, of a specific property, for a 10˚C increase in temperature, T[17,26].

In equations (7) and (8), three state variables were introduced that describe the behavior of sodium and potassium conductances and represent the state of the ion channel – n is the gating variable that corresponds to the level of activation for the potassium channel, and m and h for the activation and inactivation, respectively, of the sodium channel. The rate at which these variables change over time is governed by the following equations[17]:

$$\frac{dn}{dt} = \alpha_n(1-n) - \beta_n n; \quad \alpha_n = 0.01\frac{(v+55)}{1 - e^{(-(v+55)/10)}}; \quad \beta_n = 0.125e^{(-(v+65)/80)};$$

$$\frac{dm}{dt} = \alpha_m(1-m) - \beta_m m; \quad \alpha_m = 0.1\frac{(v+40)}{1 - e^{(-(v+40)/10)}}; \quad \beta_m = 4e^{(-(v+65)/18)}; \tag{11}$$

$$\frac{dh}{dt} = \alpha_h(1-h) - \beta_h h; \quad \alpha_h = 0.07e^{(-(v+65)/20)}; \quad \beta_h = \frac{1}{e^{(-(v+35)/10)} + 1};$$

where the variables α_X and β_X are rate coefficients that depend on the membrane potential, v, at the given time, and X corresponds to the fraction of gating particles X in the open state while (1-X) represents the fraction in the closed state. The rate of transition from a closed state to an open state is governed by α while β reflects the opposite change. For the temperature variation, if we consider that for a temperature T_1, the voltage-dependent rate coefficients are $a(V,T_1)$ and $B(V,T_1)$, their values at another temperature, T_2 can be obtained in[17]:

$$\alpha(V,T_2) = \alpha(V,T_1)Q_{10}^{\frac{T_2-T_1}{10}} \text{ and } \beta(V,T_2) = \beta(V,T_1)Q_{10}^{\frac{T_2-T_1}{10}} \tag{12}$$

In their studies, Hodgkin et al. estimated the Q_{10} for the gating rates to be around 3, a value that is now known to be normal for ion channels, which reflects a 3-times increase in gating activation rates for each 10°C increased[26]. On the other hand, the Q_{10} for conductance is comparably less temperature-sensitive, usually presenting values of around 1.2 to 1.5[26].

The variation with temperature for the maximum channel conductances can be calculated in a similar way as above. For a specific ion X, if the maximum conductance at one temperature is $\bar{g}_X(T_1)$, at another temperature it will be given by[17]:

$$\bar{g}_X(T_2) = \bar{g}_X(T_1)Q_{10}^{\frac{T_2-T_1}{10}}. \tag{13}$$

2.1.4 Thermo Sensitive Ion Channels

Although ion channels are ubiquitously influenced by the thermal conditions of its environment, some classes of these proteins are distinctively suited for perception of temperature variations.

2.1.4.1   Transient Receptor Potential ion channels

The mammalian transient receptor potential (TRP) family of ion channels consists of 28 proteins that have been described in barely all body tissues and are known to play a key role in the interpretation of environmental or endogenous stimuli[27]. TRPs are cationic channels with varying ion selectivity profiles that act as a transducer for such inputs by generating cell depolarization through the modulation of intracellular ionic concentrations. In fact, most TRP channels are characterized as polymodal, i.e., prone to activation by more than one type of stimuli.

The discovery of the TRP family started when, in 1969, a fruit fly *Drosophila* spontaneous mutant was observed to be transiently sensitive to light stimuli in contrast to the steady response typical to the wild type counterparts - blindness in the presence of constant bright light. This atypical response was found to stem from a malfunctioning ion channel and triggered the search for proteins with similar functions[27]. Hitherto, 6 mammalian subfamilies have been identified: TRPC (canonical), TRPV (vanilloid), TRPM (melastatin), TRPP (poly-cystin), TRPML (mucolipin) and TRPA (ankyrin). In general, these are assembled as six transmembrane domains (S1-S6), with a pore-forming loop between S5 and S6, and N- and C- intracellular termini (Figure 4).

Some TRPs can be functionally distinguished as thermosensitive, covering responsiveness to a wide range of temperatures. The vanilloid TRP channels are especially relevant in this context as some of its members present Q10 values ranging from 10 to 40[28]. Initially, TRPVs were believed to be thoroughly thermosensitive, however, and although TRPV2-6 present more than 50% homology to TRPV1, they do not all react to temperature[27]. TRPV1-4 are all thermosensitive nonselective cationic channels and can be found in the CNS, whereas TRPV5 and TRPV6 are unresponsive to heat, highly selective for calcium and there is no evidence for their expression in the CNS[27,29].

The founding member of this subfamily, TRPV1, was first reported as responsive to the active ingredient in chilies, capsaicin, a vanilloid-like molecule, hence the name. Although these are mostly represented in nerve extremities and accepted to assume a nociceptive function, including temperatures in the noxious range (>42)[29], higher densities of these channels have also been reported in brain neuronal populations, with a role in excitation[30]. Channels encoded by *trpv1* gene in hypothalamic vasopressin neurons were shown to be intrinsically thermosensitive both *in vitro* and *in vivo*[31]. This conclusion stems

from the observation that an hyperthermic state was associated with depolarization and an increase in AP firing rate of central vasopressin neurons. Additionally, *trpv1* knock-out mice were unable to elicit a typical vasopressin response, which is involved in the thermoregulatory response to hyperthermia, therefore eliciting their thermosensitive contribution to homeostasis. However, TRPV1 knockout mice are apparently unaffected in their capability to sense acute heat stimuli, meaning that TRPV1 is not the sole heat receptor.

2.1.4.2 TRPV4 is associated with modulation of activity due to temperature changes in hippocampal pyramidal neurons

Another relevant thermosensor in this family is TRPV4, which has a Q10 of ~20[32]. It is described in the literature to be affected by temperatures in the range of ~25 to ~40°C, according to different cell types. Remarkably, this ion channel is widely expressed in membranes spanning most bodily systems, epithelia, musculoskeletal tissues and vasculature[33]. TRPV4 has been shown to accumulate in the soma of immature hippocampal neurons but not at post-synaptic locations[34]. However, during maturation, these would start to exhibit TRPV4 clusters in the dendrites and post-synaptic locations. Furthermore, TRPV4 in dissociated hippocampal pyramidal neurons has been described to be activated at temperatures approaching physiological values (almost 34°C)[35]. Interestingly, studies in humans determined 33°C as a critical temperature for brain functioning as temperatures below would start to cause cognitive dysfunctions[36].
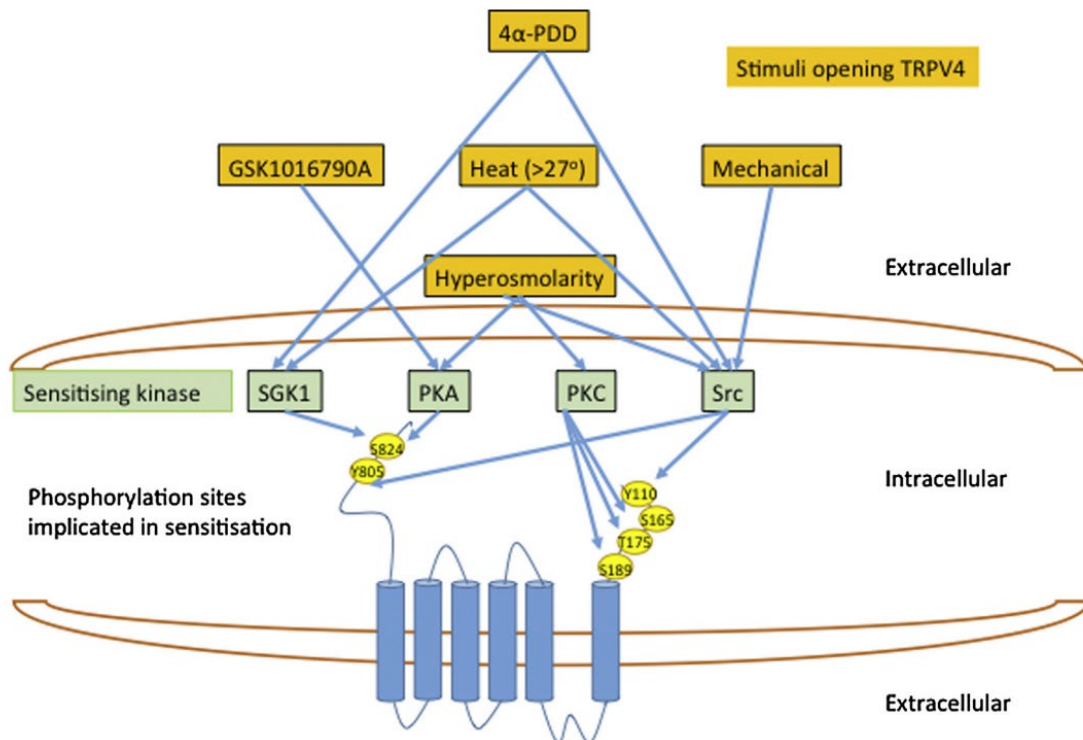
Figure 4 – The effect on TRPV4 by diverse stimuli is sensitized by protein kinases.

TRPV4 displays the typical structure of TRPs, with 6 transmembrane domains (S1-S6, from left to right) and a pore between S5 and S6. The different stimuli shown in orange boxes are associated with different sensitizing protein kinases, in green, by connecting arrows. Furthermore, arrows also indicate what motifs the protein kinases affect in TRPV4. The sensitizing protein kinases include serum glucocorticoid protein kinase-1 (SGK-1), cyclic-AMP dependent protein kinase A (PKA), protein kinase C (PKC) and SRC family kinases (SRC). Adapted from Darby et al, 2016[37].

TRPV4 is encoded by the canonical sequence and consists of 871aa. It is nonselective for cations but presents higher permeability for calcium ions[38]. This selectivity is modulated at the pore formed between S5 and S6 by the residues Asp672 and Asp682. Similarly to other members of the vanilloid subfamily, the N- terminus of TRPV4 consists of six ankyrin repeat domains (ARDs), which modulate protein-protein interactions, as well as interactions with activation ligands such as phosphatidylinositol-4,5-biphosphate (PIP$_2$) and calmodulin[32]. Before the first ARD locates a proline-rich domain, which is implicated in mechanosensitivity and cytoskeletal remodeling. On the other hand, the C- terminus contains other functional domains such as a TRP box, a calmodulin-binding site, and a PDZ-binding like motif. Gain and loss of function mutations in the TRPV4 gene are linked to several inherited human diseases[39]. The range of mutable motifs results in highly variable phenotypes, including skeletal dysplasias, such as congenital distal spinal muscle atrophy and scapuloperoneal spinal muscular atrophy, and sensorimotor neuropathies, alike Charcot-Marie-Tooth disease type 2C, which is characterized by vocal cord paralysis, compromised respiratory and urinary functioning, as well as hearing loss.

Regarding animal models for translational studies, there exist knockout mice for TRPV4[32]. These are characterized by significantly decreased theta-frequency electroencephalography (EEG) activity when compared with wildtype mice. Additionally, TRPV4KO mice are fertile animals but carriers of multiple altered phenotypes, including reduced water intake and larger bladder capacity, higher blood osmolality and impaired vascular function, as well as compromised responsiveness to thermal and mechanical stimuli. Interestingly, compared to the wild-type counterparts, these mice are resistant to obesity when fed on a high-fat diet, even with similar rationing and physical activity. Furthermore, in behavioral tests, these specimens have shown reduced depression-like and social behaviors[40].

Although TRPV4 was initially described as an osmosensor, it is now also known to be responsive to mechanical signals, alongside temperature (Figure 4). The synergistic effects of different stimuli on TRPV4 activation has been studied for the combination of temperature with other stimuli. Remarkably, TRPV4 response to heat is exacerbated in hypoosmotic solutions and reduced in hyperosmotic solutions[41]. More recently, temperature has been shown to play an exacerbating role in mechano-sensitivity of TRPV4 in Müller glial cells, as cells at physiological temperature had a significantly potentiated mechanosensing activity of TRPV4 when compared to cells at 25°C[42].

Additionally, until now, 38 TRPV4-binding proteins have been identified, covering functions in the regulation of its activation, heteromerization, ubiquitination and trafficking[32]. Initial reports of unsuccessful heat activation in inside-out patches of HEK293 cells lead to hypothesize on the dependence of endogenous signals for heat activation[43]. This was later confirmed as TRPV4 activation was completely recovered in the presence of PIP_2[44]. Furthermore, a mechanism by which heat activates TRPV4 seemingly lies on an aromatic residue at the N-terminus of S3[45]. The replacement of Tyr-555 with phenylalanine did not affect the heat activation of TRPV4 but, when replaced by Alanine the response was strongly impaired. Furthermore, the same study uncovers the independent activation of TRPV4 by different stimuli by showing that knock-out cells for Tyr-555 were still responsive to hypotonicity. Additionally, mutations in other aromatic and hydrophobic residues spanning subunits 4 to 6 have been correlated with a decrease in TRPV4 sensitivity to heat[46,47]. Several studies have covered the role of post-translation modification of TRPV4 by enzymatic agents and its sensitizing effects on a range of different stimuli. Remarkably, sensitization to heat has been described by two additional mechanisms, phosphorylation of the residue Ser 824 of TRPV4 by a SGK1 and the phosphorylation of tyrosine 110 and 805 by Src[48,49].

RN1734 was the first identified antagonist of TRPV4, seemingly inhibiting the 4α-PDD mediated activation, which follows the same post-translational mechanism as heat activation, as seen in Figure 4[50]. It has an IC_{50} in the range of 2-6 μM and, notably, displays a high selectivity profile for TRPV4 over other TRP channels. However, it may have off-target effects when at higher concentrations. In a study of the regulatory effect of TRPV4 in the GABA-activated current (I_{GABA}) in hippocampal pyramidal neurons, the addition of RN1734 was shown to block almost completely the inhibition of I_{GABA} caused by TRPV4 agonists[51]. Furthermore, the application of TRPV4 agonists has also been shown to significantly reduce the delayed rectifier potassium current in hippocampal pyramidal neurons but, such effect was also blocked by the addition of TRPV4[52].

Shibasaki et al. have produced a series of highly relevant studies for the understanding of TRPV4 temperature regulation in neuronal populations. In their initial approach, using patch-clamp technology, the group described in dissociated hippocampal neurons how, at around 33°C, there is an increase in intracellular calcium concentration, which is not seen in the absence of extracellular calcium or the presence of ruthenium red, a pan-TRP inhibitor. Furthermore, they quantified the resting membrane potential in wildtype and TRPV4KO cells at 25°C and 37°C and, while indistinguishable at the first temperature, wildtype neurons presented more depolarized at 37°C (~5.7mV). Accordingly, ruthenium red was applied to wildtype cells and a hyperpolarization of the resting membrane potential by ~5.0mV, similar with the difference between wildtype and TRPV4KO, supported the involvement of TRPV4. Finally, the authors observed that, for the

same current injection, the 5mV depolarization of the resting membrane potential lead to repetitive action potentials in wildtype neurons, whereas only a few were seen in TRPV4KO cells, even though the cells had indistinguishable dendritic morphology, synaptic marker clustering and synaptic currents.

The same group has studied the association of TRPV4 with temperature variations and different disorders. In one study, the authors developed an *in vitro* model of ischemic stroke-induced edema where it was observed that hyperthermia induced swelling via TRPV4 activation and, subsequently, that brain edema following acute brain injury was repressed in TRPV4KO male mice *in vivo*[53]. More recently, they generated both wildtype and TRPV4KO mice models of partial epilepsy and detected larger frequencies of epileptic EEG in wildtype mice, indicating the involvement of TRPV4 in epilepsy progression[54]. Additionally, it was detected that the temperature in epileptogenic zones was significantly increased by 1°C in comparison to control mice, which could explain the increased frequency of epileptic discharges due to neuronal hyperactivity. To assess the effect of TRPV4, the authors employed a brain cooling treatment, which resulted in a more substantial reduction of epileptic discharges in wildtype than TRPV4KO, suggesting that TRPV4 activation exacerbates epilepsy, but there are also TRPV4-independent mechanisms involved. Finally, the injection of a TRPV4-specific inhibitor into the epileptogenic zone significantly decreased epileptic frequency and amplitude in wildtype, but not in TRPV4KO individuals. Both studies support the relevance of TRPV4 in the impact of heat on neuronal activity and its inhibition as a mechanism for neuroprotection in different temperature-related disorders.

2.2   Recording neuronal activity

The hope to decipher the bioelectrical code underlying human nature is a most significant driving force motivating scientists for the development of new technologies. A fundamental work in the origins of electrophysiology comes from Luigi Galvani in the end of the 18th century[55,56]. He applied the term "animal electricity" for the results of his experiments, where he studied the behavior of the inferior limbs of dissected frogs when submitted to electrical stimulation. In these, he reported on the relationship between the intensity of stimulation and muscle contraction, the refractory phenomenon and also the first demonstration of the propagation of an action potential by attaching the sciatic nerve of two frog legs and observing that the stimulation of one, results in muscle contraction of both. Additionally, he speculated on the disequilibrium of charges in the neuronal tissue and the necessary existence of specific pathways for electric current flow.

About a century later, scientists started adventuring on the *in vivo* observation of electrical activity in the living brain[57] and, in 1929, Hans Berger reported on the first EEG and the non-invasive recording of electrical activity in the human brain[58]. Although the EEG

and other recording techniques such as magnetoencephalography and functional magnetic resonance imaging present a valuable tool for the study of some diseases and responsiveness to stimuli, its functionalities are limited by a low spatial resolution[59,60]. Additionally, the experimental freedom of *in vivo* investigations of the brain is strictly hindered by practical and ethical limitations, favoring the use of representative simpler models[5].

The creation of the voltage-clamp technique allowed for the pioneering works of Hodgkin and Huxley to culminate in the ionic theory of membrane excitation[55,61]. Their quantification of ionic currents across putative ion channels was confirmed with the development of the patch clamp technique, by Neher and Sakmann, in the late 1970s[62]. In this method, an electrode inside of a glass micropipette filled with an electrolyte solution is brought to close contact with a tiny patch of membrane of an isolated cell[62]. The presence of another electrode in the bath solution surrounding the cell serves as a reference for recording the potential inside of the cell. Additionally, the solution filling the pipette and the bath can be modulated according to the endpoint of the experiment and, as in the voltage-clamp technique, this method grants experimental control of the membrane potential, which allows the characterization of voltage dependent membrane currents[55,61,63]. This method can be modulated for a range of possible configurations in order to offer different insights at a cellular, or single ion channel level[2,63]. When sufficient suction is applied to rupture the membrane and the electrode is directly connected to the intracellular space of the cell, the configuration is called a whole-cell patch clamp and it is possible to measure the overall electrical properties of the membrane. Although this technique is undeniably essential for electrophysiology, it is technically challenging to implement and unfeasible for stimulation and recording of hundreds of individual neurons simultaneously. Moreover, membrane rupture for intracellular recordings can change the internal media and, along with stimulation, it causes a great impact in the cell viability, rendering it impossible for long-term studies[63]. A way to overcome the limitations imposed by this technique relies on the utilization of non-invasive, extracellular MEAs that enable long-term recordings and stimulation of large cell populations[7].

2.2.1 Microelectrode Arrays

The first MEA was introduced by Thomas et al. in 1972[64]. The authors' aim was to design an approach that could capture long-term (days or weeks), multisite electrical activity in a convenient, non-invasive manner. Thus, a 2 by 15 array of 30 microelectrodes was created and tested by recording events on cultured embryonic chick heart cells. In 1980, Pine[65] reported on the correlation of simultaneous recordings of intracellular and extracellular action potentials, further establishing the MEA recording technique as valuable tool for the study of the dynamics of neuronal cultures. In this study, the activity of dissociated rat superior cervical ganglion neurons was recorded with a newly-developed

MEA with 32 microelectrodes that could capture signals of cells at a maximal distance of 40 μm from the electrode, with a good signal-to-noise ratio (SNR). To allow for the correlation, individual cells near electrodes were recorded and stimulated with a penetrating intracellular micropipette. In the following years, the increasing reports on MEAs usage was noticeable and, alongside an overall technological and scientific progress, also was their quality and efficacy[66,67]. The first commercially available MEA systems appeared in the 1990s and, although some researchers build their own accordingly to specific experimental purposes, many resort to these well-established, commercial models (Figure 5).

MEAs are the result of a carefully designed process of micro-fabrication, consisting in a layered composition of microelectrodes, insulator and conductor layers, and a substrate[6,7,56,68]. The choice of materials is of utmost importance, not only for the best efficacy in signal acquisition but also considering the necessary close contact with the type of biological tissue to be recorded. Therefore, and ideally, these should all be nontoxic, and present good biocompatibility and adhesive properties. The electrodes are made of corrosion-resistant metals such as gold (Au), platinum (Pt) or titanium nitride (TiN), which prolongs the life, and allows for reuse, of MEAs. Each electrode diameter usually ranges between a few tens of micrometers, and these are insulated from each other, for example by silicon nitride (SiN). Finally, the substrate is typically made of a material like glass, which allows for good transparency and the observation of live cells under conventional microscopy.

Since the pioneering studies, planar MEAs have been employed for multiple types of neural network preparations ranging from dissociated cell cultures to organotypic cultures and acute brain slices[68]. These extracellular microelectrodes can capture both local field potentials (LFPs), which reflect the electric potential of the media, and extracellular action potentials (EAP), the abrupt changes in the extracellular potential caused by a spike in a near cell[7]. Apart from passive recording, MEAs are also capable of enticing and control neuronal activity by the delivery of targeted electrical stimuli. The fact that these are not induced directly in the cell represents one advantage of these systems, as it prolongs their viability. Furthermore, when environmental variables such as temperature and pH are controlled, cultured neurons can maintain an electrically active network for more than a month[68]. Thus, this technology offers a convenient spatiotemporal recording platform suited for a range of applications including neurotoxic drug testing, characterization of single-unit and network neuronal activity, and synaptic plasticity. However, these systems also present some disadvantages comparatively to intracellular ones[56]. They record only extracellular signals and, as the coupling between the cell and the electrode is weaker, the SNR is far inferior.
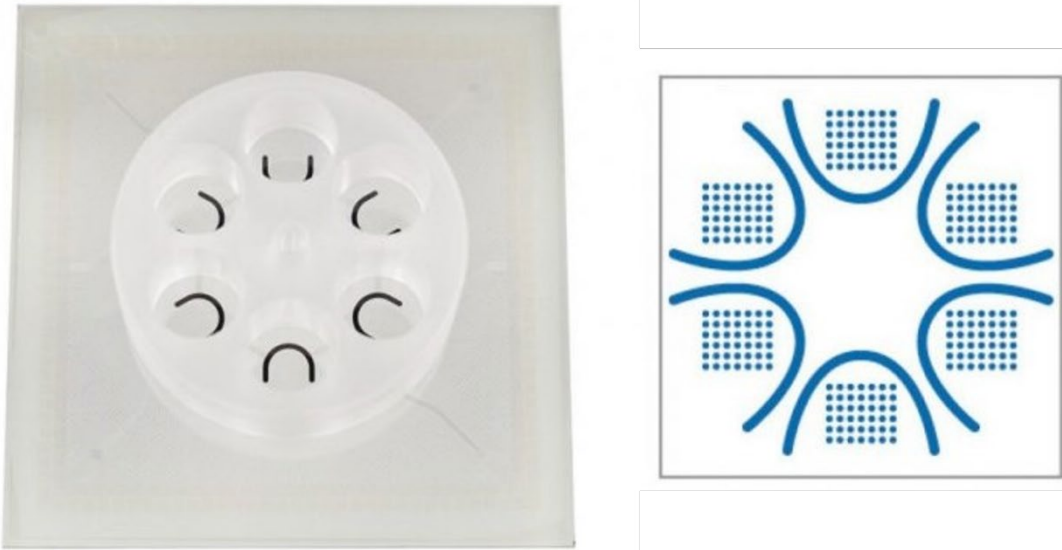
Figure 5 – Commercially available 6-well MEA from Multi Channel Systems used on this work.
6-well MEAs have six separate culture chambers, each with 42 recording electrodes. From Multi Channels Systems (https://www.multichannelsystems.com).

2.2.2 Extracellular Action Potential

The extracellular potential V_{out} of a spiking neuron modeled as a point source can be approximated from Coulomb's law[69,70]:

$$V_{out} = \frac{I}{4\pi D\sigma},$$
(14)

where I is the amplitude of the point source current, σ symbolizes the conductivity of the extracellular space, and D represents the distance from the source to the recording point. However, considering the propagation of the action potential along the axon, whose length is significantly superior to the transactional radius, a model resembling a cylinder would better approximate the extracellular potential arising from a neuron than a point source. Thus, the line source approximation (LSA), which simplifies the three-dimensional representation of the distribution of membrane current, gives the following solution for the extracellular potential[69,70]:

$$V_{out} = \frac{I}{4\pi\sigma\Delta s} \log \left| \frac{\sqrt{h^2 + r^2} - h}{\sqrt{l^2 + r^2} - l} \right|,$$
(15)

where Δs is the length of the axon, r is the radial distance from the axon, h is the longitudinal distance from the end of the axon, and $l = h + \Delta s$ is the longitudinal distance from the origin of the axon. In a practical sense, the wave form of the EAP will assume varying shapes depending on the position of the neuron and its relative position to the electrode. This

perspective is easier to understand through the work of Gold et al.[71], where a model of the time course of the extracellular potential during an action potential is simulated with the NEURON simulation environment[72] (Figure 6). Additionally, *in vivo* simultaneous recordings of intracellular and extracellular activity of CA1 pyramidal neurons are compared with the predictions from the model, which is based on the same cells and includes 12 different voltage-gated ion channels modeled using the HH formalism[71].
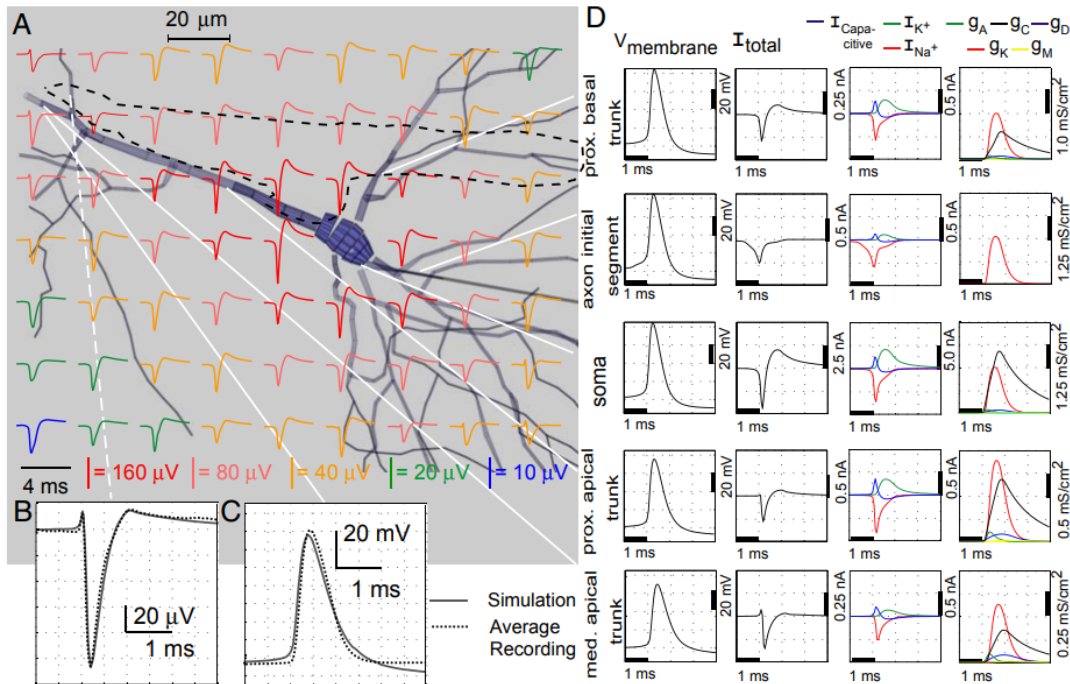
Figure 6 - Simultaneous recording and simulation of intracellular and extracellular activity of CA1 pyramidal neurons.
A) EAPs in the diagonal section crossing the soma and the location of the electrode (black dotted line). B) Comparison of the EAP simulated for the estimated electrode position and the recording. C) Comparison of recorded and simulated intracellular potential in the proximal apical trunk. D) Details of simulation for each compartment. First column represent the membrane potential for each location, while the second column gives the shape of the membrane current. Third column corresponds to the role of the current of different ions in the formation of the action potential. The three distinct phases of the EAP result from the changing dominance of ion currents. The last column represents the conductivity for the current of these ions. Adapted from Gold et al, 2006[71].

Figure 6(A) displays a grid of EAPs relative to the position of the neuron and it can be seen that the shape of the waveform is proportional to the total membrane current, I$_{total}$, represented in the second column of Figure 6(D), for the corresponding compartment, indicated by the white line directed at the respective row. Figure 6(B) is composed by two representations of an EAP, one real and one simulated. The black dotted line presents an enlarged image of the EAP the location indicated by the white dotted line in Figure 6(A) and how the simulated EAP (black line) can be superimposed. It is noticeable that the shape of the EAP shows three distinct phases, a brief positive peak, a sharp negative peak, and a longer positive period, slowly decaying back to rest. This triphasic shape is predicted by the model of sinks and sources for the flow of current in the extracellular environment[73]. When an axonal membrane is depolarized, it creates a potential difference between the

depolarized region and the neighboring resting zone, causing current to flow inward to the depolarized, or sink region. Thus, if there is an electrode adjacent to the axon in the sink region, it will capture a negative signal comparing to another distant electrode. On the other hand, the source corresponds to the neighboring area of the sink region and provides a source of current in that direction. Therefore, if there was an electrode adjacent to this area, it would record a positive signal in comparison to another distant electrode. Finally, the triphasic shape of the EAP can be explained by the propagation of the sink, represented by minus signs, along the axon membrane as exemplified, in a purely illustrative way, in Figure 7[73]. If there is a stationary electrode adjacent to the axon, towards which the action potential is propagating, it will first capture a positive signal resulting from the source region. Then, a negative potential is recorded as the sink region arrives the position close to the electrode until, at last, the membrane repolarizes, serving once again as a source and providing a positive signal.
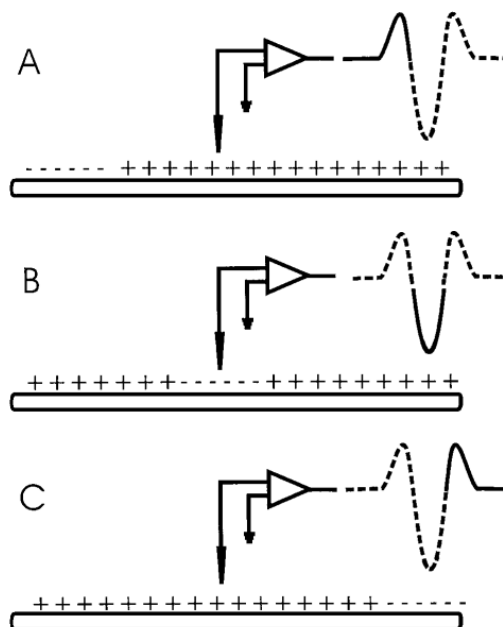
Figure 7 – Representation of the triphasic waveform of the EAP generated by the source and sink model in an isolated neuron.
(A) The region underneath the electrode is acting as a source and therefore records a positive potential comparing to a distant reference electrode. An AP can be seen approaching this area from the left, represented with minus signals. (B) When the membrane depolarization reaches the region of the recording electrode, a negative potential is recorded. (C) After the passage of the AP, the recorded region acts once again as a source, resulting in a positive potential. Adapted from Heinricher, 2004[73].

The simultaneous recording of intracellular and extracellular potentials from a motor neuron of cat ventral horn is presented in Figure 8[74]. One can observe the complementing shapes of the peaks and how the long positive period in the EAP corresponds to membrane repolarization. It is important to remark the different scales for both recordings. Since intracellular action potentials can only be detected intracellularly, the recording signal is considerably stronger than for an EAP, which, as shown in Figure 6 and

described in (15), gets weaker with distance from the cell. Thus, to appropriately detect an EAP, the electrode should be in a closely surrounding area of the spike origin (<100μm)[7].
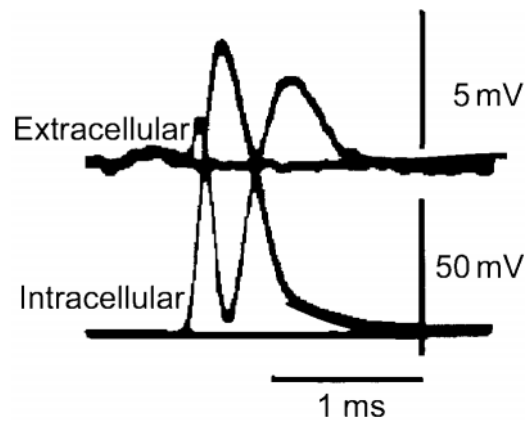
Figure 8 – Simultaneous intra- and extracellular recordings of a spike showing the temporal relation of the recorded potentials.
The difference in scale of the two recordings should be noticed. Adapted from Terzuolo and Araki, 1961[74].

2.2.3   Technical Considerations of MEA based recordings

2.2.1.1   Noise and Signal to Noise Ratio

The SNR ratio can be simply defined as the comparison between the level of a desired signal, the meaningful information, to the level of background noise. It is a key measurement for the quantification of the performance of electrophysiological recording devices and, thus, an overall goal of MEA fabrication methodologies consists in achieving higher SNR values, with a typical target ratio of 5:1 or higher[7]. There are, for example, several methods described for the modulation of electrode impedance values during MEA production, as attaining low electrode impedance translates in higher SNRs[6]. Accordingly, it is utterly important to uncover and distinguish all possible sources of noise, understanding how and when it interferes with the signal, and ultimately allowing for the development of proper solutions.

- Biological noise

The electrode recording environment, either physiological or physiologically simulated, sustains electrical activity that may go beyond the ideally desired for direct analysis. This biological, or background noise, reflects the presence of electrical activity of other nearby cells, ionic activity, and also synaptic noise resulting from the inherently random nature of synapses. Therefore, the development of models that better simulate the variables that affect recording quality allow for a performance improvement of spike sorting

algorithms[75–77]. In such cases, the LFP is usually considered as background noise and so filtered out[7].

- Electrode-electrolyte interface noise.

Another source of noise arises from the liquid-metal interface. At frequencies below 10 Hz, charge and mass transfer processes in the electrode generate noise with a steep roll of $1/f$ or even $1/f^2$ [78]. Whereas for higher frequencies, more relevant to electrophysiology, thermal noise has been shown to play a bigger part[79].

- Device noise

The design of the amplifier system, especially the front-end amplifier, should be carefully planned as it presents another source of noise. So, the aim is to guarantee that the signal acquisition system does not hinder the performance of the system due to noise[7]. Another hardware concern relies on the design of the analog-to-digital conversion (ADC) system. It originates quantization noise as a consequence of the signal discretization error. It is usually approximated as $1/\sqrt{12}$ times the magnitude of the least significant bit. The minimal resolution for the ADC in a MEA is typically 8-bit but, if the system employs an off-chip ADC, the resolution is usually 16-bit or higher[7]. Finally, the power supply also provides noise in the 50/60 Hz bandwidth, which is mainly picked up at the connection between the electrode and the amplifier, due to the latter's high impedance for that range of frequencies[80]. Thus, a common strategy to reduce this type of noise consists in minimizing the distance between the electrode and the amplifier.

2.2.1.2   Effect of electrode size and density

Larger electrodes have a higher probability of being physically closer to neurons and capture higher-amplitude spikes[81]. At the same time, these electrodes can capture signals from more neurons simultaneously[82], which will result in a lower SNR. This effect is termed spatial averaging and reflects the blurring of high-amplitude, localized events with nearby small amplitude signals[83]. Additionally, size variation also has an impact in the impedance of an electrode and, consequently, in signal-attenuation, which is measured as the ratio between the impedance of the electrode and the amplifier[7]. In practice, electrode size is inversely proportional with signal-attenuation[83,84]. The probability of an electrode to be at the right spot to provide an optimal measure of EAPs can be solved with two possible strategies[83]. Considering the aspects discussed above, one can either resort to large electrodes, which have a higher probability of being near the activity source and, therefore, capture higher-amplitude signals, but at the expense of averaging the signal of various neurons. Or rely on dense arrays of smaller electrodes, which suffer a higher signal-

attenuation, but possess an increased probability of one to be in the right spot and show reduced averaging effect.

Finally, the size of electrodes has been reported in a wide range throughout literature, varying from 5 to 120 μm in diameter[68]. More recently, Viswam et al.[83] reported a combined experimental and computational approach that elucidates on the matter using dissociated cell cultures and both organotypic and acute brain slices. Their results point out a dependence according to the nature of the signal, the relative position between the electrode and the signal, and the level of background activity. In sum, for small, localized axonal EAPs, the ideal size ranges between 1 μm x 1 μm to 16 μm x 16 μm, whereas for large perisomatic EAPs, it would be around 8 μm x 8 μm to 32 μm x 32 μm.

2.2.4 Analysis of MEA electrophysiological data - extracting relevant metrics

The treatment and processing of raw data obtained from MEAs is necessary as it allows the extraction of relevant electrophysiological information from otherwise distorted, convoluted, and noisy signals[70]. In the first place, the raw data needs to be filtered as a way to obtain higher SNR and reduce false positive rates. This can be achieved by applying a bandpass filter, usually with bandwidth of 200 - 3500 Hz, which allows the removal of low-frequency components such as LFPs and noise. It should be noted that filtering can result in an alteration of the shape of the detected EAP due to the addition of phase distortion.

Spikes are the main unit underlying activity-describing metrics and, therefore, spike detection reflects a fundamental process. The most common method relies on using an amplitude threshold, which the signal has to cross to be considered a spike[85]. A high threshold value can result in the exclusion of valid spikes, while the choice of a low threshold is more probable to capture all significant events, but at the expense of also detecting false positives. Thus, it may not be a good option to choose an absolute potential value, but instead, use a threshold relative to a number, n, of standard deviations (SD) above the root mean square (RMS) of the baseline noise[7,16]. Typically, n is calculated dynamically over 500 ms and the threshold used in most studies range from 5 to 6 SD, though values of just 3 SD or up to 8 SD have been reported. Finally, after spike detection there is usually a phase of spike sorting in signal processing methods, allowing the categorization of spikes due to their shape and the identification of neuronal networks accordingly. However, this process is not relevant in the context of this work, which relies on the characterization of the longitudinal patterns of spikes. Mean firing rate (MFR) describes the ratio of total spike counting to the duration of the recording. Novellino et al. described the MFR as the best metric to represent electrophysiological activity in toxicology studies[10]. In this study, the methods of tissue culture, activity recording, and analysis were compared between

different laboratories. Among other parameters tested, MFR was found to be the most consistent metric of activity due to its pharmaco-sensitivity, easiness to extract, robustness, and effectiveness independently of the method applied by each laboratory. Accordingly, the use of this metric has been the most commonly reported in the methodology of MEA experiments[16].

A burst is a phenomenon that describes intermittent periods of increased spiking activity. These episodes can be either characterized in a single neuron, and it has been established how different phenotypes provide different bursting behaviors, or as a simultaneous activity across a neuronal network[86]. Bursting activity has been associated with several physiological functions such as information transport, as it is believed to be a more efficient method than single spikes, motor pattern generation, and network development and synchronicity in dissociated cell cultures. Additionally, it has been associated with memory, reward-oriented and exploratory behaviors *in vivo*, as well as a relevant information for the study of pathological conditions. There is still a lack of agreement towards the correct description of a burst and, although there are several techniques proposed to the identification of these, there is no single method that has been widely implemented. Some of these techniques rely, for example, in imposing a threshold for the interspike interval (ISI), which, similarly to the case of spike detection, improves when the applied parameters are adaptively chosen. Several other parameters can be analyzed as a function of spiking and bursting, depending on the experiment to be made[87]. These include the duration of a burst, the number of spikes in a burst and the ratio of these against all spikes, the interburst interval (IBI), and more complex measures regarding network function.

2.3   Practical Applications of MEAs

Owing to the electrical excitability of neurons, MEAs have been applied in a wide range of experimental designs in order to better understand the mechanisms underlying how the nervous system works. The observation of the evolving electrical activity, throughout time, in cultured neuronal populations, allows for a better gasp at temporal signatures of the developmental process of neuronal networks[15]. These networks of interconnected neurons usually display synchronous and oscillatory behavior, which are altered in the existence of pathological conditions such as epilepsy, autism, schizophrenia, and other neurological diseases. Furthermore, the nervous system is also especially sensitive to drugs, toxins, and other chemicals. Thus, MEAs have been widely used as a way to evaluate how different compounds alter neuronal communication, providing a powerful tool for screening such compounds in their potential to induce neurotoxicity or developmental neurotoxicity[88]. Apart from the observations of biochemical neuroactive agents, MEAs also offer a valuable tool to better understand how other variables, imposed

by our physiological boundaries, regulate the nervous system. As explained before, temperature has an undeniable impact in the generation and propagation of APs. There are several clinical conditions characterized by a temperature impact. For example, excessive exposure to high temperatures can lead to a heat stroke. Extreme febrile and hyperthermic states result in impairments in the regulation of body temperature. Additionally, it can also be caused by the consumption of certain compounds, such as some neuroactive agents. Thus, it is fundamental to further understand the influence of temperature variations in neuronal activity.

In a recent study, Zwartsen et al. reported on the exacerbation effect of an hyperthermic state in the alterations of neuronal activity caused by psychoactive drugs in vitro[89]. Cortical rat neurons were cultured and grown on MEAs, and the pipeline of the experiment consisted of the observation of the effect of acute (30 min) and prolonged (4.5 h) drug exposure, at 37°C and 41°C, and a following 19 h period, at 37°C, of drug washout before a final recovery measurement. At 37°C, both acute and extended exposure to relevant doses for recreational use of cocaine, MDMA and TFMP inhibited neuronal activity. While at 41°C, also methamphetamine produced an inhibitory effect, and these were in general more pronounced, and less prone to fully recover when compared to normothermia.

Nevertheless, the first outcome of this study, regarding temperature-evoked differences in neuronal activity, is a remarkable contribution to the field since the information available concerning the sole effect of hyperthermia in the electrical activity of neurons *in vitro* is scarce. After an acute exposure to an increased temperature, a significant reduction in weighted MFR, weighted mean burst rate (wMBR) and weighted mean network burst rate (wMNBR) can be seen. Accordingly, but to a lesser degree, the (network) burst duration and ISI between (network) bursts also decreased. This tendency was only counteracted by a significant increase in the (network) IBI and its variation coefficient, which is a measure of burst rhythmicity. At the end of the prolonged exposure, the neuronal activity at 41°C was mainly similar to the observations after acute exposure, while at 37°C several parameters were altered, especially regarding burst activity. Notably, after the recovering period, both conditions converged to a similar pattern, with a significant change in IBI, (network) burst duration, and network ISI[89].

Another relevant study showed that a temperature increase to up to 40°C was reported to cause spreading depressions in rat hippocampal slices *in vitro*[90]. These are characterized by reduced spontaneous electrical activity, slow ion flow across the membrane, and negative potential changes.

2.3.1 Impaired thermoregulation

Body temperature is controlled by the brain. It integrates the sensorial inputs of the environment and subsequently applies adapting effector mechanisms in order to

produce, maintain or dissipate heat[91]. Nevertheless, since considerable amounts of heat are generated by the high levels of neuronal and metabolic activity, the brain itself is tightly regulated to maintain its own homeostasis. Thermorecording studies conducted in rodents, cats, dogs, and primates reveal a relatively large range of physiological variations in brain temperature, from 3 to 4°C[91]. Interestingly, it has been shown in mice that the body temperature between a sleeping state and wakefulness increases by around 2°C, whereas brain temperature only increases by around 0.8°C[54]. However, in situations of increased bodily heat production and/or insufficient heat dissipation, temperatures can rise above physiological limits, resulting in a state of hyperthermia.

The CNS is known to be particularly vulnerable to hyperthermia. This rise in temperature can have infective and non-infective causes and worse clinical outcomes are usually associated with the duration of the episode, as well as with higher temperatures[11]. Non-infective manifestations may result from drug intake or heat illness, which is associated with extreme environmental conditions or demanding physical activity. The cellular mechanisms by which elevated temperatures induce neuronal clinical repercussions are unclear but are likely to be the consequence of a combination of factors, including the production of reactive oxygen species, hypoxia, and excitotoxicity. Hyperthermia can boost tissue metabolic rate, increasing the production of reactive oxygen species, and lower oxygen solubility, possibly resulting in hypoxia, which is specially a problem in *in vitro* preparations where oxygenation may already be minor[92]. Excitotoxicity is caused by excessive exposure to excitatory neurotransmitters, such as glutamate[11], which can turn neurons more passive towards calcium influx, thus altering electrochemical gradients.

The clinical outcomes associated with elevated body temperatures involve neuronal dysfunction, seizures, irreversible brain damage, coma, and death. Even acute and mild cases can cause cognitive impairment, which may, in some instances, turn permanent. The most common long-lasting dysfunctions associated with hyperthermia occur in the cerebellum[11]. Although hyperthermia and fever do not encompass the same molecular processes in the induction of increased brain temperature, both can cause seizures. Febrile seizures result from infection-induced fevers that go above 38°C and represent the most common cause of seizure in young children, affecting 3 to 5% of the pediatric population. Furthermore, magnetic resonance imaging shows occasional evidence of hippocampal atrophy after prolonged and local febrile convulsions[93]. Animal models have shown that seizures can be induced during development without necessarily being affected by infection, therefore implying that seizures can be triggered solely by a temperature increase in the developing brain[94]. Both *in vitro* and *in vivo* studies point to a hyperthermia-induced hippocampal modification of neuronal excitability in immature rats, which may facilitate the development of epilepsy later in life[95,96].

Currently, the standard of care for conditions characterized by disrupted thermoregulation consists in targeted temperature management, which comprises distinct strategies aiming to maintain a specific body temperature, along with medication[97]. Therapeutic hypothermia is the most effective neuroprotective strategy and has been employed in response to hyperthermic and hyperpyretic clinical scenarios resulting, for example, from ischemic strokes, traumatic brain and spinal cord injury, heat stroke, or infections of the CNS. This strategy may exert its therapeutic effects through different mechanisms, such as reduced brain inflammation and intracranial pressure, decreased brain cell apoptosis induction and necrosis, diminished production of free radicals and overall brain metabolism. An interesting remark can be done about the study reported by Curran et al.[98], where they evaluated the effect of high temperatures in children within the autism disorder spectrum. Apparently, during febrile states, some children display less unusual behavior, which may imply a beneficial effect in the compromised neuronal activity sustained during disorder development.

Chapter 3

Materials and Methods

3.1 Electrophysiological system overview

Multi-Channel Systems (MCS, Reutlingen, Germany) is one popular choice of manufacturer for electrophysiology systems that, along with *in vivo* and patch clamp systems, provides systems for the *in vitro* analysis of extracellular recordings.

This project was conducted using solely the MEA2100-System, which comprises two main components, a headstage and an interface board. The headstage (Figure 9(1)) is the core element of the system as it houses the MEA, and is responsible for data acquisition, signal amplification and also contains a stimulus generator to enable the targeted stimulation of the culture. Amplification is performed before the acquisition by an amplifier built-in the headstage, which is closer to the source and therefore ensures low noise levels. The system has a default hardware gain of 10 and a large resolution of 24 bits. It has an integrated A/D converter which allows data acquisition with changeable parameters through the software. The MEA2100-System is considered the most flexible system of the bunch, considering it offers various contact units for different MEAs (Figure 9(5)), with changeable headstages either for one 60, 120 or 256-electrodes' MEA or two 60-electrode MEAs per headstage, and a modified set for perforated MEAs is also available. It is in the MEA that the recording process starts. These consist of a glass substrate of 5x5 cm with electrodes embedded in it. The electrodes typically measure between 10 to 30 μm and are displayed in a square grid, with an interelectrode spacing of 30 to 700 μm. The cells, or tissue slices, are cultured directly on the MEA, which can have a plastic ring to serve as a culture chamber. The headstage also has three integrated stimulus generator units that allow for the application of monophasic or biphasic rectangular pulses, as single pulses, or

pulse trains. Additionally, the MEA electrodes can be individually selected for stimulation, which can either be in current or voltage mode. The headstage is connected to the interface board, which receives the electrophysiological signals. Here, there is a Digital Signal Processor (DSP), a component which can assume the detection and analysis of signals directly, instead of the standard interfacing with the data acquisition computer. This change offers the possibility for real-time signal detection, filtering, and analysis of the acquired data, alongside optional stimulation.

It is critical to note beforehand the right placement position for each type of MEA chip, considering that these are not rotationally symmetrical. For example, for 256 electrode 6-well' MEAs, the engraved serial number can be a useful marker. For its correct orientation, the MEA should be placed in a way that the serial number locates to the top left corner, when assuming a frontal view to the headstage opening side. Furthermore, the placed MEA should be pushed towards the bottom left corner in order to secure proper connection and readings.
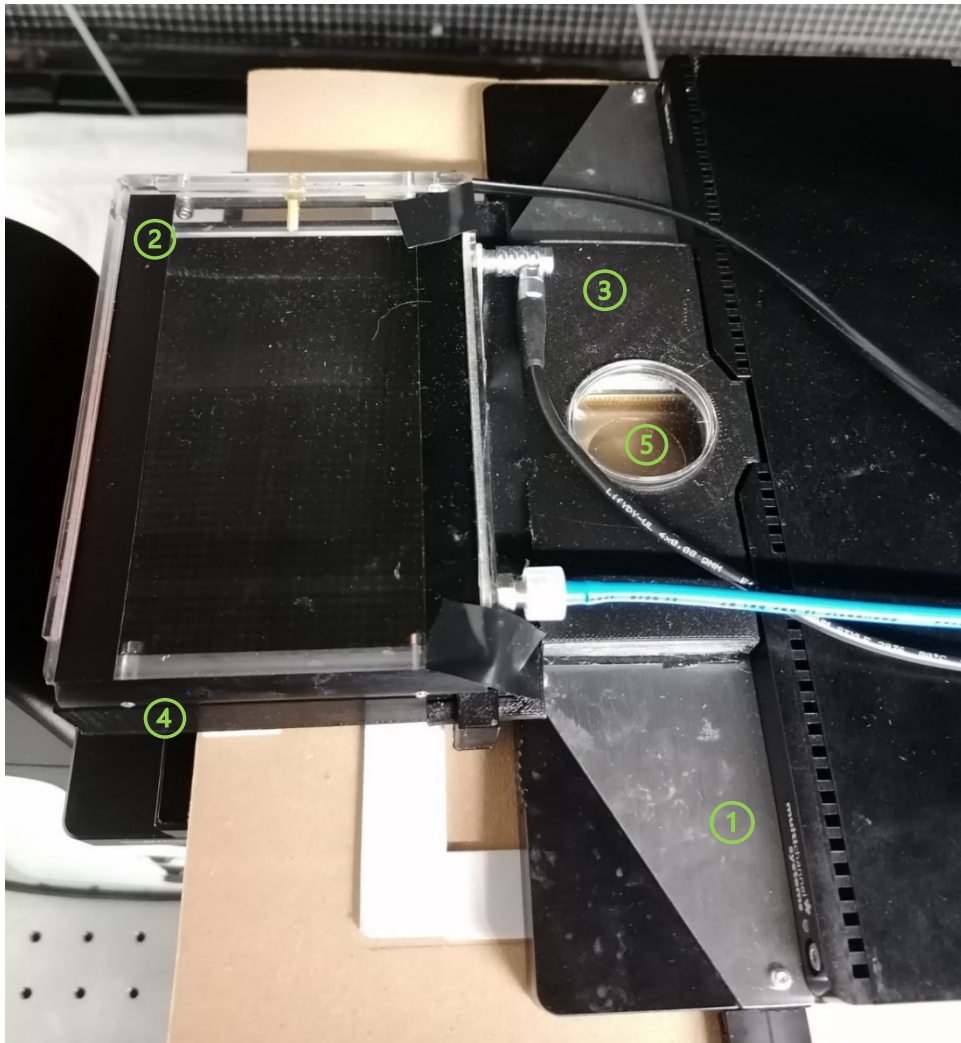

Figure 9 – The MEA2100 system headstage with an adapted stage top incubator for the maintenance of temperature and CO$_2$ concentration.
1) MEA2100 system headstage. 2) Ibidi stage top incubator lid. 3) 3D printed adapter for the proper connection between the incubating system and the MEA headstage. 4) 3D printed

support customized for the Ibidi lid. 5) Headstage plate where the MEA chip is housed, which allows for temperature control.

3.1.1 Data acquisition software

Additionally, it is fundamental to introduce the necessary software to interact and analyze the recording signals. The main interface to work with the MEA2100 system is the Multi-Channel Experimenter, which allows to monitor the data in "real-time" and modify the experimental protocol by changing, for example, the threshold for spike detection or the applied filter in the acquisition setup.

The graphical interface is very user-friendly and offers a simple functional principle for the experimental design. The necessary instruments can be dragged from the left side of the panel to the white panel and linked together (Figure 10). These instruments have color coded ports, which are displayed either on the upper or lower side, according to the input or output flow of data, respectively. The color code represents different data types that can only be connected together when matching, except for the grey recorder input, which accepts any kind of data input. Furthermore, each instrument has an independent control window tab which can be accessed with a double-click.
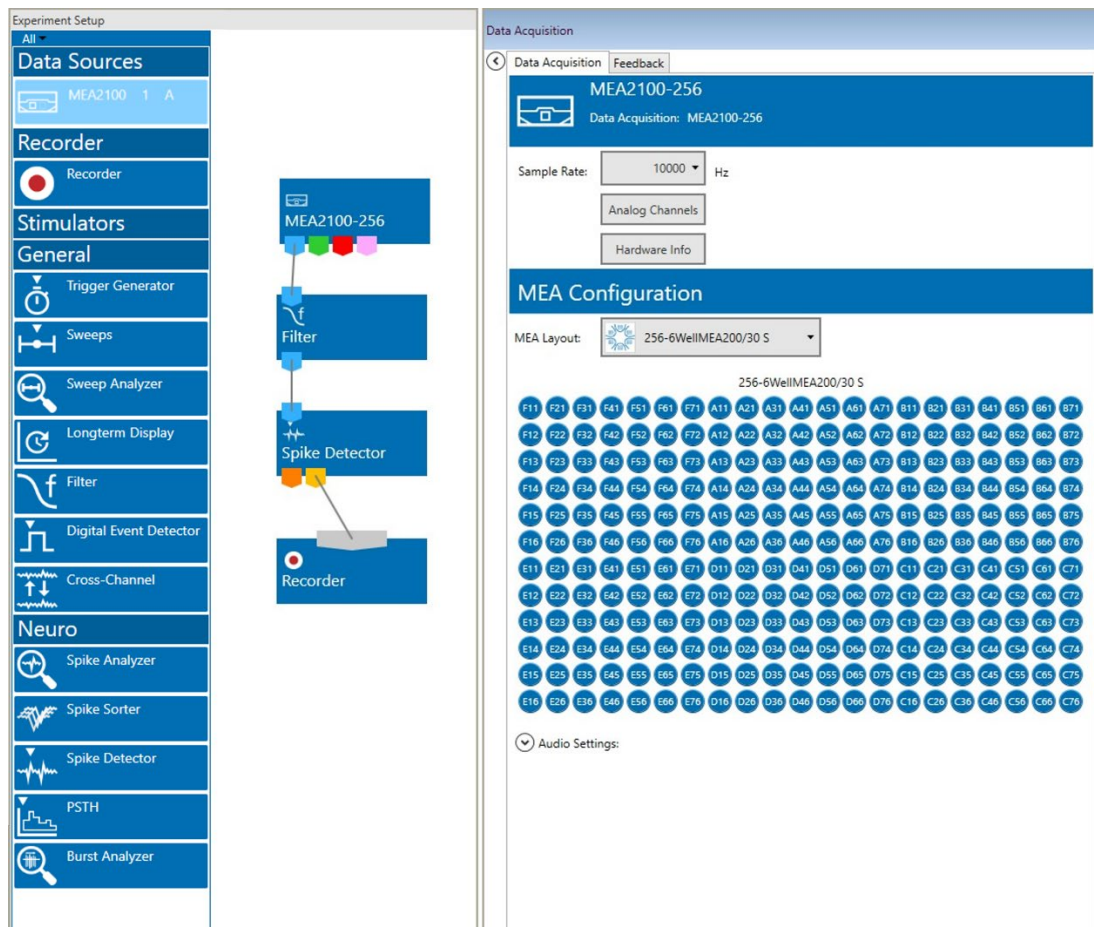

Figure 10 – Layout of MEA experimenter for the recording setup used in the work.

The same experimental design was systematically used throughout this project. It consisted of four distinct instruments, sequentially connected in the following order – MEA2100 (Data Sources), Filter (General), Spike Detector (Neuro) and Recorder (Recorder) (Figure 10). In the selected instruments there are, in total, 6 different color ports, excluding the grey recorder input. The MEA2100 has 4 possible data outputs: Blue, concerning electrode raw or filtered data, green for analog data, red for digital data and pink for trigger events. Regarding the spike detector, it has two output options: Orange, which concerns spike data, i.e., a fragment of data around the detected spike, and yellow, regarding just the time stamp of each spike. In this project, the connections were all blue to blue, except for the spike detector output, which was connected to the recorder through the yellow, or time stamp, port.

Once properly connected, some options had to be changed in the control window tab for each instrument. Starting with the MEA2100, the sample rate was set to 10 kHz if not the default value. Additionally, in the MEA configuration panel below, the MEA layout was changed for the 6-Well-S layout (Figure 10). Regarding the filter settings, there is the option to select the type of filtering method. In this case, the digital filter implemented was a second order high pass filter with a cut off frequency of 200 Hz, which does not interfere with the EAP frequency band (200 – 3500 Hz). In the spike detector control window, the selected detection method was always "Threshold", and both boxes for rising and falling edge were ticked and their values set to plus and minus 5 standard deviations. Detection by threshold means that, for each individual channel, the threshold is calculated by multiplying the chosen standard deviation by the noise. Once the "estimate" button is pressed, the threshold is calculated over the next 500 ms. One should always pay attention to the resulting threshold because, if there is spiking activity during the calculating duration, the threshold may be calculated with a wrong baseline (higher than it should be because of spikes) and, therefore, need to be calculated again. As for the recorder, it was used to change the file name and establish a timer for the desired recording duration.

Finally, there is another essential program in the Multi Channel Suite package, the Multi Channel DataManager. It allows for the conversion of the data files recorded with the Experimenter into other file extensions. Indeed, all data files recorded were converted to the HDF5 file extension, which makes it easier to import by MATLAB in order to perform data analysis.

3.1.2 Temperature control MEA2100-System and ibidi stage top incubator

Temperature is a critical factor to control during the experimental design. Variations in temperature are known to affect cell activity and viability, representing a particular frailty for this system, especially during longer recordings. Hence, an external

temperature controller (TC02) from Multi Channel Systems was connected to the MEA2100 system headstage, which has a heating element right below the MEA (Figure 9(5)). This element was set for 37°C, unless otherwise specified for specific purposes. The TC02 is equipped with PT100 sensors, providing the highest available accuracy for very precise temperature recordings. However, heating the MEA solely from below will lead to a vertical temperature gradient and condensation of cell medium. In order to solve this problem, an adapted external stage top incubator from ibidi was used (Figure 9(2)). The Heating and Incubation Systems (ibidi Stage Top Incubation System, ibidi GmbH) allow for an environment more similar to physiologic conditions by active humidity control as well as temperature and CO_2. Therefore, and unless specified otherwise, the glass lid is set to 42°C to prevent condensation, and CO_2 is sustained at 5%. Additionally, the ibidi Heating system has a type K thermocouple (TC-K, +/- 2.2°C) external temperature sensor, which was used to measure and help control the temperature in the medium inside the MEA. All these systems have computer softwares that allow for online control of all settings and data recording for monitoring long-term experiments.

3.2   Electrophysiology recordings

3.2.1 6wells MEAs

Throughout the present project we used MEAs with 256 electrodes, evenly split across 6 wells, which allow for six separate cultures in each MEA and each experiment repetition (Figure 5). 256-6wellMEAs are comprised of 252 recording electrodes, six for reference, which are located around each block, and four ground electrodes. The electrodes are made from TiN with a SiN isolator and embedded in a transparent glass substrate of 49 x 49 x 1 mm, delimited by a 10 mm high macrolon ring with six round chambers. Each well has 42 electrodes displayed in a 7 x 6 grid, granting 200 µm center-to-center distance between each 30 µm electrode. Such diameter results in an impedance of less than 100 $K\Omega$. Additionally, there is a double layer of contact pads around the rim of the MEA, which are made of transparent indium tin oxide (ITO) and provide contact to the signal amplifier.

3.2.2 Preparation of MEA for cell culture

3.2.2.1   Surface coating

For the preparation of MEAs for cell culturing, these must initially go through a process of surface coating. First of all, the MEAs undergo a step of plasma cleaning. Then,

these are incubated overnight at 37°C with 0.01 mg/ml poly-D-Lysine (PDL, Corning) diluted in sterile water, then washed at least 3 times with sterile water and left to completely dry under sterile conditions. Subsequently, the MEAs were incubated at 37°C with 5 µg/ml laminin isolated from mouse Engelbreth-Holm-Swarm sarcoma (Sigma-Aldrich Co.) diluted in Neurobasal medium, for at least 2h, before being removed in the moment immediately preceding cell seeding.

3.2.2.2 Cell culture

The hippocampal neuronal cultures were prepared by Dr. Miguel Aroso (NCN, i3S) and José Mateus (NCN, i3S). Experimental procedures involving animals were carried out following current Portuguese laws on animal care (DL113/2013) and the European Union Directive (2010/63/EU) on the protection of animals used for experimental and other scientific purposes. The experimental protocol (reference 0421/000/000/2017) was approved by the ethics committee of the Portuguese official authority on animal welfare and experimentation (Direção-Geral de Alimentação e Veterinária). All possible efforts were made to minimize the number of animals and their suffering.

The cell culturing experimental procedures were performed according to the following protocol:

Primary embryonic rat hippocampal neurons were isolated from Wistar rat embryos, which were removed from the pregnant rat at Embryonic Day 18 (E18).

The following tissues were dissected in 5 ml of Hank's Balanced Salt Solution (HBSS) (Cytiva HyClone™, Thermo Fischer Scientific), without Ca^{2+} and Mg^{2+}, which would inhibit the action of the Trypsin used in the following step. A trypsin solution is prepared by dissolving 7.5mg of Trypsin in 5 ml of HBSS and, at last, sterilized by filtering with a 0.22 µm filter. 2.3 ml of the trypsin solution were then added to the HBSS containing the hippocampal tissue for enzymatic digestion and incubated for 15 min at 37°C, except for a brief agitation every 5 minutes.

Subsequently, the supernatant was discarded, and the tissue fragments were washed once with 5 ml of a trypsin inactivation solution composed of 10% (v/v) heat-inactivated fetal bovine serum (hiFBS) (biowest, LabClinics) in HBSS, and twice with HBSS to remove hiFBS from the solution. Finally, the supernatant was once again discarded and replaced with 5 ml of a Supplemented Neurobasal medium (Gibco, ThermoFischer Scientific), containing 2% (v/v) B27 (supplement to support growth and viability of hippocampal and other CNS neurons), 0.5 mM glutamine, 1% (v/v) penicillin/streptomycin (P/S, 10,000 units /ml penicillin and 10,000 µg/ml streptomycin) (Gibco, ThermoFischer Scientific), and 1% (v/v) amphotericin B (Cytiva HyClone™, Fisher Scientific).

At this point, the tissue was further dissociated with the mechanical aid of a 5 ml plastic pipette and, sequentially, the suspension was filtered with a 40 µm nylon strainer

(Falcon, Enzifarma), to exclude remaining tissue clumps. Then, 10 µl of the cell suspension are mixed with 10 µl of HBSS and 10 µl of trypan blue (0.4% (w/v)) (Sigma-Aldrich Co.) to prepare for the counting of viable cells. The trypan blue exclusion assay allows for the identification of viable cells because only cells with compromised membranes are permeated by the dye. Accordingly, $5x10^4$ viable cells suspended in 200 µl of the Supplemented Neurobasal medium were seeded in each well of the previously coated 6-well MEA. Independently of the experiment recording protocol, during the intervening period, the cultures were always kept in a humidified incubator at 37˚C, supplied with 5% CO_2 and subjected to medium replacement every 2/3 days.

3.2.3 Temperature Experiments

3.2.3.1   System temperature calibration

Headstage plate temperature was incremented by 1˚C every 20 minutes, starting at 37˚C and finishing at 45˚C. Throughout the whole time, the temperature in the medium inside a random well of the 6 well MEA was measured with an external temperature sensor, TC-K, connected to the ibidi Heating System. To start with the 1˚C increment in the headstage plate temperature, the recording temperature in the medium was first left to stabilize at the initial 37˚C. The temperature data of both the headstage plate temperature and the temperature measured inside the medium were monitored every 10 seconds with the softwares associated with both the TC02 from Multi Channel Systems and the ibidi heating system, and later used for the system calibration.

3.2.3.2   Temperature impact on neuronal electrophysiology.

Recordings were conducted with cells at DIV18. The headstage plate temperatures were set to 42˚C and 45˚C in order to replicate physiological (37˚C) and hyperthermic (42˚C) conditions in the medium throughout the whole recordings. The temperature inside the medium was left to stabilize before recording neuronal activity in each condition.

Additionally, we observed that the TC-K sensor was evoking an intercalating biphasic noise signal. Therefore, the temperature in the medium was only measured until the recording started and right after it finished. Electrophysiology was recorded for 1 hour in each condition.

3.2.3.3   Selective Inhibition of TRPV4 activity.

Electrophysiology experiments of the effect of RN1734 (TRPV4 inhibitor) were conducted after the recordings described above. However, to restore the initial conditions, the headstage plate was left to cool down and, meanwhile, the MEA was kept in the incubator. Then, RN1734 was added to the medium and the MEA was put back in the system to stabilize at 37ºC in the medium. Subsequently, the experimental design was as described in section 3.2.1.3.

The antagonist RN1734 was obtained from Sigma-Aldrich Co. for the selective inhibition of TRPV4 activity. A stock solution of RN1734 (10 mM) was initially prepared in DMSO. For any experiment, an aliquot of the stock solution was first diluted in HBSS (1:10) and, subsequently, 4 µl of this solution were added to the medium (400 µl), in order to get the desired concentration of RN1734 (10 µM) and also, ascertain that the final concentration of DMSO in the medium during the electrophysiological recordings was 0.1% or less.

3.2.3.4   Activity Metrics

Excluding the synchrony measure, which is directly given for the whole well, the first step was to calculate the mean of each metric for every active electrode and, subsequently, the mean for each well. Then, for each of the following activity metrics, the values for the physiological condition (37°C without RN1734) were considered as 100% and the values for the other conditions were calculated as a percentage of those values ((parameter at condition/parameter at baseline (37°C without RN1734))*100) for each well. Finally, the mean of the percentage variation for each condition was calculated from all considered wells, or cultures (N = 19 for hyperthermia experiments without RN1734, N = 14 for hyperthermia experiments with RN1734 and N = 5 for TRPV4 temperature activation experiment with RN1734). Outliers were removed with the MATLAB function 'rmoutliers', where an outlier can be defined as a value more than 1.5 interquartile ranges above the upper quartile or below the lower quartile of the data.

Regarding the definition of each metric, some important remarks should be considered. Active electrodes were selected as those which had a minimum firing frequency of 0.1 Hz. The firing rate, in Hz, is calculated by dividing the number of detected spikes by the duration time of the recordings, in seconds. The burst rate is calculated in a similar manner, only considering the number of bursts instead of the number of spikes. A burst was defined as a group of spikes with at least two consecutive spikes with a maximum time delay of 10ms between such spikes detected in the same electrode. Interburst interval reveals the period between the end of a burst event and the beginning of the next one. Finally, the synchrony measure uncovers the level of synchrony of the neuronal network according to temporal fluctuations of a global variable, such as instantaneous spike activity,

as it is the case in this project. Therefore, in a synchronous state there are observable, well-defined global variations whereas, in an asynchronous state, the variance of such variable decreases/approaches a time-independent limit as the population grows. The variance, σ^2, of a random variable V is calculated as the squared deviation of its averaging, at a given time, t:

$$\sigma_V^2 = \langle [V(t)]^2 \rangle_t - [\langle V(t) \rangle_t]^2 \qquad\qquad 20$$

Furthermore, the synchrony quantification, *X*, can be normalized by the average fluctuations of such variable for each culture, in order to return a value between 0 and 1, corresponding to a totally asynchronized spiking behavior and a state of full synchrony, respectively:

$$X^2(N) = \frac{\sigma_V^2}{\frac{1}{N}\sum_{i=1}^{N}\sigma_{V_i}^2} \qquad\qquad 21$$

The representation of the evolution for each metric between conditions was represented as a spider plot adapted from the following - Moses (2021). spider_plot (https://github.com/NewGuy012/spider_plot), GitHub. Retrieved September 15, 2021.

3.2.4 Statistical analysis

Statistical analyses were performed on MATLAB using the Paired Sample t-Test, which allows to identify statistical differences between measurements taken from the same population at two different conditions. Differences between groups were considered statistically significant when $p < 0.05$.

3.2.5 Activity patterns in long duration recordings

The experiments for long-term dynamics of neuronal networks were conducted with cells at DIV 7 and 14. After placing the MEA in the system, as in common practice, the cells were left to stabilize its activity before starting the recordings. For these experiments, the temperature in the headstage plate was kept at 37°C. Additional recording settings were kept as described in section 3.1.1.

Chapter 4

Results and Discussion

4.1 Cell medium temperature calibration during electrophysiological recordings

In order to properly access the impact of temperature in the electrophysiological activity of cultured hippocampal rat neurons, it is first necessary to verify if the cell cultured MEA is correctly maintained at physiological temperatures throughout the recording duration and, ultimately, if hyperthermic conditions (39°C) can be kept in a controlled, replicable manner.

Thus, the starting point was to record the real temperature in the cell medium inside the MEA during a typical protocol. MEAs are kept in an incubator, at 37°C, during the intervening period and immediately put in the headstage of the MEA2100 system when taken out to start each experiment. The desired temperature is controlled by two different elements in our electrophysiological apparatus, one connected to the headstage and an adapted external stage top incubator. Typically, the headstage is set to 37°C and the stage top incubator to 42°C in order to prevent a vertical temperature gradient and, consequently, condensation.

The temperature in the medium was then monitored with a TC-K sensor and left to stabilize at the desired physiological temperature. However, such conditions were not attained as the temperature tended to stabilize at around 33,6/34°C after a reasonable amount of time (30 minutes). Furthermore, we sought to understand what temperature would be recorded in the medium inside the MEA when inducing an hyperthermic state. The headstage heating plate was set to 40°C and, after a similar stabilizing interval, the temperature was observed to tightly fluctuate around 35,5°C.

At this point, it was fundamental to validate the accuracy of the TC-K temperature sensor and verify the accordance between the temperature set to the headstage plate and the real temperature at its MEA-contacting surface.

Therefore, a convenient way to test the TC-K sensor at physiological temperature was to use a calibrated incubator. The sensor was placed inside the closed incubator at 37°C and left recording for an hour (Figure 11). As it can be seen, the temperature seems to oscillate around 36.7°C, which, although not parallel with the input, is clearly closer to that value (< 0.5°C) than it was in the experiment above (> 3°C), meaning that the accuracy of sensor is not significantly compromised. Additionally, it should be noted that this thermosensor has an associated error of ±2.2°C which, although substantial, does not explain the difference between the temperature set in the headstage plate and the one measured in the medium inside the MEA.
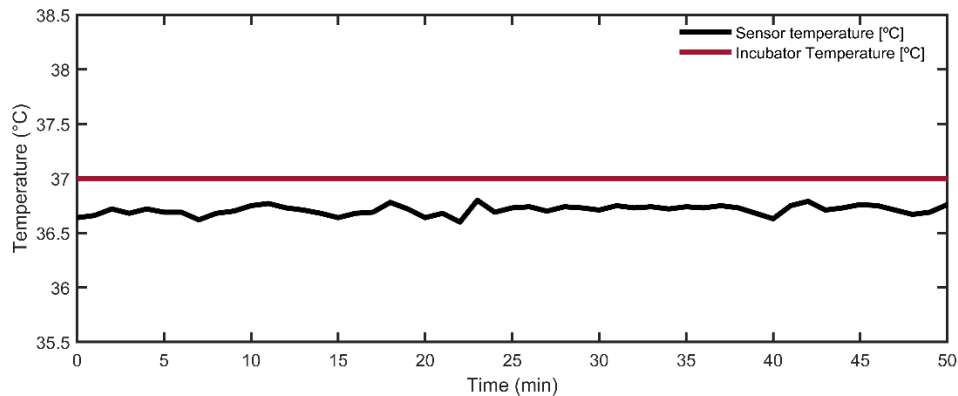

Figure 11 – Comparison between the incubator temperature and the temperature registered in the sensor.

Subsequently, it was logical to verify that the headstage heating plate was working correctly. Thus, the thermo sensor was attached to the MEA-contacting surface of the headstage and the recorded temperature was tested according to the input. It is important to mention that the solid-on-solid interface between the sensor and the plate lacks appropriate heat insulation and, therefore, the recorded temperature will, inevitably, be slightly lower than the input (Figure 12).
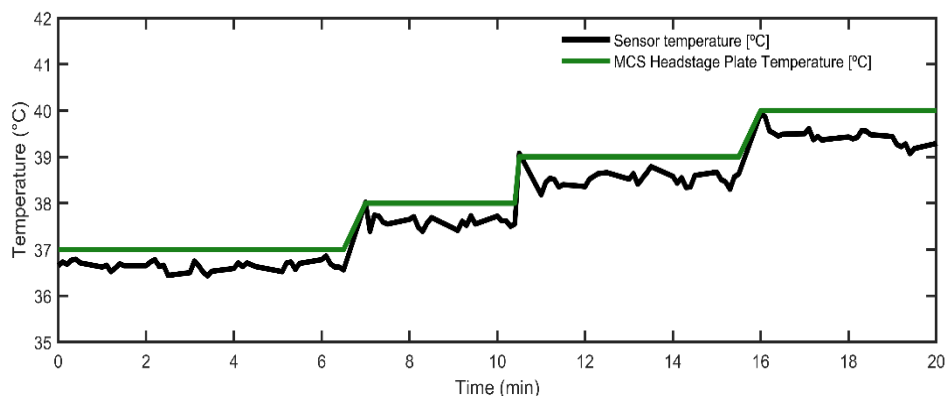

Figure 12 – Comparison of the temperature set in the MEA recording system and the temperature recorded by the sensor while in contact with the heating plate.

As shown in Figure 12, the temperature measured with the sensor is loosely similar to the input and accurately follows the 1°C increasing steps, meaning that the heating plate of the headstage is working properly.

Considering the previous results, how the sensor and the heating systems are apparently working properly, one can assume that the incompatibility between the desired and the recorded temperature may be due to insufficient insulation and heat dissipation. Thus, it was then necessary to establish a correlation between the temperature imposed by the system and the "real" recorded temperature in the medium inside the MEA, as well as to understand the time scale necessary for such condition to stabilize or, at least, vary insignificantly for the experiment duration.

Thus, the following experimental design consists of continuously recording the temperature in the medium inside the MEA, while incrementing 1°C in the headstage plate every 20 minutes, from 37°C to 45°C (Figure 13(A)).

Before each repetition of the experiment, the MEA was taken from the incubator, immediately put on the MEA2100 system, and left for 30 minutes to stabilize thermically. The starting recorded temperature was quite homogenous throughout repetitions: 33.76°C (±0.09°C). It should be noted that longer stabilizing intervals could indeed lead to an increase in the temperature reached, although slow and therefore impractical for typical experimental designs, which frequently last for periods shorter than 20 minutes[16].

A tendency for an increase of discrepancy between the temperature recorded by the sensor and the temperature set in the heating plate can be noted throughout stages. This difference was determined for the last value measured in the medium before the increase in temperature at the headstage plate. In average, for each 1°C increase, the recorded temperature would only increase 0.68°C ± 0.09°C. Such tendency highlights the relevance in understanding what mathematical model better fits the data as a predictor for future experimental designs (Figure 13(B)). A linear regression seems to perfectly fit the data, returning a high R^2 value, which represents smaller differences between the observed data and the fitted values, and more precise predictions. Attending to the proposed experiments, the fitting equation can now be used to know at what temperature the plate should be to attain both 37°C and 39°C at the cell medium inside the MEA. Respectively, the returned values are approximately 41.7°C and 44.7°C.
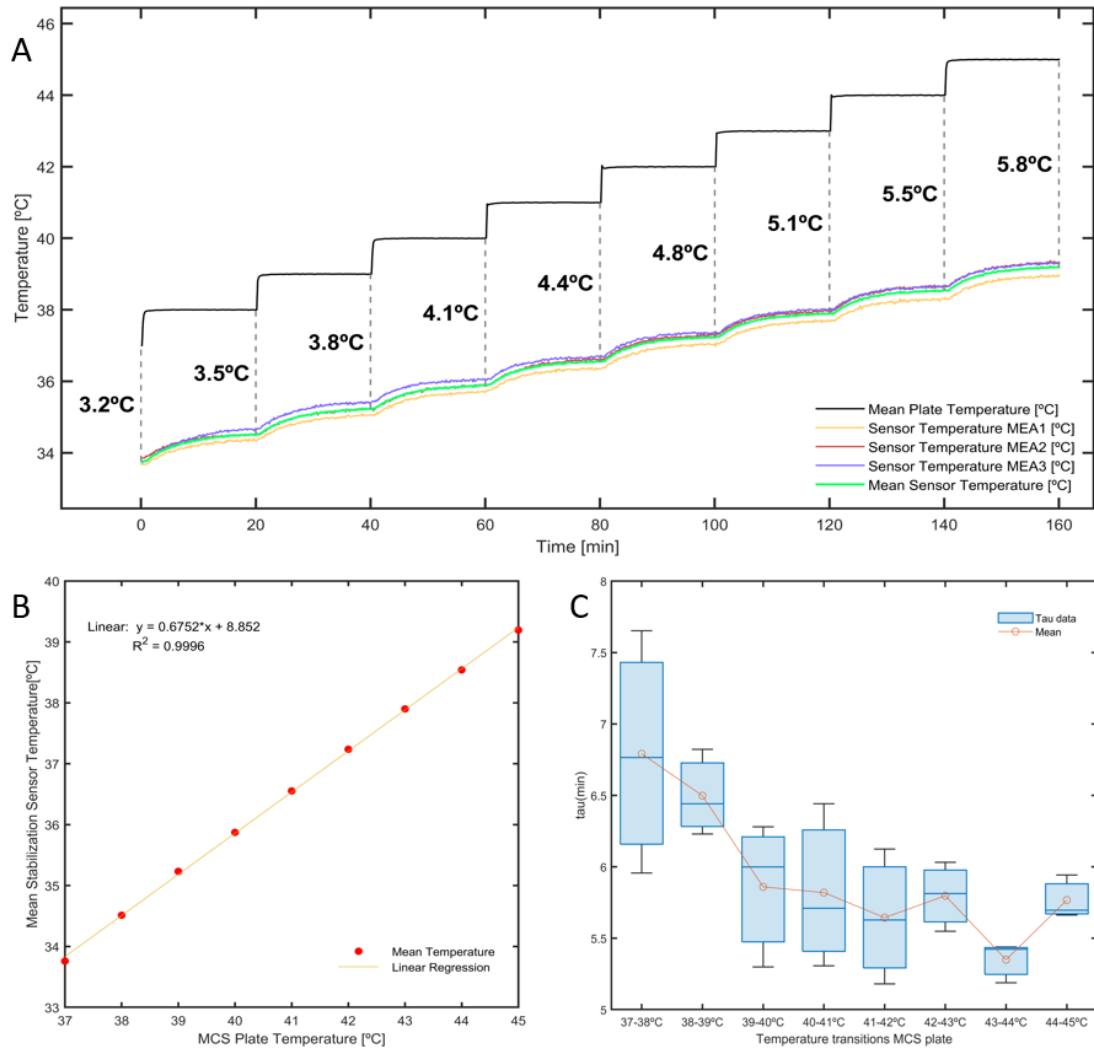
Figure 13 – **Calibration of temperature control in the MEA system.**
A) Comparison between the temperature set in the headstage plate and the "real" temperature recorded in the medium inside the MEA for 1°C incrementing steps every 20 minutes. The temperature at the left of each dotted line corresponds to the difference between the headstage temperature and the mean temperature in the sensor (mean of all repetitions) immediately before increasing temperature. B) Linear regression of the relation between the temperature at the plate and the temperature reached in the medium. C) Representation of the tau value for each temperature transition.

Right after each 1°C increment in the system (Figure 13(A)), one can observe that the recorded temperature repeatedly presents a faster increase in the first minutes and then tends to assume a slower increasing pace while seemingly reaching a stabilizing plateau. This profile, which can be observed for each temperature transition (Figure 14), fits the following exponential equation:

$$y = a * \left(1 - e^{(-x/tau)}\right) + c;$$

The tau value is defined as the time interval necessary for the temperature to reach 2/3 of its maximum value, i.e. the stabilizing temperature. Thus, for each 20-minute time interval of temperature transition in each repetition, the tau value was extracted and shown in Figure 13(C). During the first two temperature transitions, the tau value is observably higher than for the remaining transitions, which display more similar values.

However, this difference is not considerably significant since all values are almost contained in a 1-minute interval. Therefore, we recommend a 10-minute interval (slightly above the maximum tau observed) between the setting of a new temperature and the beginning of the recording.
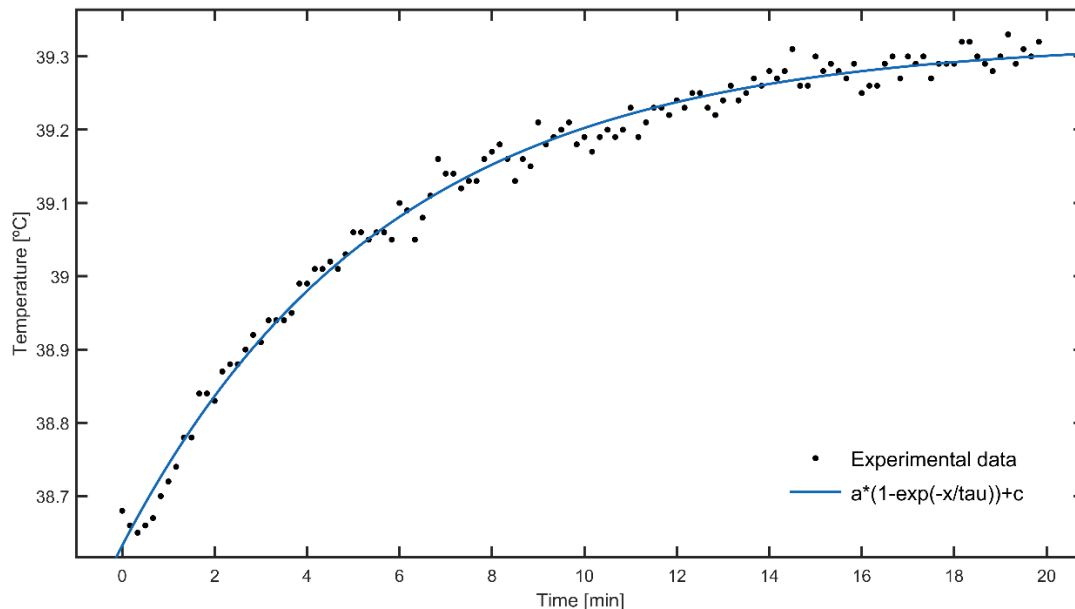

Figure 14 – Exponential fit to a representative temperature increase in the cell medium over 20 minutes.
The chosen profile represents the increase in temperature in the cell medium for the transition between 44°C and 45°C.

4.2   Impact of hyperthermia on neuronal activity

Once understood the correlation between the temperature set at the MEA2100 system and the temperature measured at the cell medium inside the MEA, our aim was to observe the impact of hyperthermic conditions in the electrophysiology of cultured hippocampal rat neurons.

Thus, the established experimental design consisted of consecutive recordings of electrophysiology at physiological temperature (baseline) and the hyperthermic state, 39°C, for 1-hour periods. To achieve these temperatures at the cell medium inside the MEA, the temperatures in the system was respectively set to 42°C and 45°C. Prior to each recording moment, either at the start of the experiment or during the heating phase, the culture was first left to reach the desired temperature.

The effect of heating in electrophysiology was accessed through the computation of a variety of activity characterizing metrics.

Figure 15 depicts a representative profile of the heating effect in the MFR recorded at each electrode for all the wells in a MEA (Figure S1-Figure S3 for other MEAs). For every well, the number of electrodes considered corresponds to the total of active electrodes in either one or both conditions, even if below the established minimal firing rate threshold,

0.1Hz, for one of the temperatures. In general, the MFR of each population decreases by approximately half of its initial value. This tendency can be clearly followed at each electrode level and, even though plenty electrodes display comparably reduced firing rates, these would, almost invariably, decrease further at 39°C, even to the point of no recordable activity. These results suit the scarce literature regarding the impact of temperature increase in hippocampal neurons, where a decrease of neuronal activity was shown by optogenetics, but not electrophysiology[12]. Recently, Zwartsen et al. studied the impact of heating in the electrophysiology of rat primary cortical cultures in vitro. Similarly to our results, here they showed a depression in the MFR of the cultures by approximately 25% both during acute exposure (30 min) to increased temperature as wells as after a prolonged period of exposure (4.5 h)[89]. However, it is necessary to retain that the temperature mentioned as hyperthermic was 41°C.
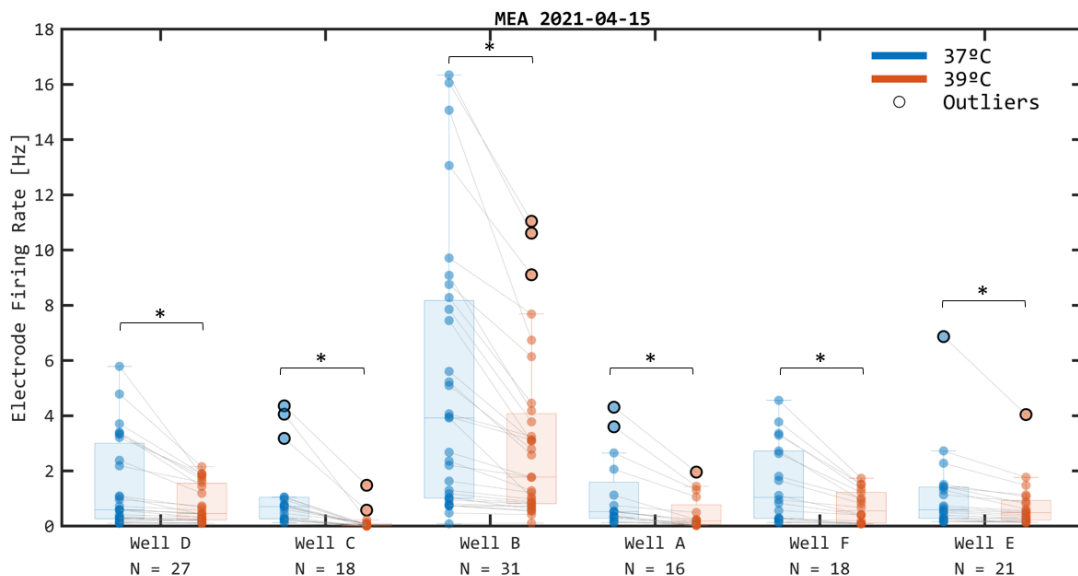

Figure 15 – The effect of hyperthermic conditions (39°C) in the MFR for all wells of an MEA (15-04-2021).
All electrodes active for one or both conditions were considered. * Indicates a temperature-induced significant difference (p < 0.05).

Furthermore, we explored the effect of an hyperthermic state in other characterizing metrics of neuronal activity. Figure 16 shows the distinctive variation profiles for each metric in the 6 populations of a 6-well MEA (Figure S4-Figure S6 for other MEAs). The evolution is displayed as the percentage variation from each parameter at 39°C to the parameter at baseline, 37°C, which is normalized as 100%.

Firstly, one can notice that the number of active electrodes is either maintained or decreases throughout conditions. As seen in Figure 16, the firing rate considerably decreases to values between 25% and 50% lower than those at the baseline condition, and this tendency is tightly followed by the bursting rate. This fact elucidates a trait in the variation profile as, even though there is a decrease in overall activity, the firing rate and burst rate are kept at a similar ratio. Only in well C do both metrics decrease more than

usual, but it should also be noticed that the number of active electrodes in this well is considerably lower, which insinuates an overall activity depression in this culture.
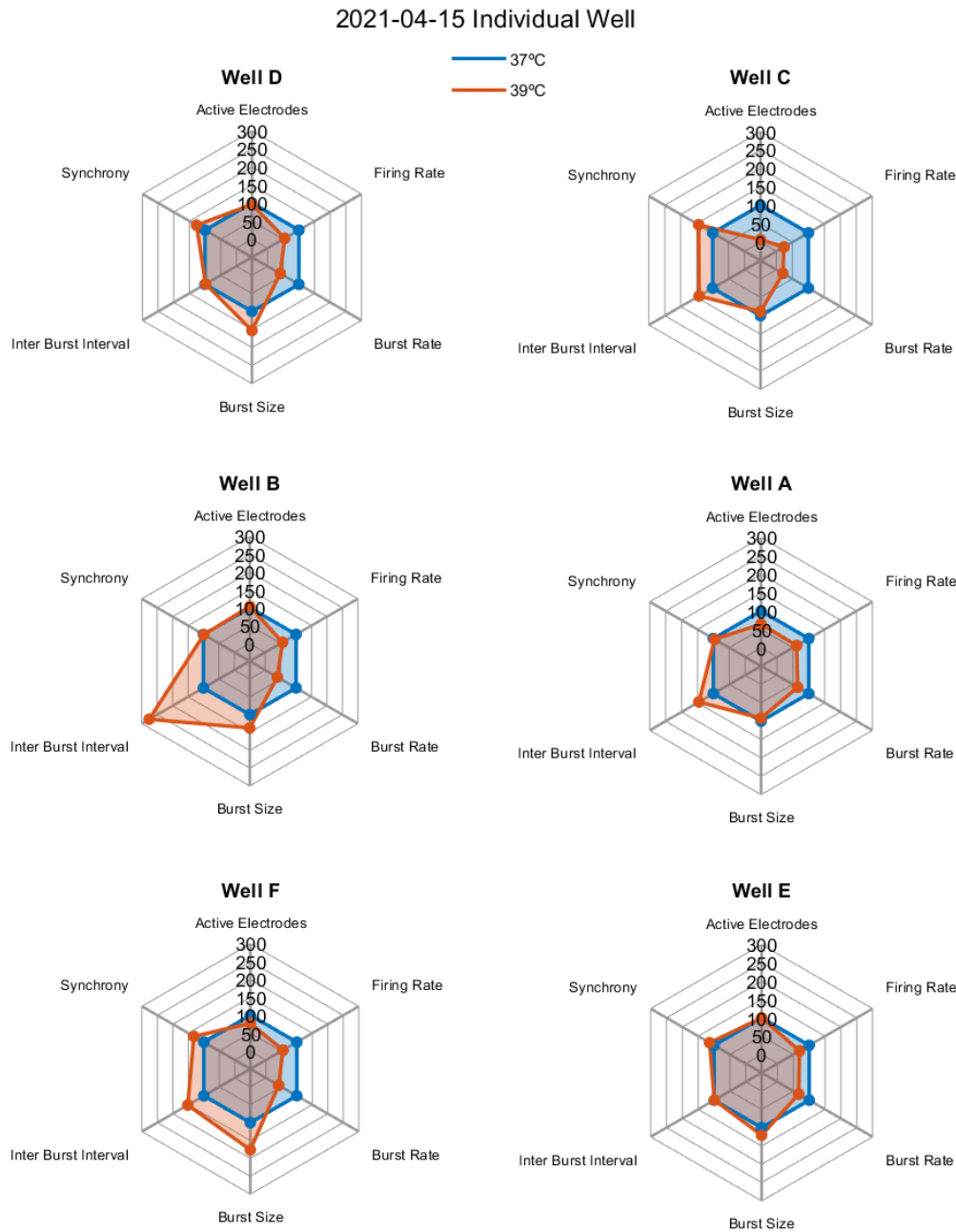

Figure 16 – Effect of an increase in temperature (39˚C) on a set of activity-characterizing metrics for each well in an MEA (15-04-2021).
The evolution is displayed as the percentage variation from each parameter at 39˚C to the parameter at baseline, 37˚C, which is normalized as 100%.

Regarding the bursting activity itself, we proceeded to the observation of both the size of each bursting event and the interburst interval, which are two relevant traits of the information conveyed in the electrical activity of neurons. In three cultures (well C, A and E), burst sizes are loosely similar between conditions, however in well D, B and F, there is an increase of at least 50%. Concerning interburst intervals, there is no apparent pattern in its variation throughout conditions. It can be maintained at slightly similar values as in well

D and E or increase considerably. In well B there is an exaggerated rise in the values of interburst interval, which may be explained by the temporal disposition of the activity. At 37°C, the bursting activity may have been condensed in a continuous interval, or present throughout the whole recording. In contrast, 39°C may have been characterized by several, substantially distant, discrete periods of activity that may have influenced an increase in the mean of all interburst interval values for that well. Finally, the synchronicity of the cultures either registered an increase of up to 50% or maintained the baseline value.

At this point, to properly evaluate the impact of hyperthermic conditions on the electrophysiology of dissociated rat hippocampal neurons, the mean of the data regarding each metric of each culture (well) for both conditions were gathered and, once again, compared as the percentage of variation between the baseline (37°C) and 39°C. This data corresponds to a total of 19 individual wells across 4 different MEAs and is displayed in Figure 17, as the mean of the variation percentage in all cultures, with the color filled area representing the respective standard deviation.
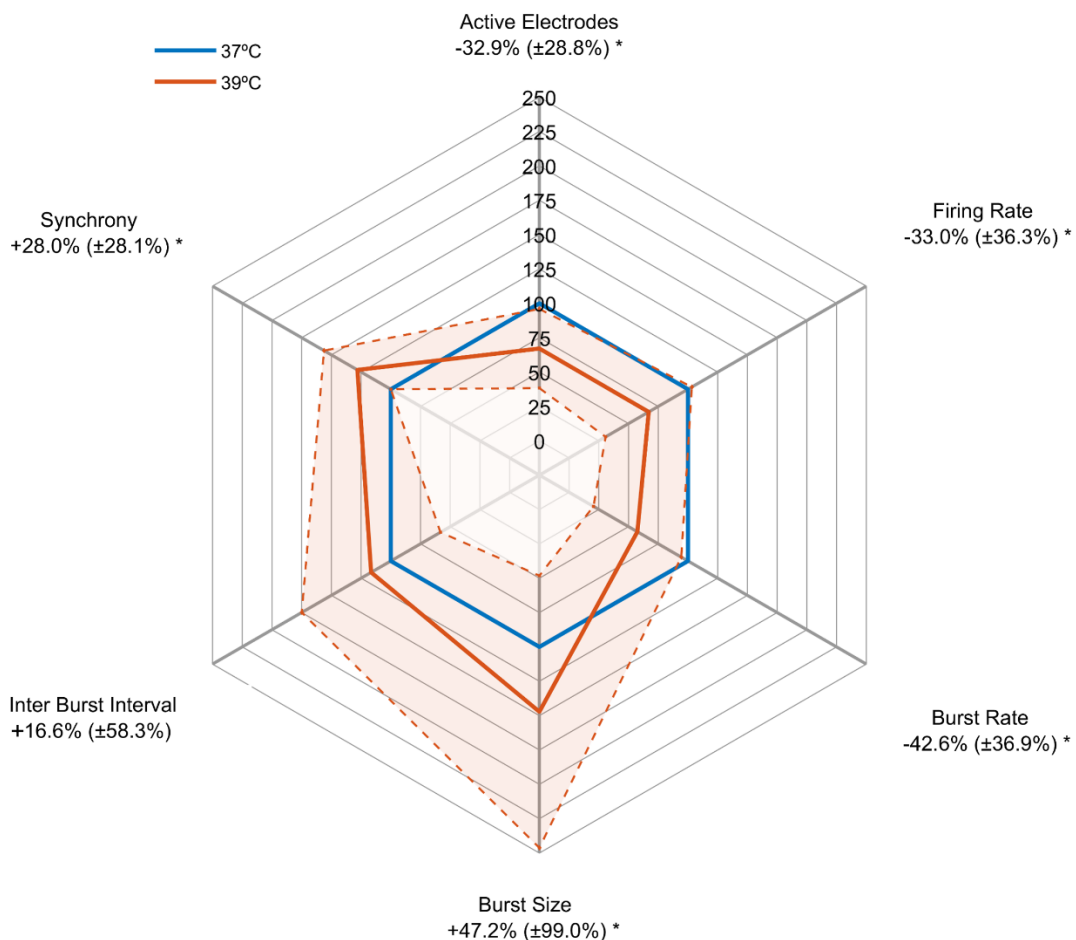

Figure 17 – The effect of an hyperthermic condition (39°C) on neuronal activity.
The data from each repetition was joined together as the mean value for each metric. The effect of heating is displayed as the percentage variation from each parameter at 39°C to the parameter at baseline, 37°C, which is normalized as 100%. The value of these percentages and respective SD is shown below each metric. The color filled area represents the respective standard deviation. * Indicates a temperature-induced significant difference (p < 0.05).

In general, with the increase in temperature, there was a discernable tendency for the number of active electrodes to decrease (-32.9% ± 28.1%), possibly reflecting the overall reduction of the activity due to heating, as stated in literature[12]. It should be kept in mind that only electrodes with activity superior to a 0,1 Hz threshold are considered. Our results show a significant decrease of the firing rate by 33% (±36.3%), which is in accordance with Zwartsen et al., where the firing rate was reduced by approximately 25% both during a period of acute exposure and after a prolonged exposure, as stated before.

Additionally, in our results, the only other metric that suffers a considerable reduction is the burst rate. The 42.6% (±36.9%) difference is in accordance with the overall reduction of activity in the cultures but shows a larger reduction than that described in literature. The effect of an acute exposure to 41°C was sensibly half the percentage registered by us and, after a prolonged exposure the difference was considerably higher, as they only measured a 5% difference between the baseline condition and 41°C.

The burst size represented the biggest increase in the metrics we calculated - 47.2% (±99.0%) – however, the value of the standard deviation is remarkably broad, and it should be noted that the burst size can, with a considerable probability, be lower than that of the baseline. There are no corresponding studies in literature but, Zwartsen et al. did measure the variation of a similar metric, the burst duration (average time between the first and last spike inside a burst, in seconds). Interestingly, in their experiments, the burst duration always decreased with the increase in temperature. Additionally, in our results, the mean interburst interval value increased 16.6% but also presents a wide standard deviation, ±58.3%, which encompasses values below the baseline. Zwartsen et al. registered an increase in the interburst interval superior to our results, but then again, these values are contained in the wide range of the standard deviation. Finally, we describe an overall increase in the synchronization of the network by 28.0% (±28.1%).

In sum, when comparing the electrical activity of primary hippocampal neuronal networks at a physiological temperature (37°C) and hyperthermia (39°C), we could observe an overall reduction of activity due to heating.

4.3 Molecular mechanisms of temperature's effect on neuronal activity – Inhibition of TRPV4 by RN1734

The molecular mechanisms by which hyperthermia alters normal neuronal activity are still scarcely understood. This effect is believed to have multiple pathways, but one plausible mechanism to participate in such impact revolves around the action of ion channels of the TRP family. TRPV4 is expressed in hippocampal neuronal populations, where it has been described to have a temperature activation threshold of around 34°C[34,35]. By employing whole-cell patch clamp, it was found to be involved in neural excitability through the modulation of the resting membrane potential. The normal resting membrane potential,

when compared with the application of ruthenium red, a pan-TRP inhibitor, or TRPV4KO cells, was considerably more depolarized and therefore more prone to elicit spiking events. Furthermore, the same effect was later confirmed in hippocampal granule cells of slice preparations, and a reduction of activity in EEG was also observed in TRPV4KO mice[40]. Consequently, we sought to explore the influence of TRPV4 as a transducing agent of heating into the dynamics of extracellular electrophysiology in *in vitro* dissociated rat hippocampal cultures.

To verify the possible action of TRPV4 in the reduction of neuronal activity due to heating, we used a specific antagonist - RN1734 (10 μM). After the proceedings described before, there was an initial cooling step where the temperature in the headstage plate was set to 42°C and the temperature in the medium inside the MEA was left to stabilize once again at 37°C. Then, the inhibitor was added to the cultures and the activity was recorded as already described.

The activity profiles of the 3 different conditions - 39°C, 37°C + RN1734 and 39°C + RN1734 – are also shown, in Figure 18, as the percentage of variations relative to the baseline condition of 37°C and the respective standard deviations. For this analysis, we considered a total of 14 wells distributed across 4 MEAs. Firstly, the variations observed at 39°C were clearly consistent with the results mentioned above, presenting only a substantially wider range of values for the interburst interval. However, the presence of RN1734 lead to an almost complete cessation of activity at both temperatures tested: at 37°C the firing rate got close to a 70% reduction (± 22.9%) and close to 80% (± 12.9%) at 39°C.

Following the same tendency of the firing rate, the burst rate suffered a decrease of about 90% at 37°C + RN1734 and almost complete at 39°C + RN1734, where only one bursting event was registered throughout all wells. This fact justifies the inexistence of standard deviation values in the burst size scale for this condition, as well as the interburst interval value, which is, understandably, 0. At 37°C + RN1734, the interburst interval took a disproportionately large increase due to the spacing between the scarce bursting events, which saw a considerable diminution in its rate. However, the burst size was kept similar to the baseline condition(90,4% ± 42.5%). Finally, at 37°C + RN1734, the synchronization of the network had an increase of 43.4% (± 88.3%), although with a wide range of standard deviation, while at 39°C + RN1734, the increase was considerable accentuated (240.7% ± 123.8%).

In sum, the inhibition of TRPV4 led to a large diminution of activity, which is more pronounced with heating. Therefore, the normal functioning of TRPV4 is not the main reason for the activity reduction registered when increasing temperature.
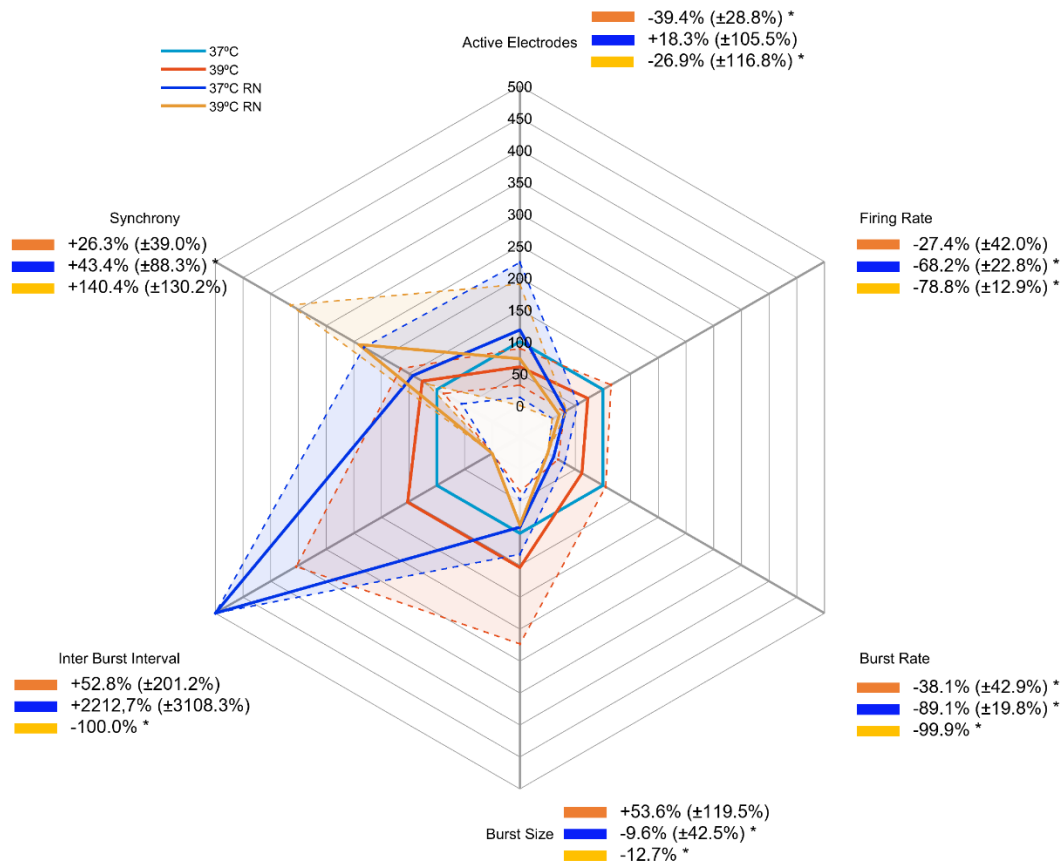
Figure 18 – Comparison of the activity profiles between baseline (37˚C) and three different conditions: 39˚C, 37˚C + RN1734, 39˚C + RN1734.
The data from each repetition was joined together as the mean value for each metric. The effect of heating is displayed as the percentage variation from each parameter at one of the three conditions (39˚C, 37˚C + RN1734, 39˚C + RN1734) to the parameter at baseline, 37˚C, which is normalized as 100%. The value of these percentages and SD is shown below, or at the side of each metric, accompanied by the color representing each condition. In the 39˚C + RN1734, burst related metrics have no SD, this is due to fact that there was only one burst event across all cultures. The color filled area in the graph represents the respective SD. * Indicates a temperature-induced significant difference (p < 0.05).

As described in literature, the activation temperature for TRPV4 in hippocampal neuronal cells is close to 34˚C and therefore, the application of RN1734 in a culture at a temperature lower than that would ideally have no discernable effect[35]. Thus, we conducted a smaller experiment where the temperature in the headstage plate of the electrophysiology system was set to 35˚C in order to record the activity at 32˚C in the medium inside each well of the MEA. The MEA was left to stabilize at the desired temperature and its activity recorded for one hour before adding RN1734 and record another hour.

Figure 19 depicts the profile of the percentage of variation and respective standard deviation. In sum, there is a considerable decrease in the number of active electrodes and an even more accentuated reduction in the firing rate and burst rate. Burst size and synchrony are loosely similar to the baseline condition but the interburst interval shows a large increase, which is expected due to the diminution of the burst rate.

Considering the selectivity of RN1734 towards TRPV4 and the application of the concentration standardized across literature (10 µM), one would not expect such a reduction of neuronal activity. Thus, we are left questioning the reference activation temperature for TRPV4 and the possibility for it to be lower than assumed. For hippocampal neurons, as observed by Shibasaki et al through Ca^{2+} fluorescence imaging, heat-evoked increase in cytosolic Ca^{2+} caused by TRPV4 was seen at 33.7°C but not at the inferior temperature step shown (30.3°C)[35].
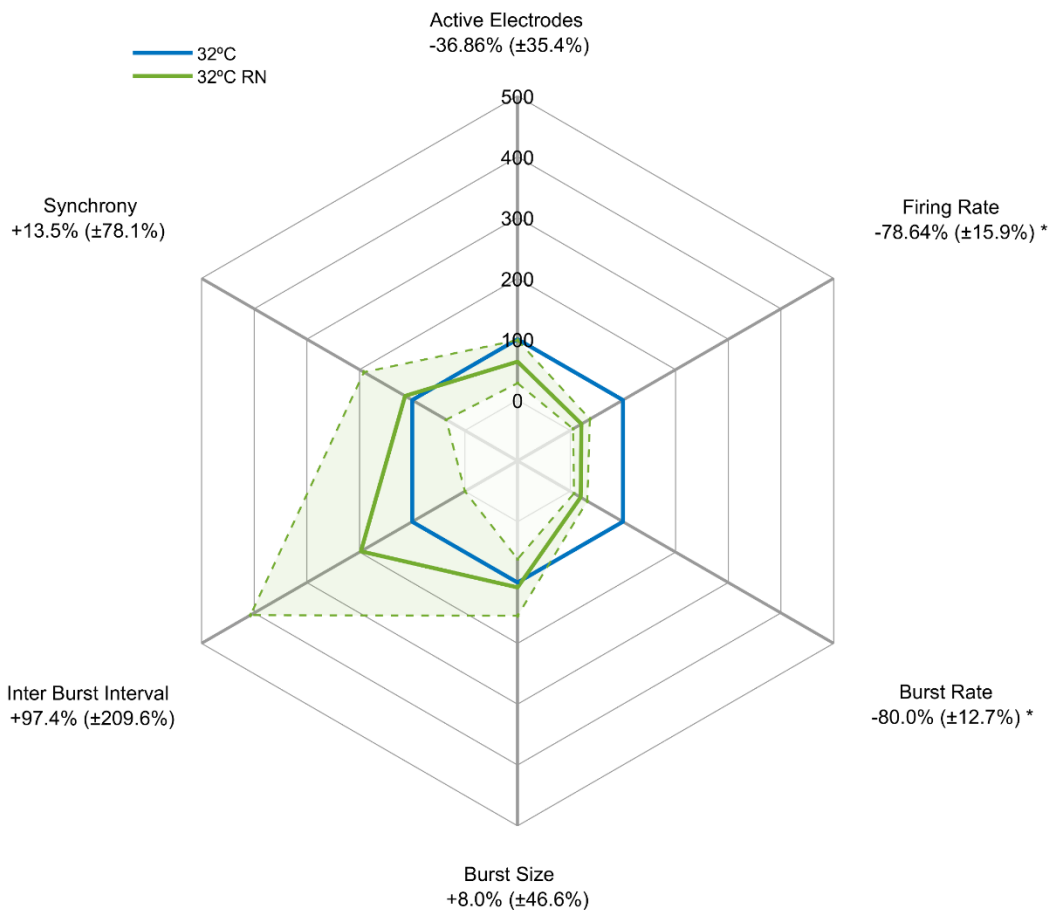

Figure 19 – Effect of RN1734 on neuronal activity at 32°C (below the expected activation temperature of TRPV4).
The effect of heating is displayed as the percentage variation from each parameter at 32°C + RN1734 to the parameter at baseline, 32°C, which is normalized as 100%. The value of these percentages and respective SD is shown below each metric. The color filled area represents the respective standard deviation. * Indicates a temperature-induced significant difference ($p < 0.05$).

4.4   Search for patterns of activity in long-term recordings

As previously stated, there is no literature regarding long-term dynamics of primary neuronal cultures on MEAs. Understanding possible patterns of activity would be of great assistance in the identification of ideal recording intervals, i.e., the smaller interval which is representative of the cultures activity for the whole day, for cultures at different stages

of maturation – DIVs. Past studies on longer recordings done by our group did hint the possibility to discern certain patterns of activity, however, these observations were not performed in a systematized way.

Thus, in this part of the dissertation, we sought to identify such specific dynamics of activity. We conducted 24 hours recordings of electrophysiology on primary hippocampal neuronal cultures at both DIV 7 and 14, stages which were chosen according to the known distinct activity profiles. Typically, at DIV7, the network is still in its maturation phase, still establishing synaptic connections and, therefore, exhibiting less electrical activity. On the other hand, at DIV14, cultures are usually already at a more mature stage that is characterized by more constant firing patterns[14–16].

For our initial approach, we started by observing the raster plot – the display of spiking activity registered by the electrodes over time – in search for visual cues of periodicity (Figure 20(A)). Subsequently, and to help visualize possible patterns, the activity was submitted to subsampling to obtain a "spike train" – the concatenation of all spiking events in all electrodes of a well for a specified time window (Figure 20(B)). Furthermore, these spiking counts for each interval were subjected to a convolution step, where the subsampled profile is filtered in order to identify the instantaneous firing rate for each well (Figure 20(C)). Throughout all the following experiments, related to the analysis of long duration recordings, we only considered wells where more than 10% of all electrodes were active.

At this point, we applied a Fourier Transform to the instantaneous firing rate to try to discern a possible set of frequencies composing the signal, which would correspond to patterns of network activity. Unexpectedly, this approach was not successful as no apparent patterns of activity were to be found across cultures in different MEAs for both DIV 7 and 14. Perhaps, this reflects the ongoing maturation of neuronal network. Although these are more developed at DIV14, and present more consistent firing events when compared with DIV7, there is the possibility that putative patterns of activity may only be found at later stages of maturation.

Moreover, to account for the possibility of periodicity of activity to arise only at certain phases of the recording, we implemented another approach. Its concept consisted on the division of the recording in equal time intervals and to subject each to an autocorrelation. More precisely, assuming 1 hour intervals, the instantaneous firing rate profile for each hour would slide on itself in both directions intending to find overlapping moments. To account for profiles that could be lost when splitting the intervals – imagining the possibility of important information to exist between the ending of an interval and the beginning of the consecutive one -, this autocorrelation was applied at time marks corresponding to half the considered interval for analysis, in this case, 30 minutes. This methodology was applied covering a wide selection of time intervals, ranging from 1 minute

to 6 hours. Unfortunately, we were once again unable to identify any relevant, and consistent pattern in the neuronal activity (Figure S12-Figure S14).
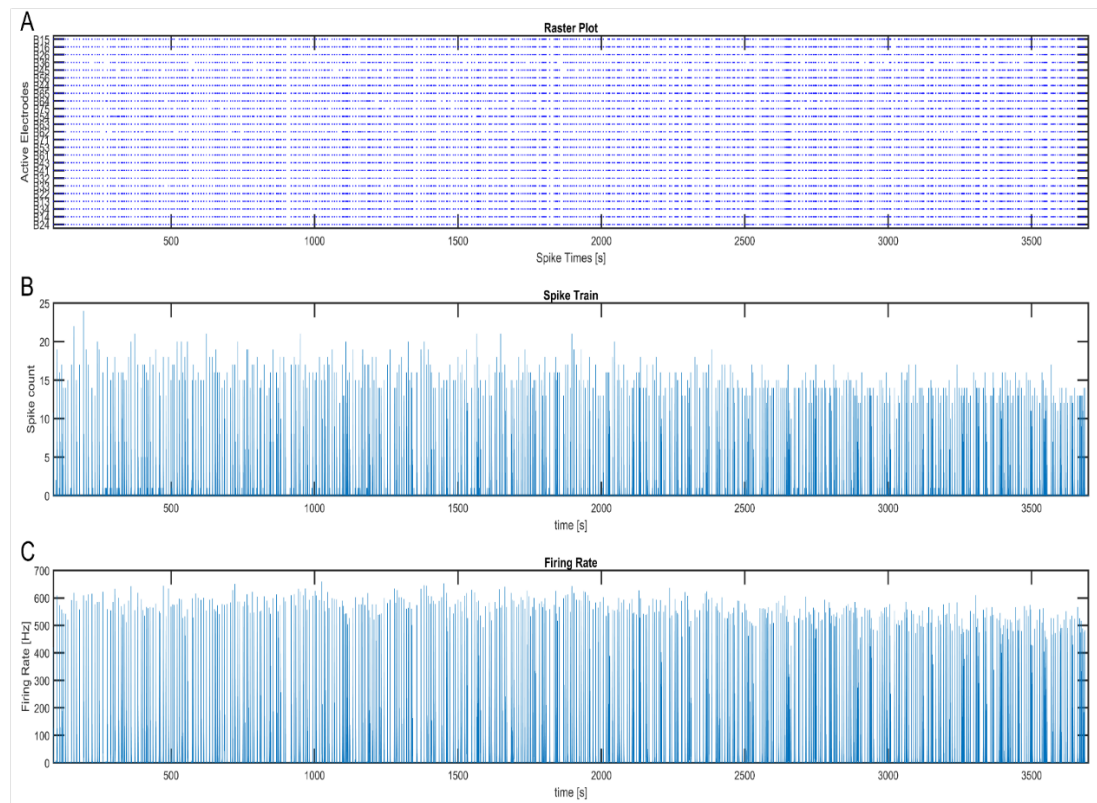

Figure 20 - Representative activity for 1 hour of DIV14.
A) Raster plot for all active electrodes of chosen well (Well B 09042021 DIV 14). Spike train with 200 Hz subsampling. C) Instantaneous firing rate.

4.5   Identification of ideal recording intervals

Thus, we started a new approach to analyze the 24 hours recordings and try to determine what would be the most appropriate recording interval to represent the neuronal activity over the 24 hours of that DIV.

The starting point for this new strategy consisted on the division of the whole recordings in equal intervals, and the calculation of the MFR for such intervals. The time intervals selected were – 1, 5, 15, 30, 60 and 180 minutes – and its representation can be seen in Figure 21 and Figure 22 for a well chosen from each MEA at DIV7 and DIV14, respectively. For example, for 1 minute intervals, the whole recording was divided in the 1440 minutes that compose 24 hours and, subsequently, the MFR for each electrode was calculated for each minute.

One advantage of this approach relies on how it helps clarify the activity profile for each culture and to observe the variations in the MFR over consecutive intervals and across distant timepoints. It can be noticed how, in general, there is a higher variation in the MFR of consecutive intervals according to how small the interval is. More precisely, for 1 minute intervals, it is highly likely to find a MFR profile that changes considerably from minute to

minute. Therefore, one can say that this interval is sensible to the "local" variations of the activity. Meanwhile, as we consider longer intervals, the variation profiles get tempered since these durations contain the wide variations registered for 1 minute intervals and, thus, more subtle outlines of the MFR evolution can be seen.

Furthermore, when looking at the bigger picture, one can notice the existence of whole-recording tendencies, such as increasing or decreasing profiles of activity (Figure 21, Figure 22 and Figure S7-Figure S11 (supplementary figures for all wells of all MEAs analyzed). These vary considerably both in cultures on the same MEA as well as across MEAs. At DIV7, cultures are especially prone to display distinct profiles. In the chosen well from each MEA (Figure 21), one can see both increasing (1st profile) and decreasing (2nd profile) global tendencies of the MFR over the recording time, or, as observed in the 3rd profile, for considerable periods of time there is little to no activity, but these are intercalated with transient peaks of intense network activity. Meanwhile, for DIV 14 (Figure 22), although the activity also presents increasing and decreasing profiles, these are objectively more constant around its average value, and some cultures even present steady activity profiles. Furthermore, one can observe that the MFR values are, in general, higher at DIV14 when compared to DIV7. These differences between different days of culture may be explained by the developmental process of neuronal cultures in vitro.

Typically, at DIV7, the network is still in its maturation phase, still establishing synaptic connections and, therefore, exhibiting less electrical activity. On the other hand, at DIV14, cultures are usually already at a more mature stage that is characterized by more constant firing patterns[14–16].
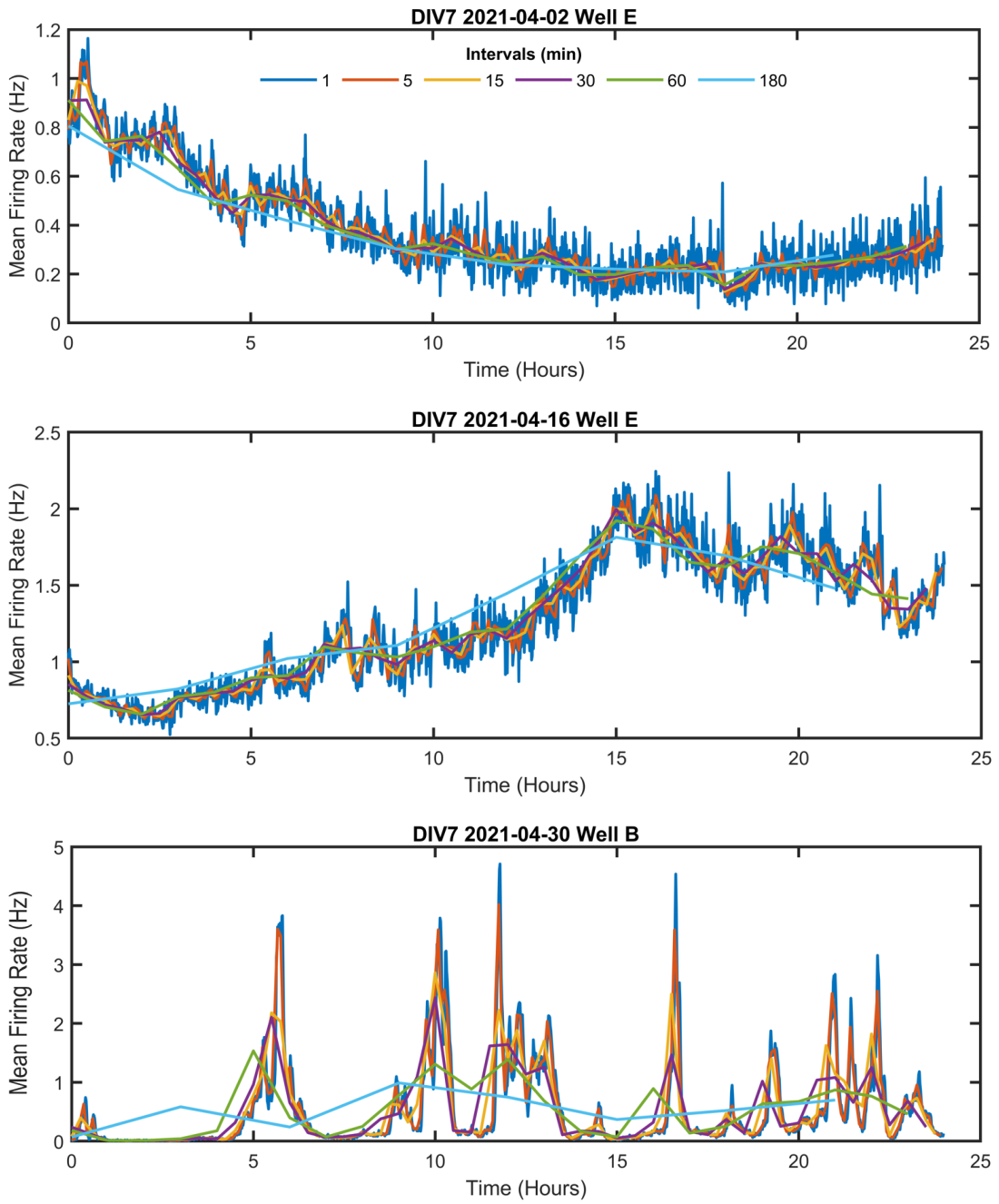
Figure 21 – Examples of profiles of MFR of different intervals for 24 hours at DIV 7. These are representative of the different activity patterns observed in the 24h recordings at DIV 7.
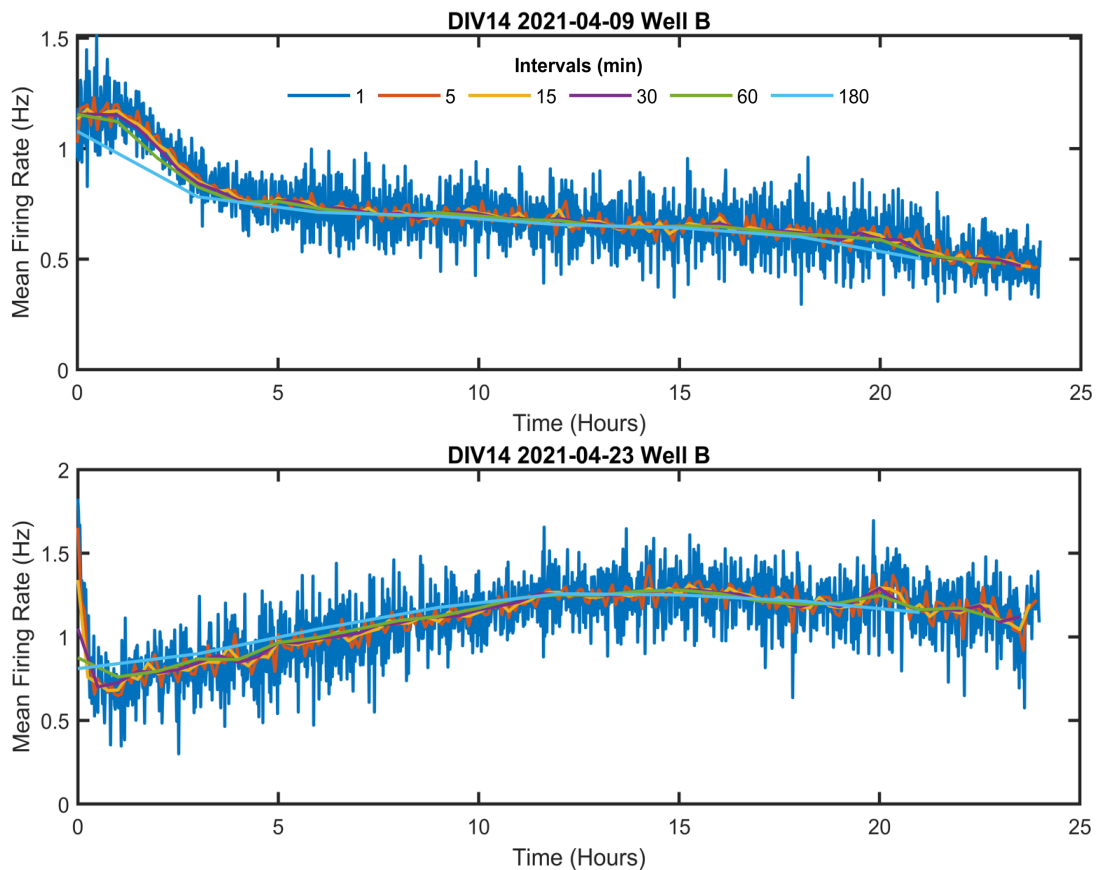
Figure 22 - Examples of profiles of MFR of different intervals for 24 hours at DIV 14.
These are representative of the different activity patterns observed in the 24h recordings
at DIV 14.

At this point, it was necessary to further analyze the data and attempt to
objectively identify what would be the most appropriate recording duration to represent
the activity of the 24 hours in each of the culture days. Thus, we proceeded to study, in
two different manners, how the activity for each of the chosen time intervals varies
throughout the whole recording.

Hence, before starting such analysis, there was an initial step of normalization of
the data according to the MFR of the whole 24 hours. In this way, the data from each
different culture can be directly compared and considered all together for prospective
studies.

4.6   Duration of recording to best capture neuronal activity across time

Here, our objective was to comprehend how similar the activity in one interval is
to any other random interval of the same duration. Thus, after obtaining the values
corresponding to the normalization of the data for each DIV (Figure 23(A) and Figure 24(A)),
we proceeded to visualize the data as a distribution of the normalized MFR (Figure 23(B)

and Figure 24(B)) through a boxplot chart. For each DIV, only one well is shown as representative of the whole data.

One can observe that, for DIV7, there is a wider distribution of the MFR when compared to DIV14. This tendency is perceptible for every considered time interval as both the box-delimited quartiles and the whiskers representing the last non-outlier values presented a narrower distribution. Meaning that a random value of the MFR for any interval has a higher probability to be closer to the median MFR of said interval for the 24 hours at DIV14 when compared to DIV7.
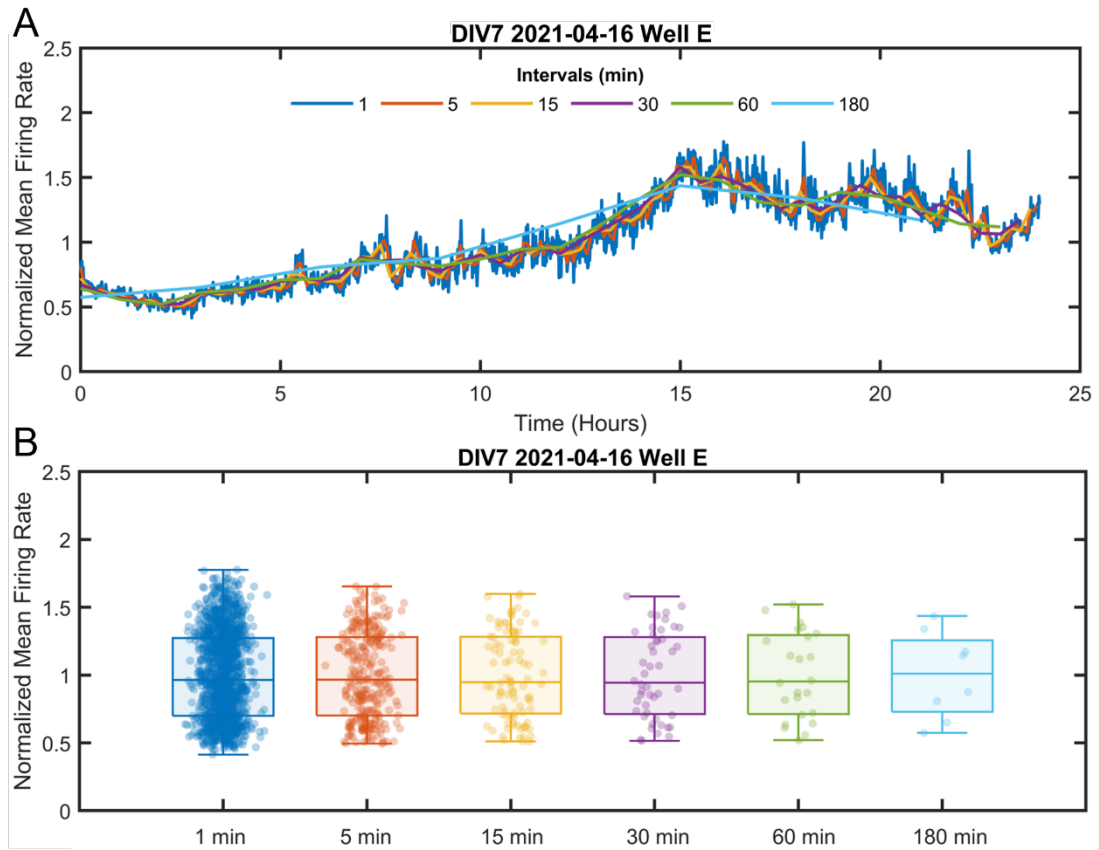

Figure 23 – Normalized MFR at DIV 7.
A) Profile of normalized MFR. B) Box chart distribution of normalized MFR. The MFR of each interval was normalized to the MFR of the 24 hours.
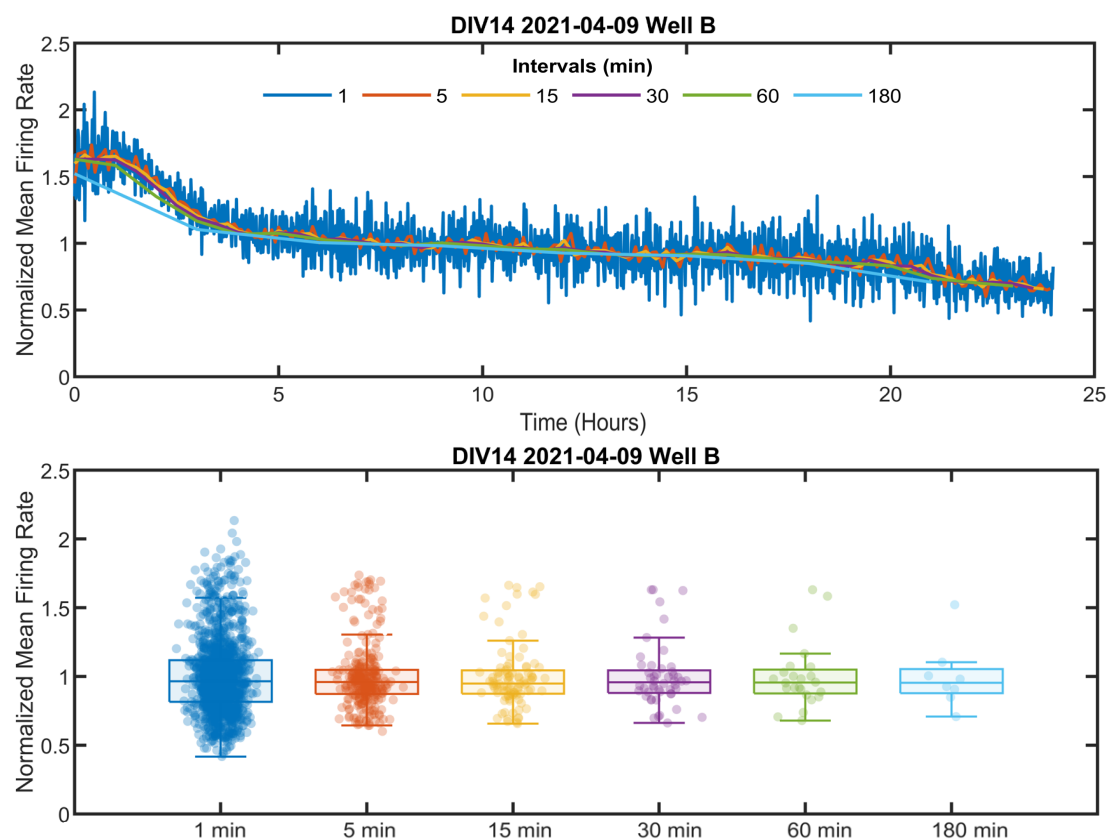
Figure 24 - Normalized MFR at DIV 14.
A) Profile of normalized MFR. B) Box chart distribution of normalized MFR. The MFR of each interval was normalized to the MFR of the 24 hours.

Furthermore, in order to quantify and ultimately compare these results, we calculated the coefficient of variation (CV) of each data set. The coefficient of variation is a relative measure of dispersion of a probability distribution, used to evaluate the precision and repeatability of a measurement and is calculated as the ratio of the standard deviation to the mean. That is, the lower the standard deviation of the data when compared to the mean, the lower the coefficient of variation, which translates in a higher probability of any point of the data set to be nearly representative of the overall data. In turn, a higher ratio of the standard deviation to the mean will result in higher values of the coefficient of variation, meaning that there is a lower probability of any data point to be representative of the whole data.

In this case, since we normalized the MFR of all intervals against the global 24h firing rate mean, the mean of each interval is now equal to 1 and, therefore, the coefficient of variation will be equal to the standard deviation. After calculating the coefficient of variation for each culture/well, all values were drawn together according to the respective DIV and time interval (Figure 25).

At DIV7, one can immediately spot a narrowing tendency of the distribution, which results from the typically inconsistent MFR profiles, however the median coefficient of variation is similar for each time interval (close to 50%). In sum, this indicates that, at DIV7, for all intervals, each measurement of activity will, most probably, be considerably

separated from the real value and reflect the high instability of the firing rate profile. Therefore, care should be taken when comparing the activity of neuronal cultures between DIVs at this culture stage or even, at the same DIV but with a long interval between recordings (ex. 6h interval between recordings).

At DIV14, the median of the distribution of the coefficient of variation is lower when compared with DIV7. It lies mostly below 30%, except for the 1-minute interval, where it is closer to 40%. This lower value reflects the fact that at DIV14 the neuronal activity is more stable when compared with DIV7, thus each sampling (represented here by each time interval) will be closer to the true value of the MFR.
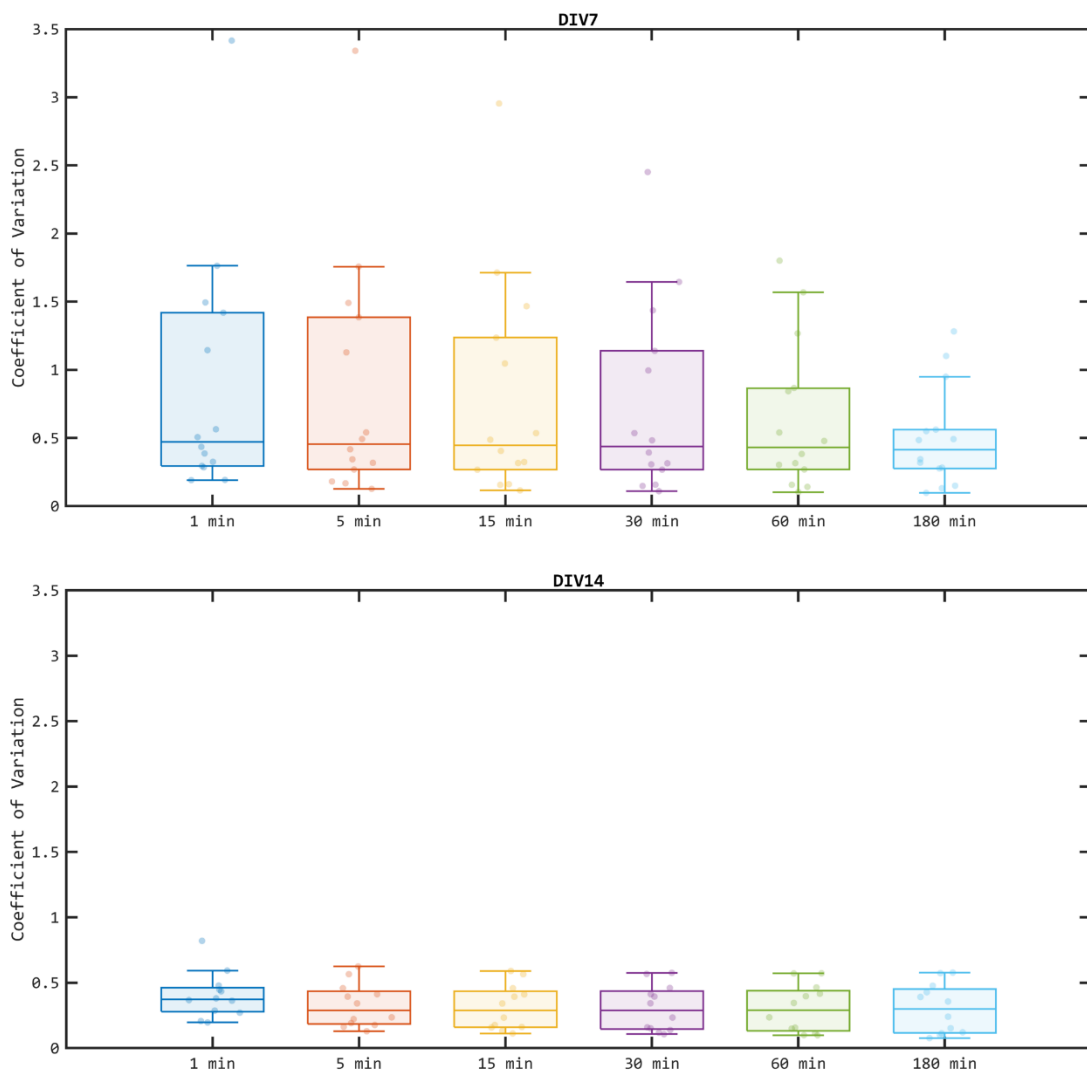

Figure 25 – Coefficient of variation for each recorded well and interval at DIV 7 and 14.

Additionally, one should notice a slight tendency for the distribution to widen according to the increasing interval duration at this DIV. This indicates that the CV of longer intervals has a higher variability across MEAs, and it is justified by the different profiles of firing rate observed and exemplified on Figure 24(A) (see also Figure S10Figure S11).

Nevertheless, the observations made here should be further investigated, in order to assure that the instability of the profile of firing rate observed is due to the intrinsic

activity of the cultures and not caused by the recording conditions. The MEA recording system is not provided with a complete incubation system able to maintain a controlled atmosphere. For this we had previously adapted an incubation system from a microscopy setup (ibidi stage top incubator) to be able to maintain the cells for such long periods of time while recording. Although we did not observe any problem in the viability of the cultures, slight changes to the atmosphere (e.g. CO_2 concentration, medium evaporation) during the recordings might account for some of the changes in activity observed across time.

4.7 Duration of recording to best capture neuronal activity for consecutive recordings

Finally, we set to investigate the change of activity between consecutive data points for each interval, or, in another words, verify the stability of activity between two consecutive intervals. This kind of information is extremely helpful when planning experimental designs involving the assessment of acute treatments, e.g., drugs with instantaneous effect, to assure that the possible effect caused in the network activity is related with the treatment and not with intrinsic changes on the activity of the network.

Hence, we started by calculating the differences in the normalized MFR between consecutive intervals of the same length. That is, for the 1440 1-minute intervals that divide the 24 hours, we calculated the absolute difference between the normalized MFR of the 2nd interval and the 1st interval, between the 3rd interval and 2nd interval and so on until there were 1439 values. This process was applied to all time intervals of all cultures and a representative profile can be seen in Figure 26(A) and Figure 27(A) for DIV7 and DIV14, respectively.
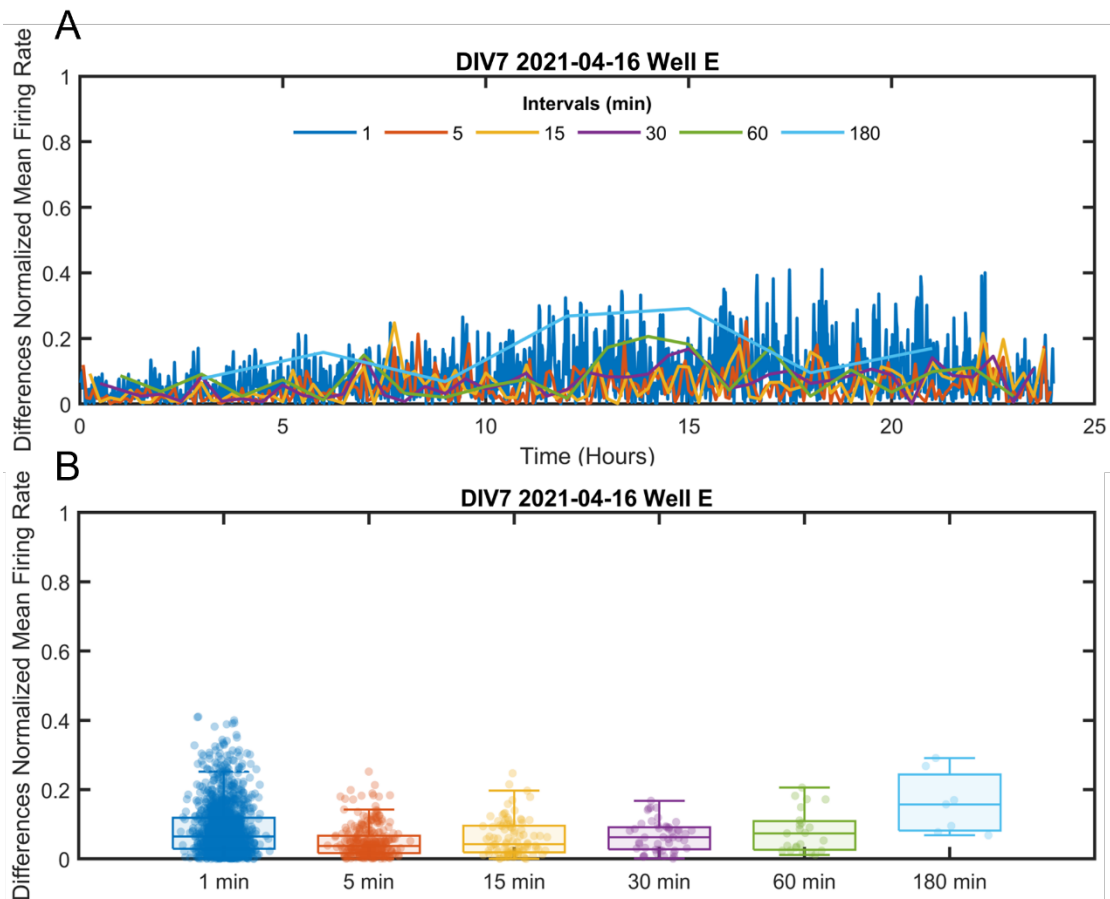
Figure 26 – Consecutive differences of normalized MFR at DIV 7.
A) Profile of consecutive differences of normalized MFR. B) Box chart distribution of such differences.

It should be noted beforehand that the differences profiles have apparently shorter spans according to the increasing length of the time interval. That is, for the 180-minutes intervals, the value corresponding to the difference between the 2nd and the 1st point is represented at the location of the 2nd value (3 hours), while the last value, corresponding to the difference between the 8th and 7th values, is represented at the 7th position (21 hours).

There are some considerable differences when observing both profiles. One can notice a larger range between the differences registered in 1-minute intervals at DIV14 when compared to other time intervals (Figure 27(A)). However, at the 1st value for 180 minutes and the 2nd for 60 minutes, the respective values are disproportionally higher due to the influence of the decreasing global tendency of the activity, especially seen in the initial part of the recording. These discrepancies between time intervals can be more easily seen in Figure 27(B) where the distribution of the total differences values for each interval are shown.

At DIV7, the differences appear in loosely similar ranges for all intervals, meaning that, for all intervals, there are more identical consecutive variations of the MFR, which corroborates what is seen in the profiles of Figure 21 (Figure 26).
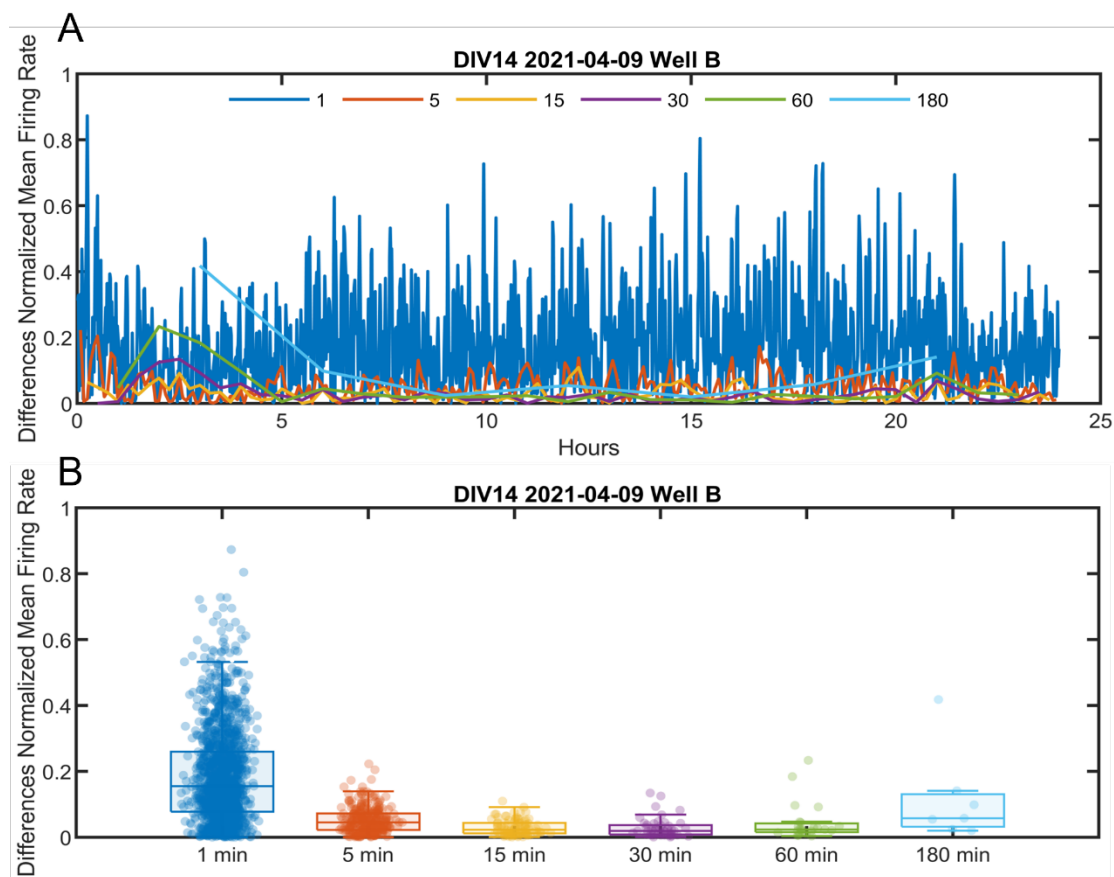
Figure 27 - Consecutive differences of normalized MFR at DIV 14.
A) Profile of consecutive differences of normalized MFR. B) Box chart distribution of such differences.

Finally, we calculated the median of all differences values for each interval in each well of each DIV. The median was used instead of the mean considering how this metric is more resistant to the presence of particularly dissonant events. Consequently, the medians were joined together according to the interval and the DIV, and its distribution is shown in Figure 28. Thus, we were hoping to conclude on the most appropriate recording interval in which one can obtain the least variation to the immediately consecutive one.

At DIV7, there is no significant variation between intervals, except for 180 minutes. Meaning that, between two consecutive 180-minutes intervals, the activity of that culture is expected to vary more than in any other time interval. This effect is mostly caused by the global variations present in most profiles. Additionally, one can identify 5-minutes intervals as the smallest interval with lower median, which reflects its preferable use, at DIV7, for acute assays.

For cultures at DIV14, the observable profile is considerably different. There is, however, still an influence of the global variations of network activity that equally affects the variation at 180-minutes intervals. The big difference towards DIV7 relies on the fact that 1-minute intervals appear to be the least optimal to ensure that the activity between two consecutive intervals is similar. This effect is related to the wide local variations seen

in Figure 22. The 5-minutes time intervals are affected in the same manner but to a lesser extent. Finally, the 15 and 30 -minutes intervals present similar median values (around 0.03) and thus, for practical reasons, the smaller interval should be considered as the optimal one. In sum, at DIV14, the time interval presenting less variation in normalized MFR for consecutive intervals, is that of 15 minutes.
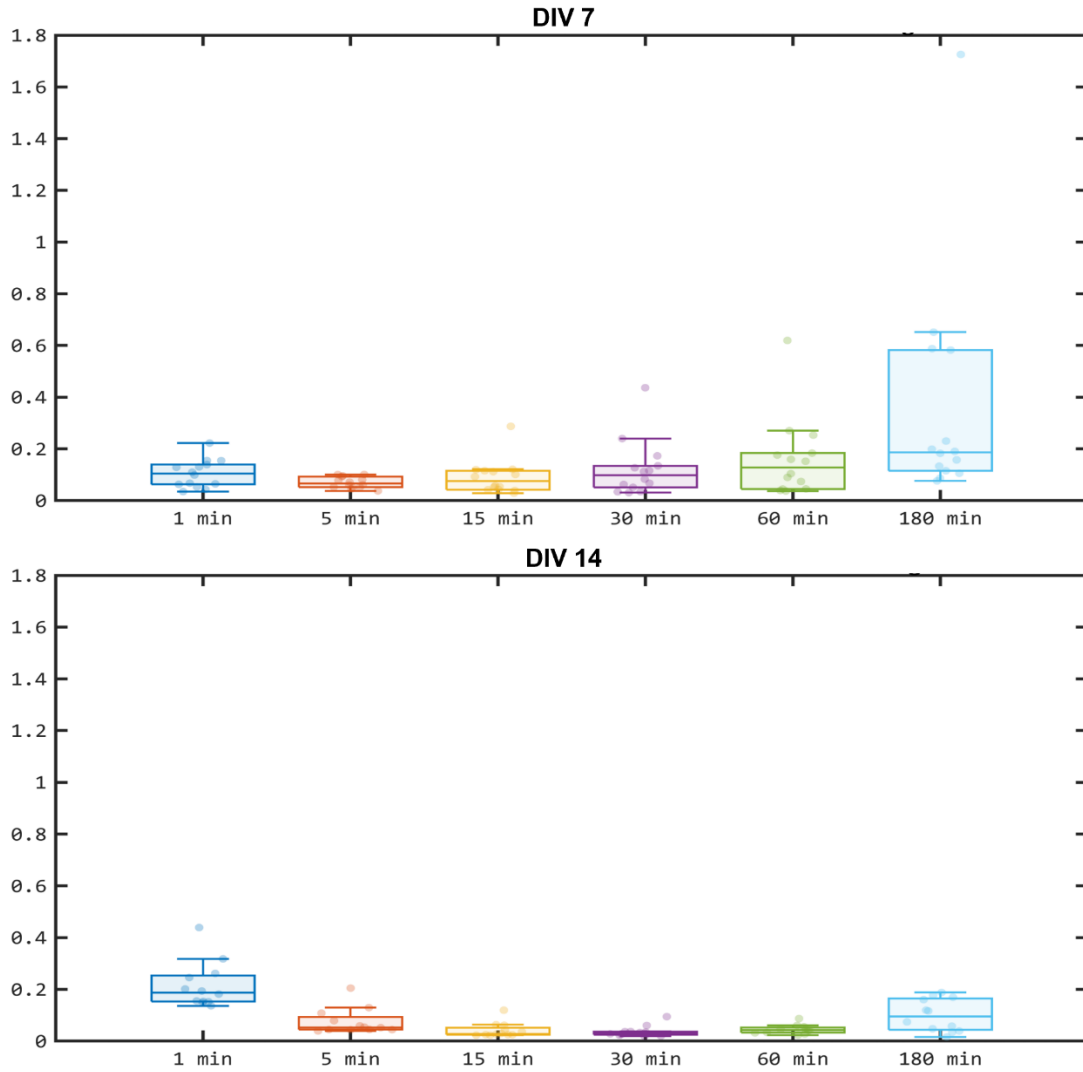

Figure 28 - Distribution of the median of all consecutive differences of normalized MFR obtained from all recorded wells at DIV 7 and 14.

Chapter 5

5.1 Concluding Remarks

One of the most valued advantages of MEAs relies on the capacity to simultaneously perform non-invasive recordings and long-term following of neuronal cultures. For this reason, there has been an increase in use of MEA-based assays in the field of neurosciences. However, this technique still faces unresolved challenges. Here, we focused on temperature impact on neuronal activity and on the description of the dynamics of neuronal activity over continuous long-term recordings.

In the first part of the work, after verifying that the temperature set in the MEA2100 recording system was considerably different from the temperatures registered in the cellular medium, we performed a calibration of the recording system in order to know the relation between the set temperature and the "real" cellular medium temperature. Furthermore, we have also demonstrated that a 10 min interval is sufficient for the culture medium to stabilize when the temperature is raised in 1℃. From the study of the alterations in electrophysiology of neuronal cultures recorded at physiological (37°C) and hyperthermic (39°C) conditions, we determined that the increase of the culture temperature leads to a significant reduction of both the firing and burst rate. Although the molecular mechanisms that relate changes of temperature with neuronal activity are not well characterized, we selected the TRPV4 ion channel as a potential target. This channel is temperature sensitive, changing the voltage gating membrane potentials according to temperature shifts. However, the inhibition of this channel resulted in a higher reduction of neuronal activity at all temperatures measured. Thus, we concluded, that TRPV4 is most probably not directly involved in the reduction of activity related with the increase of temperature.

Regarding the investigation of activity patterns in 24h recordings at DIV 7 and 14, we could not find any discernable periodicity in the activity profiles, which can, perhaps, be associated to the ongoing, yet incomplete, maturation process at such DIVs. In line with this, the activity profile observed at DIV 14 is more stable when compared with DIV7, as it would be expected due to network maturation. Nonetheless, we sought to identify the most

appropriate recording interval at both DIVs by determining the variability between the firing rate determined at a certain time interval and the overall mean firing rate calculated for the entire recording session (24h). The appropriate recording interval will, ideally, minimize the sampling error and capture accurately the activity of the culture at a given DIV. Thus, we divided all recordings in different time intervals (1, 5, 15, 30, 60 and 180 minutes), and calculated the mean firing rate for each interval. The analysis of the coefficient of variation of the firing rate for each interval revealed that, at DIV 7, the longer the recording the smaller the CV across cultures, while, for DIV14, there is no apparent difference from the 5 minute interval to the higher ones, indicating that the sampling error will be similar regardless of the recording time chosen. Thus, decision on the best recording interval to capture the activity of cultures should be taken according to the needs of the protocol. Yet, further experiments should be performed to better characterize the stability of activity across the 24h to make sure that the observed profiles are not the result of any limitation of the incubation system of the MEA recording system (e.g. CO_2 stability, control of medium evaporation).

At last, we assessed the stability of the recorded firing rate in consecutive intervals. Here, the lower the difference in activity of consecutive intervals the most stable is the activity at that time frame. For DIV 7, the lower median values of those differences were found at intervals of 5 and 15 minutes and, at DIV14, the lower values were found at intervals of 15 and 30 minutes. Thus, our recommendation is to use such recording time intervals when studying acute perturbations to neuronal cultures around such DIVs.

5.2   Future Perspectives

Throughout this dissertation we were able to enrich our knowledge on the activity of primary hippocampal neuronal cultures studied with MEAs and, remarkably, provide valuable insights into the optimization of future experimental designs. However, some key points can be detailed as essential to improve. The incubation system used throughout recordings to help maintain the desired conditions should be further characterized as to, for example, assure the stability of the atmosphere, especially during long recordings and experiments with higher temperatures. The activity of TRPV4 should be characterized more effectively, possibly with the addition of an agonist to the experimental design. Finally, regarding the identification of temporal patterns of activity in the neuronal networks, additional DIVs should be tested, specifically at later stages of maturation where the activity is known to be more stable.

References

1.   Kandel ER, Schwartz JH, Jessel TM, Siegelbaum SA, Hudspeth AJ, Mack S. *Principles of Neural Science, 5th Edition*. 5th Edition.; 2013.

2.   Purves D, Augustine GJ, Fitzpatrick D, et al. *Neuroscience, 6th Edition*. 6th Edition.; 2018.

3.   Sousa AMM, Meyer KA, Santpere G, Gulden FO, Sestan N. Evolution of the Human Nervous System Function, Structure, and Development. *Cell*. 2017;170(2):226-247. doi:10.1016/j.cell.2017.06.036

4.   Keller JM, Frega M. Past, Present, and Future of Neuronal Models In Vitro. *Adv Neurobiol*. 2019;22:3-17. doi:10.1007/978-3-030-11135-9_1

5.   le Feber J. In Vitro Models of Brain Disorders. *Adv Neurobiol*. 2019;22:19-49. doi:10.1007/978-3-030-11135-9_2

6.   Nam Y, Wheeler BC. In vitro microelectrode array technology and neural recordings. *Crit Rev Biomed Eng*. 2011;39(1):45-61. doi:10.1615/critrevbiomedeng.v39.i1.40

7.   Obien MEJ, Deligkaris K, Bullmann T, Bakkum DJ, Frey U. Revealing neuronal function through microelectrode array recordings. *Front Neurosci*. 2015;8. doi:10.3389/fnins.2014.00423

8.   Pozzi D. Evaluation of in vitro neuronal networks for the study of spontaneous activity. *STEMedicine*. 2020;1(2):e35-e35. doi:10.37175/stemedicine.v1i2.35

9.   Vassallo A, Chiappalone M, De Camargos Lopes R, et al. A multi-laboratory evaluation of microelectrode array-based measurements of neural network activity for acute neurotoxicity testing. *NeuroToxicology*. 2017;60:280-292. doi:10.1016/j.neuro.2016.03.019

10.   Novellino A, Scelfo B, Palosaari T, et al. Development of Micro-Electrode Array Based Tests for Neurotoxicity: Assessment of Interlaboratory Reproducibility with Neuroactive Chemicals. *Front Neuroengineering*. 2011;4. doi:10.3389/fneng.2011.00004

11.   Walter EJ, Carraretto M. The neurological and cognitive consequences of hyperthermia. *Crit Care*. 2016;20. doi:10.1186/s13054-016-1376-4

12.   Takeya M. Intrinsic factors involved in the depression of neuronal activity induced by temperature increase in rat hippocampal neurons. *Kurume Med J*. 2001;48(4):295-306. doi:10.2739/kurumemedj.48.295

13. Peña E de la, Mälkiä A, Vara H, et al. The Influence of Cold Temperature on Cellular Excitability of Hippocampal Networks. *PLOS ONE*. 2012;7(12):e52475. doi:10.1371/journal.pone.0052475

14. Chiappalone M, Bove M, Vato A, Tedesco M, Martinoia S. Dissociated cortical networks show spontaneously correlated activity patterns during in vitro development. *Brain Research*. 2006;1093(1):41-53. doi:10.1016/j.brainres.2006.03.049

15. Reinartz S. Long-Term Activity Dynamics of Single Neurons and Networks. *Adv Neurobiol*. 2019;22:331-350. doi:10.1007/978-3-030-11135-9_14

16. Negri J, Menon V, Young-Pearse TL. Assessment of Spontaneous Neuronal Activity In Vitro Using Multi-Well Multi-Electrode Arrays: Implications for Assay Development. *eNeuro*. 2020;7(1). doi:10.1523/ENEURO.0080-19.2019

17. Sterratt D, Graham B, Gillies A, Willshaw D. *Principles of Computational Modelling in Neuroscience*. Cambridge University Press; 2011. doi:10.1017/CBO9780511975899

18. Hodgkin AL, Huxley AF, Katz B. Measurement of current-voltage relations in the membrane of the giant axon of Loligo. *J Physiol*. 1952;116(4):424-448.

19. Hodgkin AL, Huxley AF. Currents carried by sodium and potassium ions through the membrane of the giant axon of Loligo. *J Physiol*. 1952;116(4):449-472.

20. Hodgkin AL, Huxley AF. The components of membrane conductance in the giant axon of Loligo. *J Physiol*. 1952;116(4):473-496.

21. Hodgkin AL, Huxley AF. The dual effect of membrane potential on sodium conductance in the giant axon of Loligo. *J Physiol*. 1952;116(4):497-506.

22. Hodgkin AL, Huxley AF. A quantitative description of membrane current and its application to conduction and excitation in nerve. *J Physiol*. 1952;117(4):500-544.

23. Beeman D. Hodgkin-Huxley Model. In: Jaeger D, Jung R, eds. *Encyclopedia of Computational Neuroscience*. Springer; 2013:1-13. doi:10.1007/978-1-4614-7320-6_127-3

24. Raghavan M, Fee D, Barkhaus PE. Chapter 1 - Generation and propagation of the action potential. In: Levin KH, Chauvel P, eds. *Handbook of Clinical Neurology*. Vol 160. Clinical Neurophysiology: Basis and Technical Aspects. Elsevier; 2019:3-22. doi:10.1016/B978-0-444-64032-1.00001-1

25. Kuang S, Wang J, Zeng T, Cao A. Thermal impact on spiking properties in Hodgkin-Huxley neuron with synaptic stimulus. *Pramana - J Phys*. 2008;70(1):183-190. doi:10.1007/s12043-008-0016-1

26. Hille B. *Ion Channels of Excitable Membranes*. 3rd edn. Sinauer Associates, Sunderland, MA; 2001.

27. Samanta A, Hughes TET, Moiseenkova-Bell VY. Transient Receptor Potential (TRP) Channels. *Subcell Biochem*. 2018;87:141-165. doi:10.1007/978-981-10-7757-9_6

28. Zheng J, Trudeau MC, eds. *Handbook of Ion Channels*. CRC Press; 2015. doi:10.1201/b18027

29. Kauer JA, Gibson HE. Hot flash: TRPV channels in the brain. *Trends in Neurosciences*. 2009;32(4):215-224. doi:10.1016/j.tins.2008.12.006

30. Gibson HE, Edwards JG, Page RS, Van Hook MJ, Kauer JA. TRPV1 Channels Mediate Long-Term Depression at Synapses on Hippocampal Interneurons. *Neuron*. 2008;57(5):746-759. doi:10.1016/j.neuron.2007.12.027

31. Sharif-Naeini R, Ciura S, Bourque CW. TRPV1 Gene Required for Thermosensory Transduction and Anticipatory Secretion from Vasopressin Neurons during Hyperthermia. *Neuron*. 2008;58(2):179-185. doi:10.1016/j.neuron.2008.02.013

32. Redmon SN, Shibasaki K, Križaj D. Transient Receptor Potential Cation Channel Subfamily V Member 4 (TRPV4). In: Choi S, ed. *Encyclopedia of Signaling Molecules*. Springer New York; 2017:1-11. doi:10.1007/978-1-4614-6438-9_101977-1

33. Toft-Bertelsen TL, MacAulay N. TRPing to the Point of Clarity: Understanding the Function of the Complex TRPV4 Ion Channel. *Cells*. 2021;10(1):165. doi:10.3390/cells10010165

34. Shibasaki K, Tominaga M, Ishizaki Y. Hippocampal neuronal maturation triggers post-synaptic clustering of brain temperature-sensor TRPV4. *Biochemical and Biophysical Research Communications*. 2015;458(1):168-173. doi:10.1016/j.bbrc.2015.01.087

35. Shibasaki K, Suzuki M, Mizuno A, Tominaga M. Effects of Body Temperature on Neural Activity in the Hippocampus: Regulation of Resting Membrane Potentials by Transient Receptor Potential Vanilloid 4. *J Neurosci*. 2007;27(7):1566-1575. doi:10.1523/JNEUROSCI.4284-06.2007

36. FAY T, SMITH GW. OBSERVATIONS ON REFLEX RESPONSES DURING PROLONGED PERIODS OF HUMAN REFRIGERATION. *Archives of Neurology & Psychiatry*. 1941;45(2):215-222. doi:10.1001/archneurpsyc.1941.02280140025002

37. Darby WG, Grace MS, Baratchi S, McIntyre P. Modulation of TRPV4 by diverse mechanisms. *The International Journal of Biochemistry & Cell Biology*. 2016;78:217-228. doi:10.1016/j.biocel.2016.07.012

38. Voets T, Prenen J, Vriens J, et al. Molecular Determinants of Permeation through the Cation Channel TRPV4 *. *Journal of Biological Chemistry*. 2002;277(37):33704-33710. doi:10.1074/jbc.M204828200

39. Nilius B, Voets T. The puzzle of TRPV4 channelopathies. *EMBO Rep*. 2013;14(2):152-163. doi:10.1038/embor.2012.219

40. Shibasaki K, Sugio S, Takao K, et al. TRPV4 activation at the physiological temperature is a critical determinant of neuronal excitability and behavior. *Pflugers Arch - Eur J Physiol*. 2015;467(12):2495-2507. doi:10.1007/s00424-015-1726-0

41. Güler AD, Lee H, Iida T, Shimizu I, Tominaga M, Caterina M. Heat-Evoked Activation of the Ion Channel, TRPV4. *J Neurosci*. 2002;22(15):6408-6414. doi:10.1523/JNEUROSCI.22-15-06408.2002

42. Matsumoto H, Sugio S, Seghers F, et al. Retinal Detachment-Induced Müller Glial Cell Swelling Activates TRPV4 Ion Channels and Triggers Photoreceptor Death at Body Temperature. *J Neurosci*. 2018;38(41):8745-8758. doi:10.1523/JNEUROSCI.0897-18.2018

43. Watanabe H, Vriens J, Suh SH, Benham CD, Droogmans G, Nilius B. Heat-evoked Activation of TRPV4 Channels in a HEK293 Cell Expression System and in Native Mouse Aorta Endothelial Cells*. *Journal of Biological Chemistry*. 2002;277(49):47044-47051. doi:10.1074/jbc.M208277200

44. Garcia-Elias A, Mrkonjic S, Pardo-Pastor C, et al. Phosphatidylinositol-4,5-biphosphate-dependent rearrangement of TRPV4 cytosolic tails enables channel activation by physiological stimuli. *Proc Natl Acad Sci U S A*. 2013;110(23):9553-9558. doi:10.1073/pnas.1220231110

45. Vriens J, Watanabe H, Janssens A, Droogmans G, Voets T, Nilius B. Cell swelling, heat, and chemical agonists use distinct pathways for the activation of the cation channel TRPV4. *Proc Natl Acad Sci U S A*. 2004;101(1):396-401. doi:10.1073/pnas.0303329101

46. Klausen TK, Janssens A, Prenen J, et al. Single point mutations of aromatic residues in transmembrane helices 5 and -6 differentially affect TRPV4 activation by 4α-PDD and hypotonicity: implications for the role of the pore region in regulating TRPV4 activity. *Cell Calcium*. 2014;55(1):38-47. doi:10.1016/j.ceca.2013.11.001

47. Vriens J, Owsianik G, Janssens A, Voets T, Nilius B. Determinants of 4 alpha-phorbol sensitivity in transmembrane domains 3 and 4 of the cation channel TRPV4. *J Biol Chem*. 2007;282(17):12796-12803. doi:10.1074/jbc.M610485200

48. Lee EJ, Shin SH, Chun J, Hyun S, Kim Y, Kang SS. The modulation of TRPV4 channel activity through its Ser 824 residue phosphorylation by SGK1. *Animal Cells and Systems*. 2010;14(2):99-114. doi:10.1080/19768354.2010.486939

49. Wegierski T, Lewandrowski U, Müller B, Sickmann A, Walz G. Tyrosine Phosphorylation Modulates the Activity of TRPV4 in Response to Defined Stimuli*. *Journal of Biological Chemistry*. 2009;284(5):2923-2933. doi:10.1074/jbc.M805357200

50. Vincent F, Acevedo A, Nguyen MT, et al. Identification and characterization of novel TRPV4 modulators. *Biochemical and Biophysical Research Communications*. 2009;389(3):490-494. doi:10.1016/j.bbrc.2009.09.007

51. Hong Z, Tian Y, Qi M, et al. Transient Receptor Potential Vanilloid 4 Inhibits γ-Aminobutyric Acid-Activated Current in Hippocampal Pyramidal Neurons. *Frontiers in Molecular Neuroscience*. 2016;9:77. doi:10.3389/fnmol.2016.00077

52. Zhou L, Xu W, An D, et al. *Effect of Transient Receptor Potential Vanilloid 4 Activation on the Delayed Rectifier Potassium Current in the Hippocampal Pyramidal Neurons and Kv Subunit Expression in the Hippocampi of Mice*. In Review; 2020. doi:10.21203/rs.3.rs-24895/v1

53. Hoshi Y, Okabe K, Shibasaki K, et al. Ischemic Brain Injury Leads to Brain Edema via Hyperthermia-Induced TRPV4 Activation. *J Neurosci*. 2018;38(25):5700-5709. doi:10.1523/JNEUROSCI.2888-17.2018

54. Shibasaki K, Yamada K, Miwa H, et al. Temperature elevation in epileptogenic foci exacerbates epileptic discharge through TRPV4 activation. *Lab Invest*. 2020;100(2):274-284. doi:10.1038/s41374-019-0335-5

55. Verkhratsky A, Krishtal OA, Petersen OH. From Galvani to patch clamp: the development of electrophysiology. *Pflugers Arch - Eur J Physiol*. 2006;453(3):233-247. doi:10.1007/s00424-006-0169-z

56. Liu M-G, Chen X-F, He T, Li Z, Chen J. Use of multi-electrode array recordings in studies of network synaptic plasticity in both time and space. *Neurosci Bull*. 2012;28(4):409-422. doi:10.1007/s12264-012-1251-5

57. Caton R. Electrical Currents of the Brain. *The Journal of Nervous and Mental Disease*. 1875;2(4):610.

58. Berger H. Über das Elektrenkephalogramm des Menschen. *Archiv f Psychiatrie*. 1929;87(1):527-570. doi:10.1007/BF01797193

59. Buzsáki G, Anastassiou CA, Koch C. The origin of extracellular fields and currents — EEG, ECoG, LFP and spikes. *Nature Reviews Neuroscience*. 2012;13(6):407-420. doi:10.1038/nrn3241

60. Einevoll GT, Kayser C, Logothetis NK, Panzeri S. Modelling and analysis of local field potentials for studying the function of cortical circuits. *Nature Reviews Neuroscience*. 2013;14(11):770-785. doi:10.1038/nrn3599

61. Verkhratsky A, Parpura V. History of electrophysiology and the patch clamp. *Methods Mol Biol*. 2014;1183:1-19. doi:10.1007/978-1-4939-1096-0_1

62. Neher E, Sakmann B, Steinbach JH. The extracellular patch clamp: a method for resolving currents through individual open channels in biological membranes. *Pflugers Arch*. 1978;375(2):219-228. doi:10.1007/BF00584247

63. Wood C, Williams C, Waldron GJ. Patch clamping by numbers. *Drug Discovery Today*. 2004;9(10):434-441. doi:10.1016/S1359-6446(04)03064-8

64. Thomas CA, Springer PA, Loeb GE, Berwald-Netter Y, Okun LM. A miniature microelectrode array to monitor the bioelectric activity of cultured cells. *Experimental Cell Research*. 1972;74(1):61-66. doi:10.1016/0014-4827(72)90481-8

65. Pine J. Recording action potentials from cultured neurons with extracellular microcircuit electrodes. *Journal of Neuroscience Methods*. 1980;2(1):19-31. doi:10.1016/0165-0270(80)90042-4

66. Egert U, Schlosshauer B, Fennrich S, et al. A novel organotypic long-term culture of the rat hippocampus on substrate-integrated multielectrode arrays. *Brain Res Brain Res Protoc*. 1998;2(4):229-242. doi:10.1016/s1385-299x(98)00013-0

67. Nisch W, Böck J, Egert U, Hämmerle H, Mohr A. A thin film microelectrode array for monitoring extracellular neuronal activity in vitro. *Biosensors and Bioelectronics*. 1994;9(9):737-741. doi:10.1016/0956-5663(94)80072-3

68. Kim R, Joo S, Jung H, Hong N, Nam Y. Recent trends in microelectrode array technology for in vitro neural interface platform. *Biomed Eng Lett*. 2014;4(2):129-141. doi:10.1007/s13534-014-0130-6

69. Gold C, Henze DA, Koch C. Using extracellular action potential recordings to constrain compartmental models. *J Comput Neurosci*. 2007;23(1):39-58. doi:10.1007/s10827-006-0018-2

70. Quiroga RQ. Principles of Neural Coding. :625.

71. Gold C, Henze DA, Koch C, Buzsáki G. On the Origin of the Extracellular Action Potential Waveform: A Modeling Study. *Journal of Neurophysiology*. 2006;95(5):3113-3128. doi:10.1152/jn.00979.2005

72. Hines ML, Carnevale NT. The NEURON simulation environment. *Neural Comput*. 1997;9(6):1179-1209. doi:10.1162/neco.1997.9.6.1179

73. Heinricher MM. 2 Principles of Extracellular Single-Unit Recording. In: *Microelectrode Recording in Movement Disorder Surgery*. 2004th ed. Thieme Verlag; 2004. doi:10.1055/b-0034-56092

74. Terzuolo CA, Araki T. An Analysis of Intra- Versus Extracellular Potential Changes Associated with Activity of Single Spinal Motoneurons*. *Annals of the New York Academy of Sciences*. 1961;94(2):547-558. doi:https://doi.org/10.1111/j.1749-6632.1961.tb35558.x

75. Jäckel D, Frey U, Fiscella M, Franke F, Hierlemann A. Applicability of independent component analysis on high-density microelectrode array recordings. *Journal of Neurophysiology*. 2012;108(1):334-348. doi:10.1152/jn.01106.2011

76. Lempka SF, Johnson MD, Moffitt MA, Otto KJ, Kipke DR, McIntyre CC. Theoretical analysis of intracortical microelectrode recordings. *J Neural Eng*. 2011;8(4):045006. doi:10.1088/1741-2560/8/4/045006

77. Martinez J, Pedreira C, Ison MJ, Quian Quiroga R. Realistic simulation of extracellular recordings. *Journal of Neuroscience Methods*. 2009;184(2):285-293. doi:10.1016/j.jneumeth.2009.08.017

78. Hassibi A, Navid R, Dutton RW, Lee TH. Comprehensive study of noise processes in electrode electrolyte interfaces. *Journal of Applied Physics*. 2004;96(2):1074-1082. doi:10.1063/1.1755429

79. Liu X, Demosthenous A, Donaldson N. On the Noise Performance of Pt Electrodes. In: *2007 29th Annual International Conference of the IEEE Engineering in Medicine and Biology Society*. ; 2007:434-436. doi:10.1109/IEMBS.2007.4352316

80. Harrison RR. The Design of Integrated Circuits to Observe Brain Activity. *Proceedings of the IEEE*. 2008;96(7):1203-1216. doi:10.1109/JPROC.2008.922581

81. Camuñas-Mesa LA, Quiroga RQ. A Detailed and Fast Model of Extracellular Recordings. *Neural Computation*. 2013;25(5):1191-1212. doi:10.1162/NECO_a_00433

82. Ward MP, Rajdev P, Ellison C, Irazoqui PP. Toward a comparison of microelectrodes for acute and chronic recordings. *Brain Research*. 2009;1282:183-200. doi:10.1016/j.brainres.2009.05.052

83. Viswam V, Obien MEJ, Franke F, Frey U, Hierlemann A. Optimal Electrode Size for Multi-Scale Extracellular-Potential Recording From Neuronal Assemblies. *Front Neurosci*. 2019;13. doi:10.3389/fnins.2019.00385

84. Nelson MJ, Pouget P, Nilsen EA, Patten CD, Schall JD. Review of signal distortion through metal microelectrode recording circuits and filters. *Journal of Neuroscience Methods*. 2008;169(1):141-157. doi:10.1016/j.jneumeth.2007.12.010

85. Hennig MH, Hurwitz C, Sorbaro M. Scaling Spike Detection and Sorting for Next-Generation Electrophysiology. *Adv Neurobiol*. 2019;22:171-184. doi:10.1007/978-3-030-11135-9_7

86. Cotterill E, Eglen SJ. Burst Detection Methods. *Adv Neurobiol*. 2019;22:185-206. doi:10.1007/978-3-030-11135-9_8

87. Johnstone AFM, Gross GW, Weiss DG, Schroeder OH-U, Gramowski A, Shafer TJ. Microelectrode arrays: A physiologically based neurotoxicity testing platform for the 21st century. *NeuroToxicology*. 2010;31(4):331-350. doi:10.1016/j.neuro.2010.04.001

88. Shafer TJ. Application of Microelectrode Array Approaches to Neurotoxicity Testing and Screening. *Adv Neurobiol*. 2019;22:275-297. doi:10.1007/978-3-030-11135-9_12

89. Zwartsen A, Hondebrink L, de Lange DW, Westerink RHS. Hyperthermia exacerbates the acute effects of psychoactive substances on neuronal activity measured using microelectrode arrays (MEAs) in rat primary cortical cultures in vitro. *Toxicology and Applied Pharmacology*. 2020;397:115015. doi:10.1016/j.taap.2020.115015

90. Wu J, Fisher RS. Hyperthermic Spreading Depressions in the Immature Rat Hippocampal Slice. *Journal of Neurophysiology*. 2000;84(3):1355-1360. doi:10.1152/jn.2000.84.3.1355

91. Kiyatkin EA. Brain temperature and its role in physiology and pathophysiology: Lessons from 20 years of thermorecording. *Temperature (Austin)*. 2019;6(4):271-333. doi:10.1080/23328940.2019.1691896

92. Hájos N, Mody I. Establishing a physiological environment for visualized in vitro brain slice recordings by increasing oxygen supply and modifying aCSF content. *Journal of Neuroscience Methods*. 2009;183(2):107-113. doi:10.1016/j.jneumeth.2009.06.005

93. VanLandingham KE, Heinz ER, Cavazos JE, Lewis DV. Magnetic resonance imaging evidence of hippocampal injury after prolonged focal febrile convulsions. *Annals of Neurology*. 1998;43(4):413-426. doi:https://doi.org/10.1002/ana.410430403

94. Baram TZ. Chapter 13 - Animal Models for Febrile Seizures. In: Baram TZ, Shinnar S, eds. *Febrile Seizures*. Academic Press; 2002:189-201. doi:10.1016/B978-012078141-6/50015-9

95. Chen K, Baram TZ, Soltesz I. Febrile seizures in the developing brain result in persistent modification of neuronal excitability in limbic circuits. *Nature Medicine*. 1999;5(8):888-894. doi:10.1038/11330

96. Dube C, Chen K, Eghbal-Ahmadi M, Brunson K, Soltesz I, Baram TZ. Prolonged Febrile Seizures in the Immature Rat Model Enhance Hippocampal Excitability Long Term. *Ann Neurol*. 2000;47(3):336-344.

97. Cariou A, Payen J-F, Asehnoune K, et al. Targeted temperature management in the ICU: guidelines from a French expert panel. *Ann Intensive Care*. 2017;7:70. doi:10.1186/s13613-017-0294-1

98. Curran LK, Newschaffer CJ, Lee L-C, Crawford SO, Johnston MV, Zimmerman AW. Behaviors Associated With Fever in Children With Autism Spectrum Disorders. *Pediatrics*. 2007;120(6):e1386-e1392. doi:10.1542/peds.2007-0360
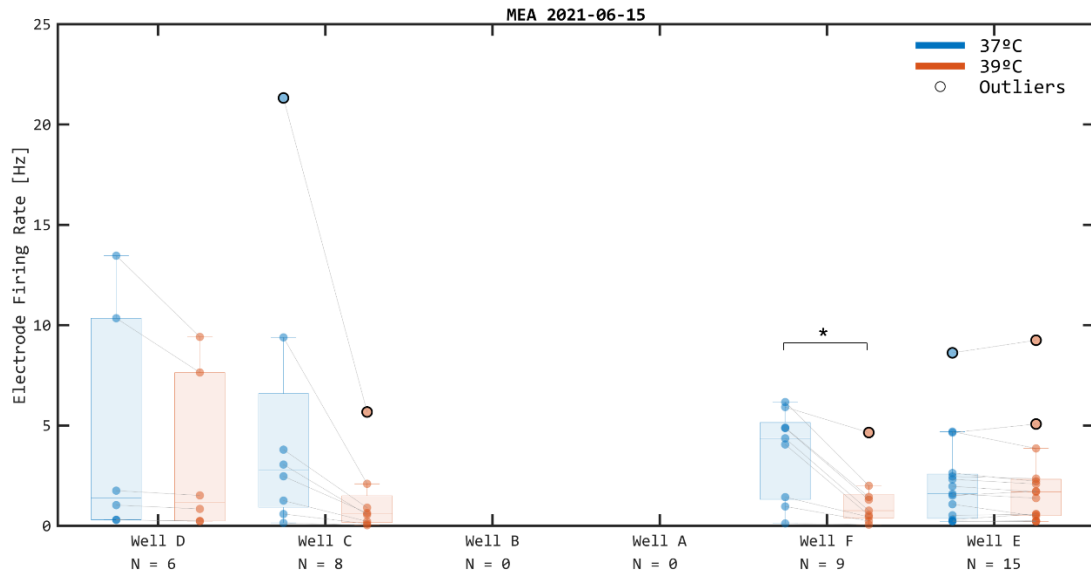
Supplementary Information

Figure S1 - The effect of hyperthermic conditions (39°C) in the MFR for all wells of an MEA (15-06-2021).
All electrodes active for one or both conditions were considered. * Indicates a temperature-induced significant difference (p < 0.05).
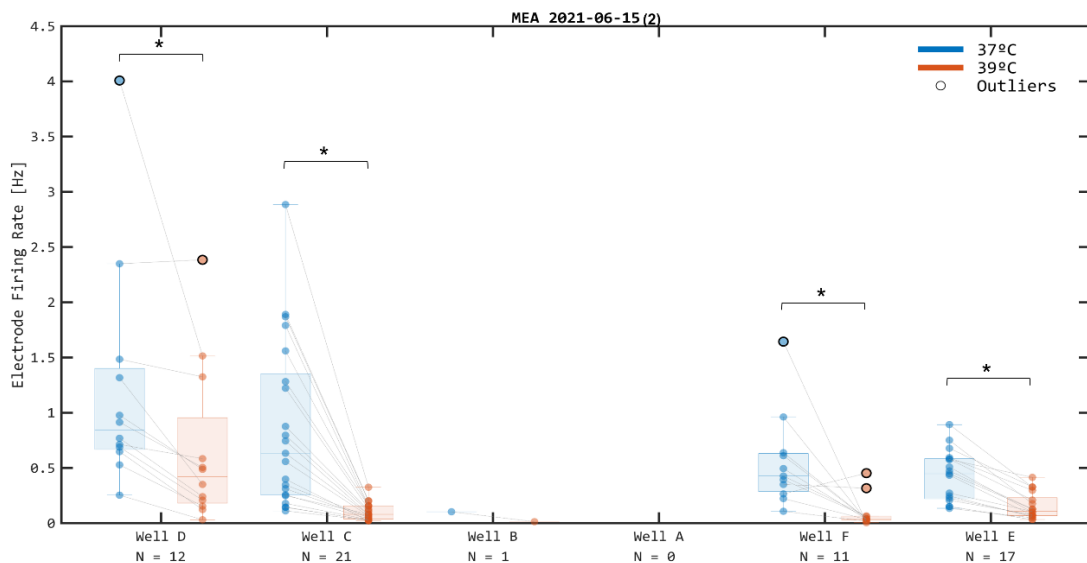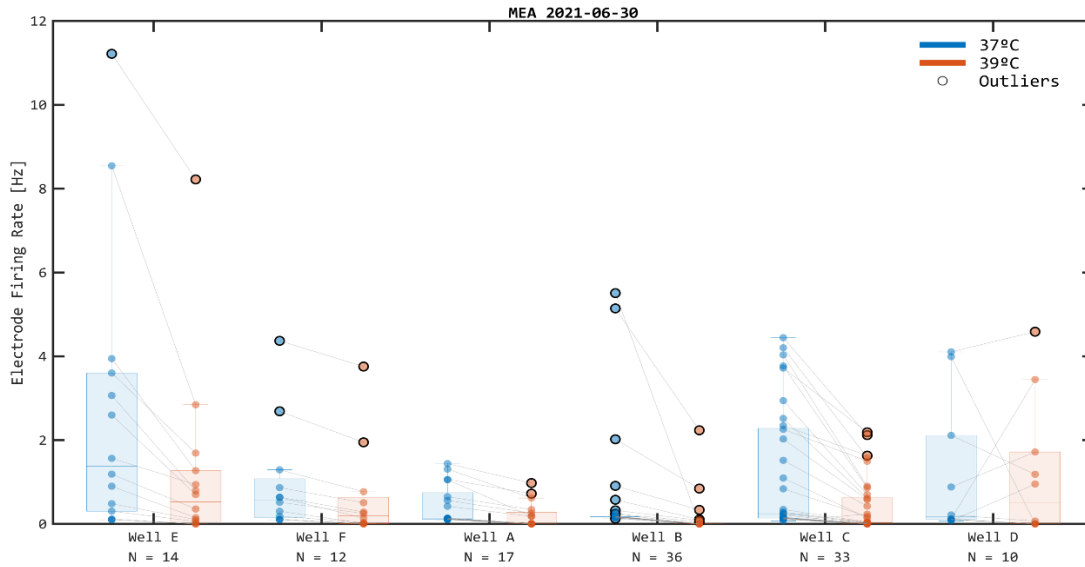

Figure S2 - The effect of hyperthermic conditions (39°C) in the MFR for all wells of an MEA (15-06-2021(2)).
All electrodes active for one or both conditions were considered. * Indicates a temperature-induced significant difference (p < 0.05).

Figure S3 – The effect of hyperthermic conditions (39°C) in the MFR for all wells of an MEA (30-06-2021).
All electrodes active for one or both conditions were considered. * Indicates a temperature-induced significant difference (p < 0.05).
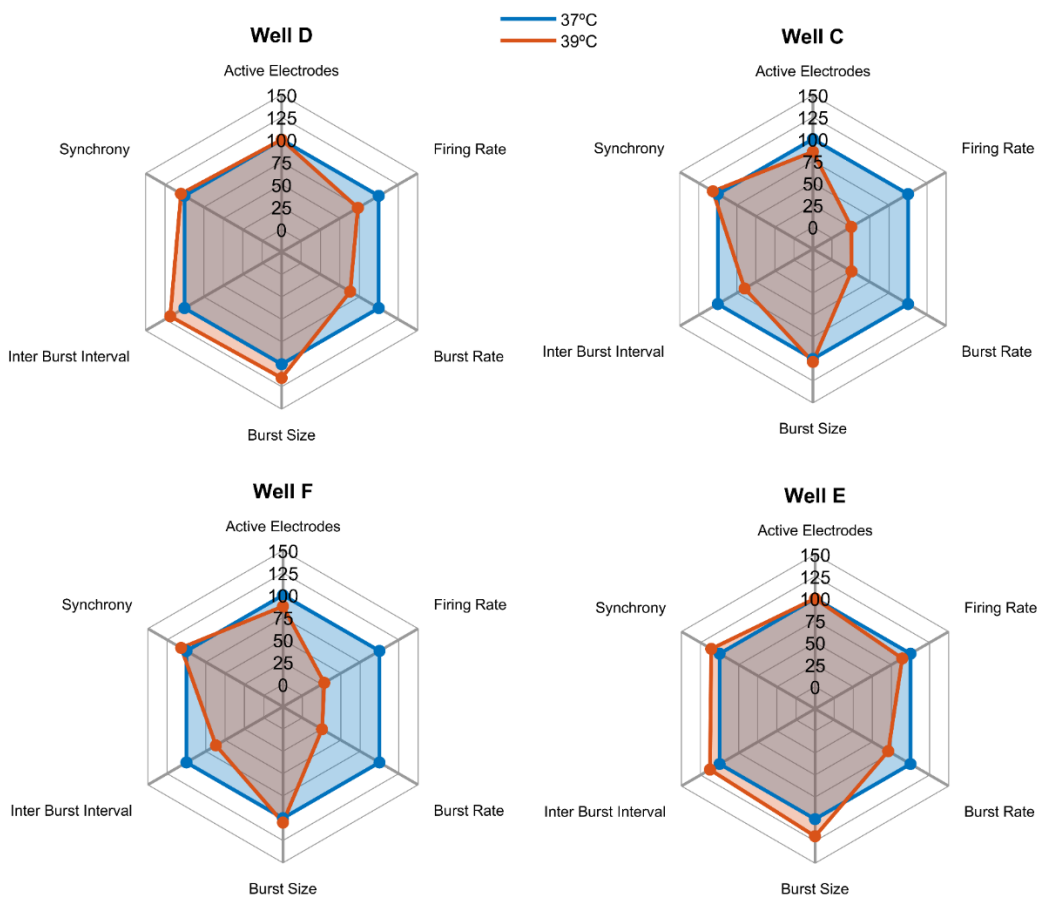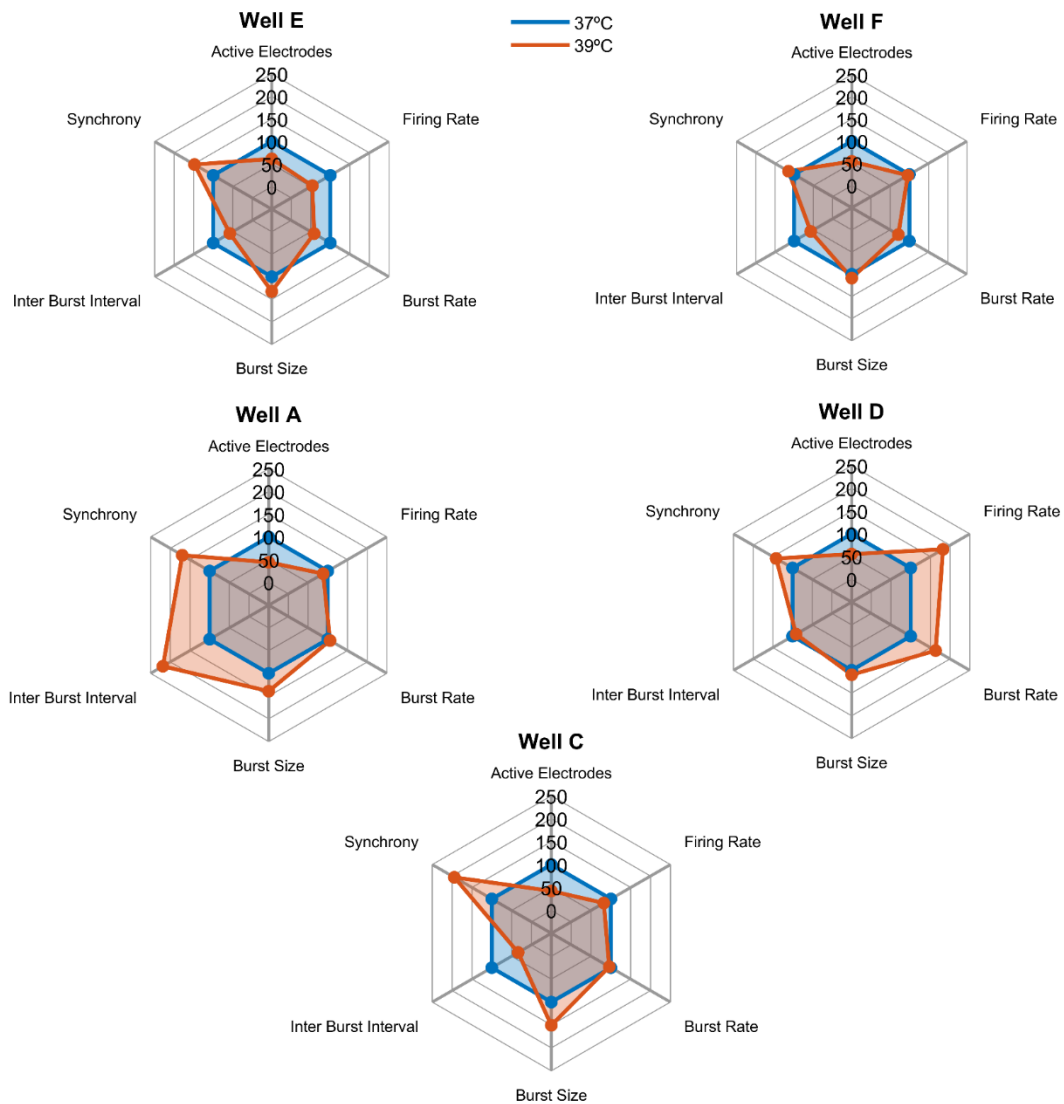

Figure S4 - Effect of an increase in temperature (39°C) on a set of activity-characterizing metrics for each well in an MEA (15-06-2021).
The evolution is displayed as the percentage variation from each parameter at 39°C to the parameter at baseline, 37°C, which is normalized as 100%.

2021-06-15(2) Individual Well
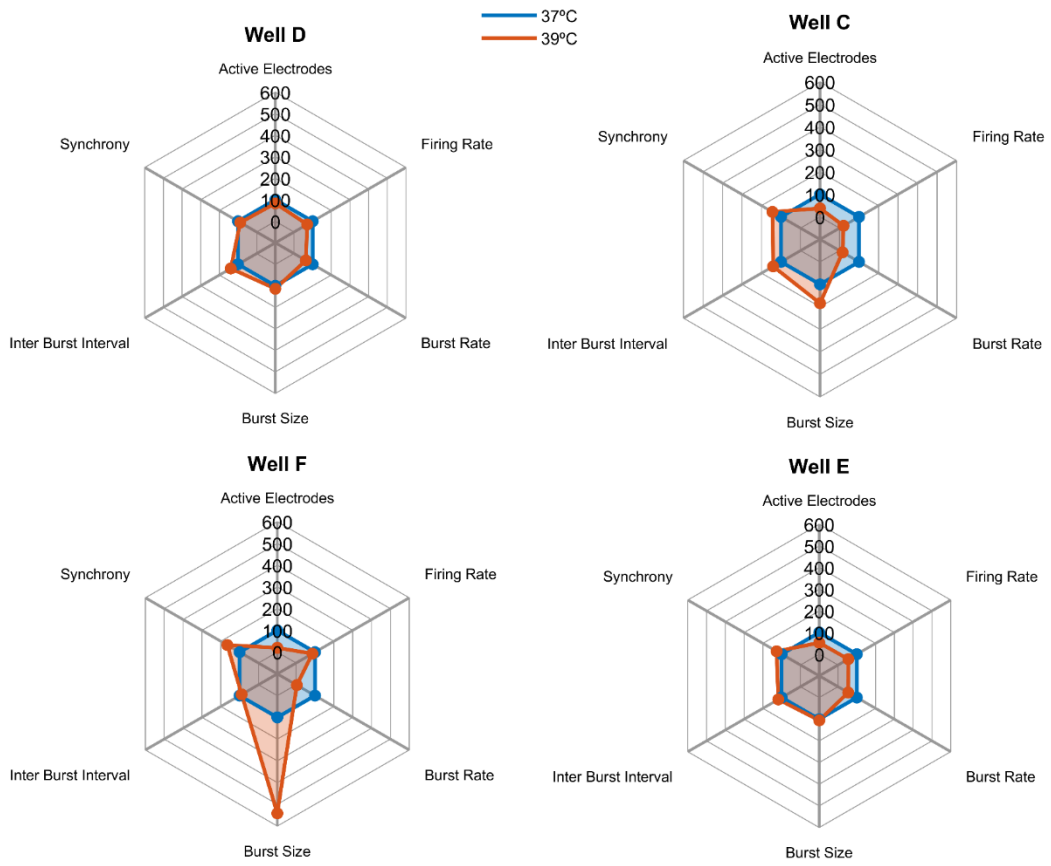
Figure S5 – Effect of an increase in temperature (39°C) on a set of activity-characterizing metrics for each well in an MEA (15-06-2021(2)).
The evolution is displayed as the percentage variation from each parameter at 39°C to the parameter at baseline, 37°C, which is normalized as 100%.

Figure S6 - Effect of an increase in temperature (39°C) on a set of activity-characterizing metrics for each well in an MEA (30-06-2021).
The evolution is displayed as the percentage variation from each parameter at 39°C to the parameter at baseline, 37°C, which is normalized as 100%.
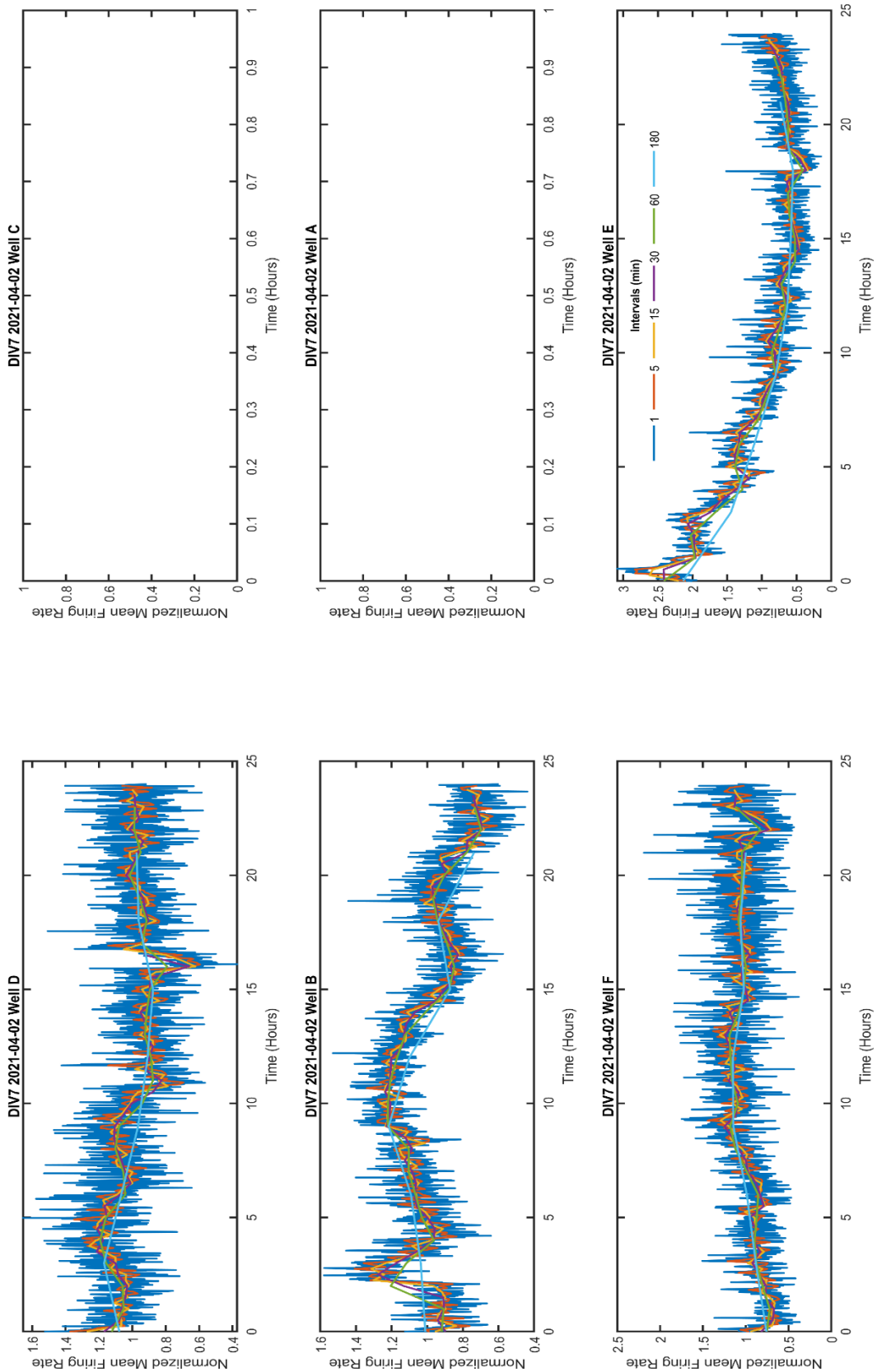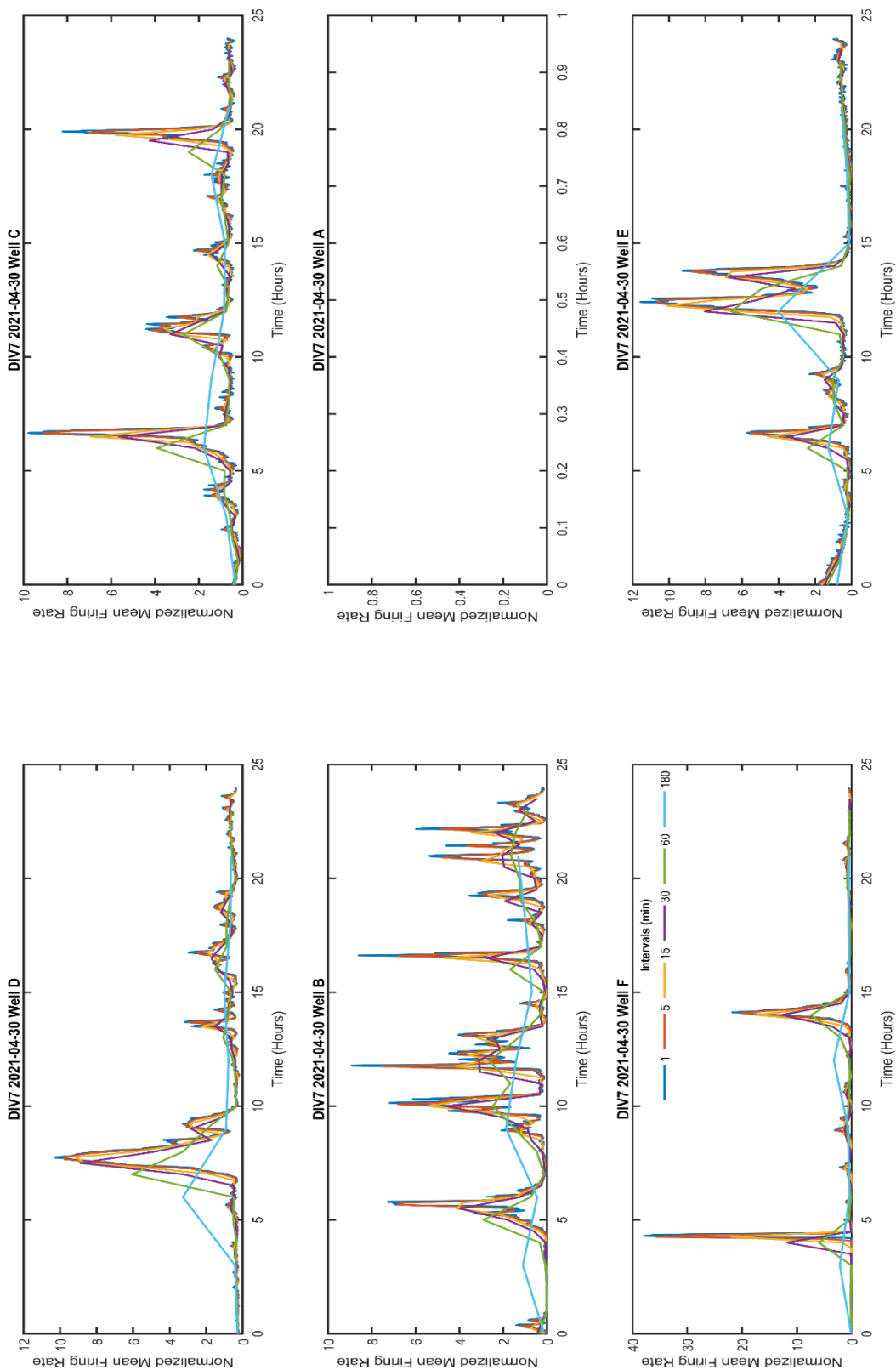
Figure S7 - Profiles of normalized MFR for all wells in an MEA at DIV 7 (02-04-2021).
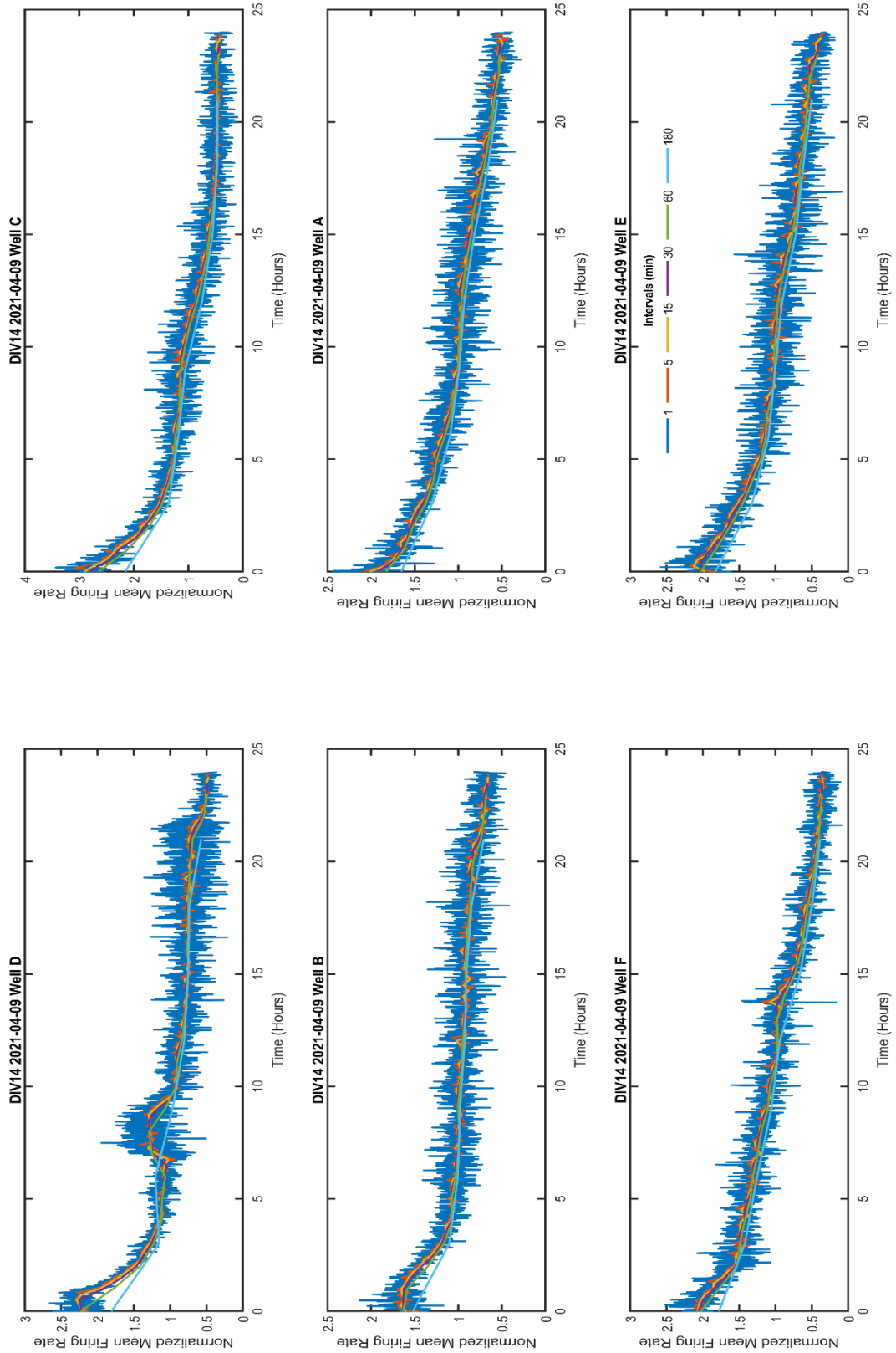Active Electrodes: 5 Well D; 1 Well C; 6 Well B; 3 Well A; 5 Well F; 6 Well E.
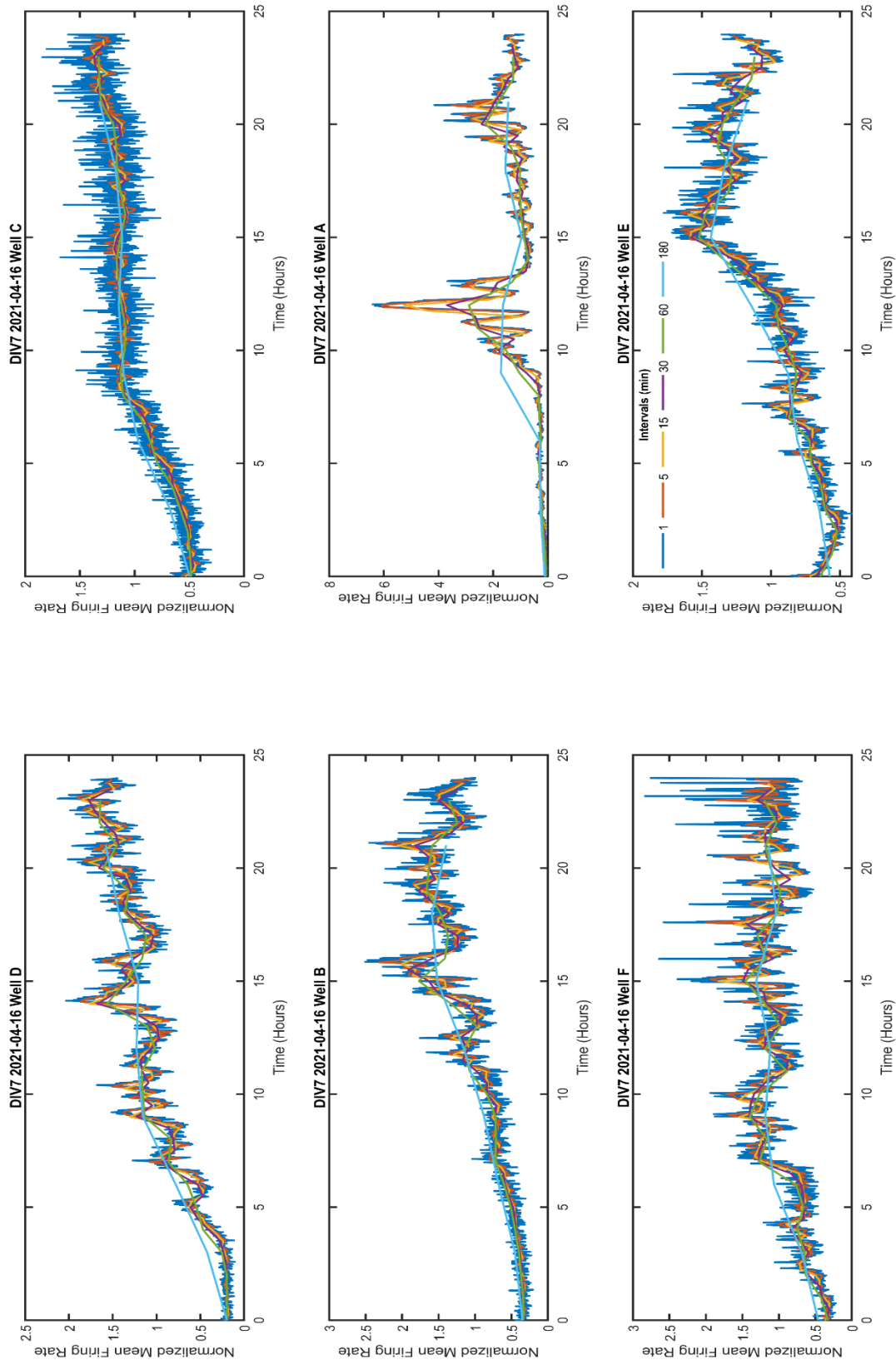
Figure S8 - Profiles of normalized MFR for all wells in an MEA at DIV 7 (16-04-2021).
Active Electrodes: 12 Well D; 22 Well C; 14 Well B; 11 Well A (should be ignored); 17 Well F; 18 Well E.

Figure S9 - Profiles of normalized MFR for all wells in an MEA at DIV 7 (30-04-2021).
Active Electrodes: 14 Well D; 10 Well C; 6 Well B; 1 Well A; 6 Well F; 7 Well E.

Figure S10 – Profiles of normalized MFR for all wells in an MEA at DIV 14 (09-04-2021).
Active Electrodes: 21 Well D; 9 Well C; 25 Well B; 12 Well A; 11 Well F; 14 Well E.
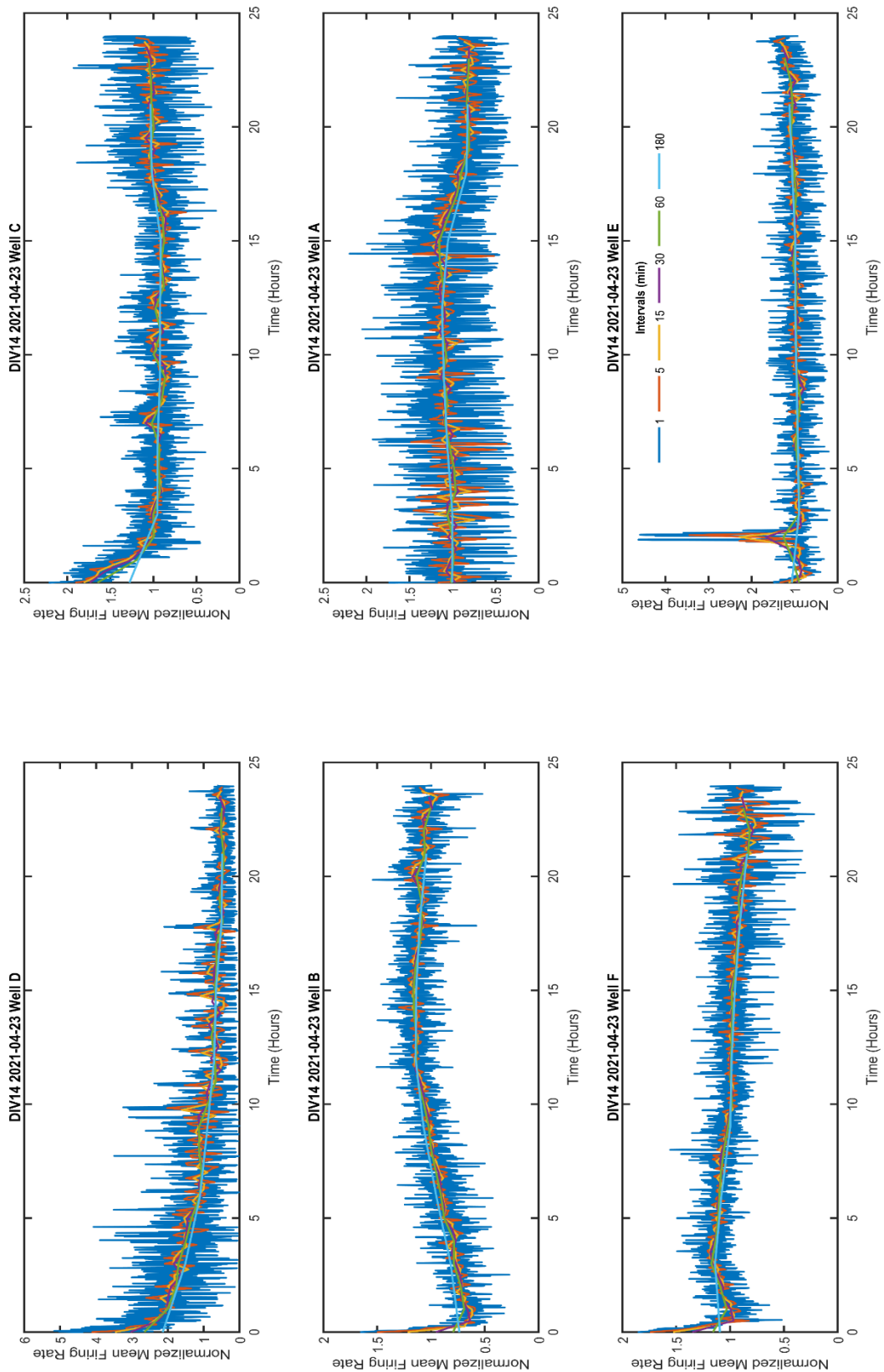
Figure S11 - Profiles of normalized MFR for all wells in an MEA at DIV 14 (23-04-2021).
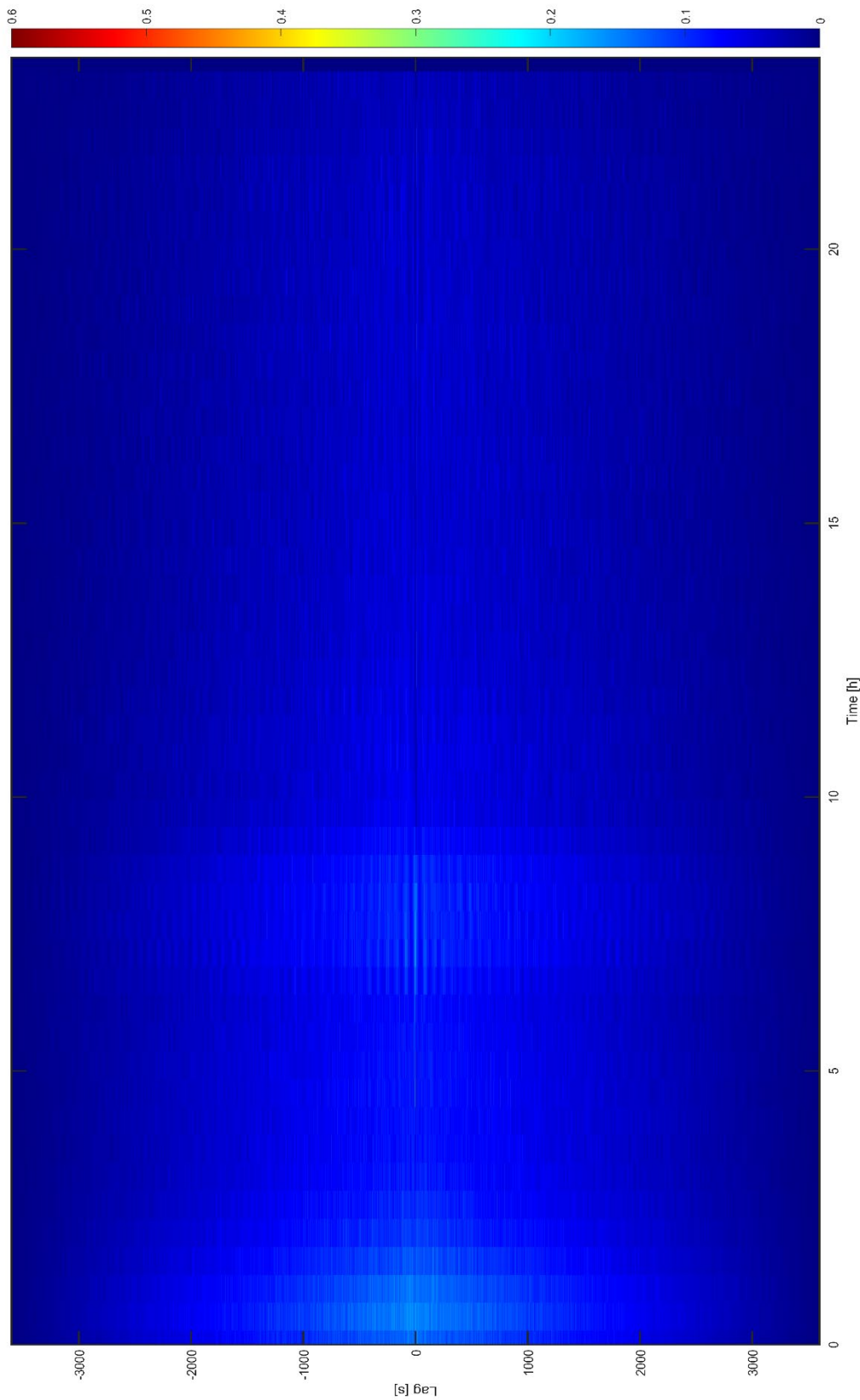Active Electrodes: 32 Well D; 40 Well C; 30 Well B; 27 Well A; 26 Well F; 25 Well E.

Figure S12 – Autocorrelation.
Representative autocorrelation profile seen in one well (DIV14 – 09042021 well D). 1 hour autocorrelation at each 30 min time mark. Lags represent the time deviation of each profile from itself. Colorbar for reference of correlation. No correlation will be close to 0, while max correlation is at 0.6.
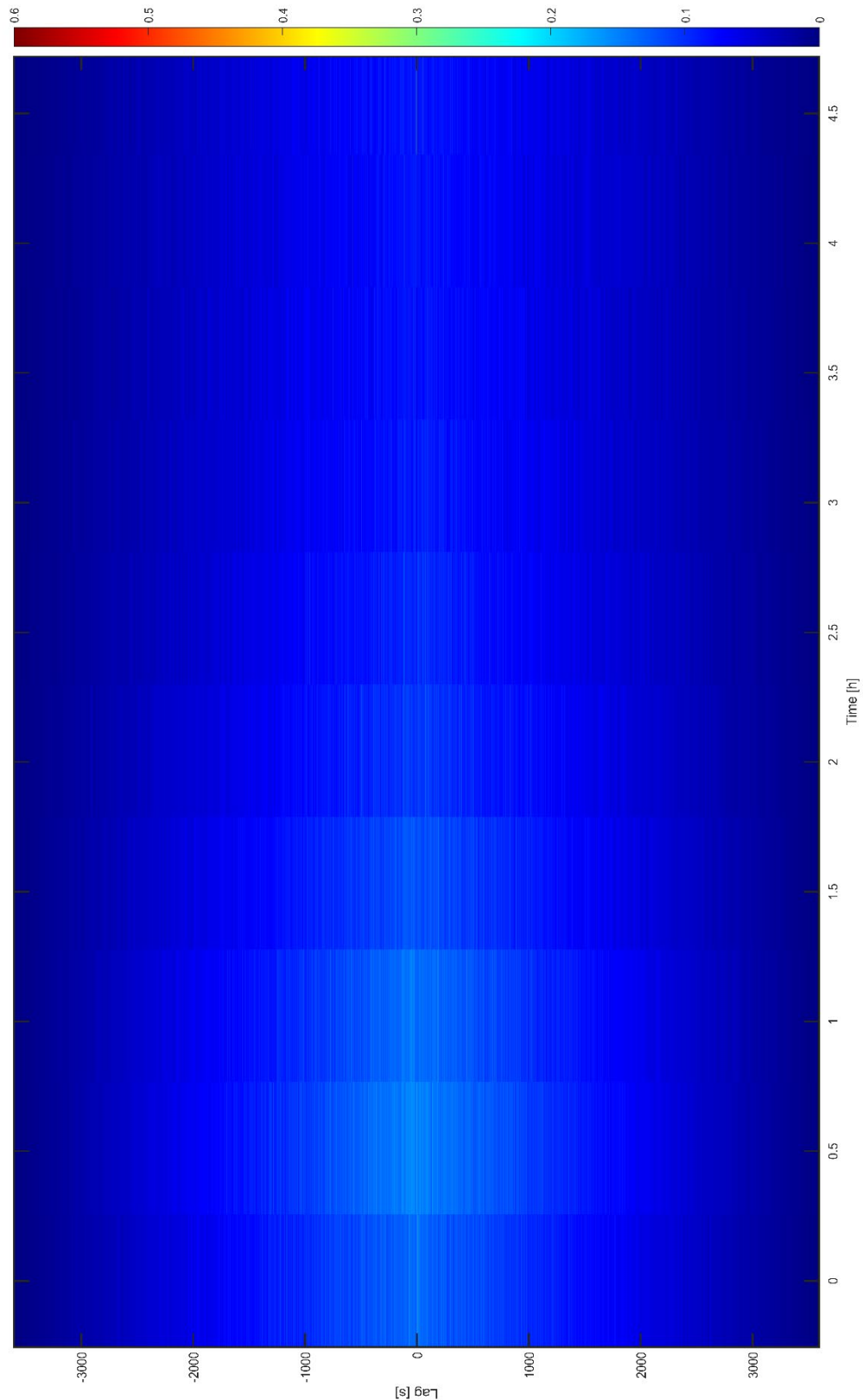
Figure S13 – Autocorrelation 5 hours.
Representative autocorrelation profile seen in one well (DIV14 – 09042021 well D) for the first 5 hours. 1 hour autocorrelation at each 30 min time mark. Lags represent the time deviation of each profile from itself. Colorbar for reference of correlation. No correlation will be close to 0, while max correlation is at 0.6.
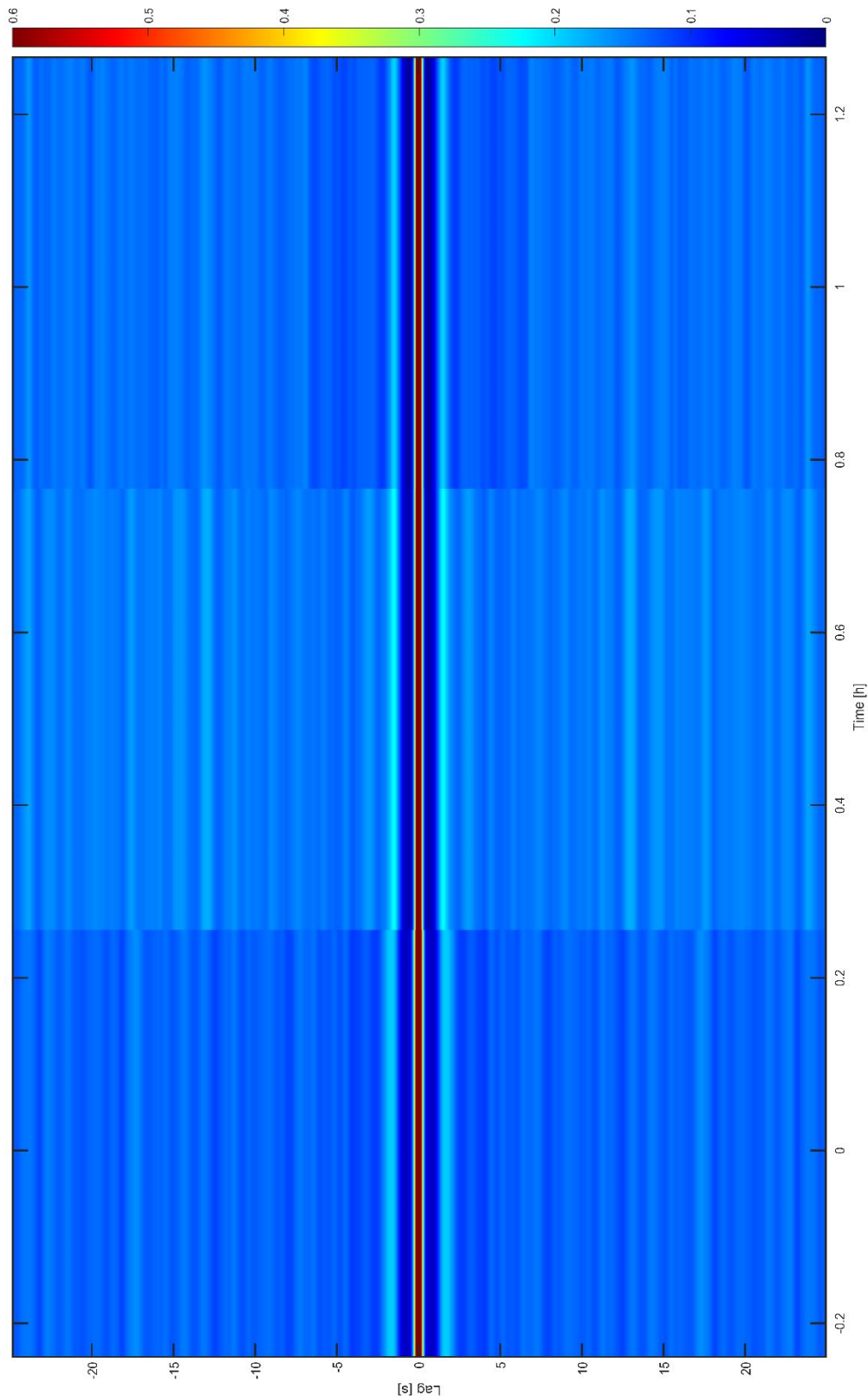
Figure S14 – Autocorrelation 1 hour.
Representative autocorrelation profile seen in one well (DIV14 – 09042021 well D) for the first hour. 1 hour autocorrelation at each 30 min time mark. Lags represent the time deviation of each profile from itself. Colorbar for reference of correlation. No correlation will be close to 0, while max correlation is at 0.6. At 0 s lag there is an expected max correlation evidenced by the dark red line.